Converter based Electrochemical Impedance Spectroscopy for Fuel Cell Stacks

by

Jiabin Shen

M.Eng., Memorial University of Newfoundland, Canada, 2017
B.Sc., China University of Petroleum, China, 2015

Thesis Submitted in Partial Fulfillment of the
Requirements for the Degree of
Doctor of Philosophy

in the
School of Mechatronic Systems Engineering
Faculty of Applied Sciences

SIMON FRASER UNIVERSITY

Spring 2021

Declaration of Committee

Name: **Jiabin Shen**

Degree: **Doctor of Philosophy**

Title: **Converter based Electrochemical Impedance Spectroscopy for Fuel Cell Stacks**

Committee:

Chair: Ramtin Rakhsha
Lecturer, Mechatronic Systems Engineering

Jiacheng Wang
Supervisor
Associate Professor, Mechatronic Systems Engineering

Patrick Palmer
Committee Member
Professor, Mechatronic Systems Engineering

Mohammad Narimani
Committee Member
Lecturer, Mechatronic Systems Engineering

Mehrdad Moallem
Examiner
Professor, Mechatronic Systems Engineering

Wilson Eberle
External Examiner
Associate Professor, Engineering
The University of British Columbia

Abstract

Fuel cells are important devices in a hydrogen-based chain of energy conversion. They have distinctive advantages over batteries with their higher energy density and faster refueling speed, which make them attractive in stationary power supplies and heavy-duty vehicles. However, the high cost and low durability associated with modern fuel cells are still hindering their wider commercialization. Besides developing more reliable and lower cost materials and advanced assemblies of cells and stacks, a practical and effective diagnostic tool is highly needed for fuel cells to identify any abnormal internal conditions and assist with maintenance scheduling or application of on-board mitigating schemes. Conventionally, linear instruments were used for fuel cell EIS, however, limited to single cells or short stacks only as a laboratory testing method. With recent developments, EIS enabled by switching power converters are capable of being applied to a high-power stack directly. This approach has the potential for practical field applications such as a servicing tool for fuel cell manufacturers or an on-board diagnostic tool of a moving vehicle. Previous works on converter based EIS have made a few different attempts at conceptually realizing this solution while several significant issues were not well recognized and resolved yet. As such, this thesis explores further on this topic to address the flexibility of EIS perturbation generation, the perturbation frequency range, and the linkage between fuel cell EIS requirements and the converter design to push for its readiness for practical implementations. Several new solutions are proposed and discussed in detail, including a total software approach for existing high-power converters to enable wide-frequency-range EIS, a redesign of the main dc/dc converter enabling wide-frequency-range perturbations, and a separate auxiliary converter as a standalone module for EIS operation. A detailed analysis of oscillations brought by converter based EIS in powertrains is also presented.

Acknowledgements

The thesis would never be possible without the continuous supports and valuable suggestions from my senior supervisor Dr. Jiacheng Wang. I would like to thank him for all the helps provided throughout the past few years, not only limited to the academic discussions, but also advises on my career and life. I would also like to thank my supervisors Dr. Patrick Palmer and Dr. Mohammad Narimani for their comments and helps on improving this work.

I would like to express my gratitude to the examining committee Dr. Wilson Eberle and Dr. Mehrdad Moallem for being present at my defense and providing valuable comments. My gratitude also goes to Dr. Ramtin Rakhsha for hosting the defense session.

I would also like to thank my parents and my wife, Yuanyuan Niu, for their unconditional loves and supports during my pursuing of the doctoral degree. Many thanks to my colleagues and friends at the Power Electronics and Energy Applications Laboratory (PEEAL), who made this journey much enjoyable. Special thanks to Hooman Homayouni for introducing me to the fascinating fuel cell world. I appreciate the opportunity of an industrial intern provided by Dr. Jake Devaal and receiving industrial inputs from him as well as Greg Afonso at Ballard Power Systems.

I acknowledge the funding provided by the Natural Sciences and Engineering Research Council of Canada (NSERC) and Mathematics of Information Technology and Complex Systems (MITACS). I also thank the Kaiser Foundation for providing me with the award for Digitally Controlled Power Electronics.

Table of Contents

List of Figures

List of Tables

List of Abbreviations

ACMC	averaged current mode control
ADC	analog-to-digital converter
CF	current-fed
CF-DAB	current-fed dual active bridge
CPL	constant power load
ECM	equivalent circuit model
EIS	electrochemical impedance spectroscopy
FCS	fuel cell stack
FCV	fuel cell vehicle
HI	health indicator
IGBT	insulated gate bipolar transistor
MOSFET	metal–oxide–semiconductor field-effect transistor
PEM	polymer electrolyte membrane
PI+R	proportional-integral plus resonant
PPC	power processing converter
PSES	primary side energy storage
PWM	pulse-width modulation
RUL	remaining useful life
SiC	silicon carbide
ZOH	zero-order hold
ZCS	zero current switching
ZVS	zero voltage switching

Chapter 1 Introduction

This chapter introduces the general research background and motivations of this work. A detailed literature review is provided, where previous efforts in this line of research are visited and explained and the existing research gaps are identified. Electrochemical impedance spectroscopy (EIS) is an effective technique for finding internal abnormal conditions of a fuel cell, and EIS perturbations generated by power converters enable *in situ* diagnostics on a fuel cell stack (FCS) which almost inevitably needs a power conditioning converter to properly function in practical applications. However, it is found that hardware constraints of the perturbation generating converters have impacts on the achievable EIS frequency range. Additionally, the level of flexibility of generating the ac perturbations *in situ* and the influences of inducing EIS perturbations on the converter systems were not well recognized and addressed in the previous works. This thesis aims to resolve these issues by proposing three converter based solutions, including approaches of both hardware and software in nature, for effective implementation of *in situ* EIS to improve condition monitoring and diagnostics of a practical FCS. It also presents a detailed analysis on EIS induced oscillations and their propagation in a hybrid fuel cell powertrain system with other connected components which helps reveal the influence of such operations in a practical application scenario.

1.1 Research Background and Motivation

Due to the rising concerns of climate change and environmental protection and targeting for a carbon neutral future, transportation manufacturers are shifting from traditional internal combustion engine vehicles to their clean energy alternatives. Besides its features of high efficiency and zero emission, a fuel cell vehicle (FCV) has unique advantages compared to battery-powered electric vehicles such as longer ranges due to the higher energy density of hydrogen and faster refueling speeds. With the many research and development efforts and advancements made over the past decades, fuel cells present a promising solution for future clean energy vehicles, especially in the heavy-duty sector such as buses and trucks [1].

Among all, the polymer electrolyte membrane (PEM) fuel cell has received increasing attention in stationary power supplies and motive hydrogen-powered vehicles. However, the limited durability and reliability of a state-of-the-art PEM FCS are still hindering its wider commercial adoption. It suffers from a variety of degradation and fault conditions [2], [3], especially in vehicular powertrains that are subject to more dynamic load cycles. Urban-route trial bus projects found that the dynamic load variations affected the life of FCS significantly and scheduled maintenances were necessary to extend their services [4], [5]. The fleet in [5] had an average of 9178 hours of service which was much lower than the targeted 18000 hours. In addition to advancing the fuel cell technology itself, an effective stack-level *in situ* diagnostic tool is highly desirable in practice, where it can be applied to facilitate maintenance services or used for on-board diagnostics. It is noted here that *in situ* refers to that no displacement is required for the FCS and the EIS is carried out when the system is either operational or idling. Great efforts and costs would be saved by detecting internal conditions without disassembling the stack and necessary mitigating approaches can be performed to prevent further damages, or even applied directly with proper system control given diagnostic results are obtained on-board. For example, when a drying fault occurs in an FCS, procedures such as increasing humidification or shutting down the system is expected. Therefore, the possibility of forming pinholes [2], with which the hydrogen at the anode will directly react with oxygen at the cathode and generating no electricity, is effectively reduced and the lifetime of an FCS can be extended.

Several characterization methods, including voltage cycling [6], cell voltage monitoring [7], total harmonic distortion analysis [8], and EIS, are available for use on fuel cells. Of all these approaches, EIS has attracted more interests due to its higher information density and presenting minimal interference to normal operations, hence allowing *in situ* diagnostics. The EIS operation is typically triggered by imposing a small ac perturbation of potential or current on the fuel cell dc operating point, thus the fuel cell internal impedance can be acquired from the fuel cell response and an impedance spectrum is obtained by changing the frequency of ac perturbations. This output, an impedance spectrum, varying with the internal conditions of an FCS, contains rich information and can be used for identifying fuel cell internal conditions. EIS was conventionally applied to assist with designing, manufacturing, and testing of the cells. Recently, it has also been adopted as a solution for fault diagnostics [9]-[11] and degradation analysis [4], [12]-[14] intended for either offline servicing or on-board condition monitoring of fuel cells.

To apply EIS for diagnostics on a commercially adopted FCS in vehicular applications, the limited voltage and power rating of the traditional EIS instruments cannot directly satisfy the requirement. The commonly used EIS devices are manufactured by companies such as Gamry Instruments Inc. and Kikusui Electronics Inc. They provide commercial EIS instruments that are normally designed at low voltage and power ratings and with bulky enclosures for lab testing on single cells or short stacks only. These off-the-self products cannot meet the needs of carrying out *in situ* EIS on practical automotive FCS for maintenance or on-board diagnostics. Therefore, further developments of the EIS tool are needed.

The main application scenarios of adopting EIS for diagnostics on an FCS, such as in a vehicular powertrain, are offline servicing maintenance and on-board diagnostics. In servicing maintenance, the FCV is stopped, and the system is either shut down or in idling mode. The fuel cell will be re-wired to a testing bench for maintenance. The EIS operation is then performed and expected to provide diagnosis on the possible faulty conditions of a stack without opening it, which brings significant value for a servicing team. Moreover, the health condition of a stack can be checked periodically, and a report of assessment and identification of the potential hazards could be generated. Therefore, further damages on the stack are prevented with proper means responding to the diagnostic results. For example, pinholes may be formed on the fuel cell membrane due to mechanical stress or hot spots caused by inappropriate controls or unexpected operating conditions. However, small pinholes cannot be easily detected from the fuel cell output voltage, not to say quantification and location of the pinholes in a stack. Fuel cell manufacturers such as Ballard are developing EIS technique as a valid approach for detection and quantification of different abnormal conditions such as hydrogen crossover on its fuel cell products.

On the other hand, the on-board application of EIS diagnostic tool is more challenging due to the space requirement and complex and uncontrollable environment in a powertrain. However, the benefit brought by enabling EIS on-board is obvious as detection of the FCS conditions can be conducted without detaching and rewiring the FCS to a testing bench. Moreover, fault mitigation methods can be potentially applied with on-board system control given the type of fault is identified. For example, a humidification adjusting system can be implemented based on the humidification related high-frequency impedance obtained from EIS, where the membrane humidification is difficult to be detected by regular sensors, and fault tolerant control is therefore possible, such as the one proposed in [15].

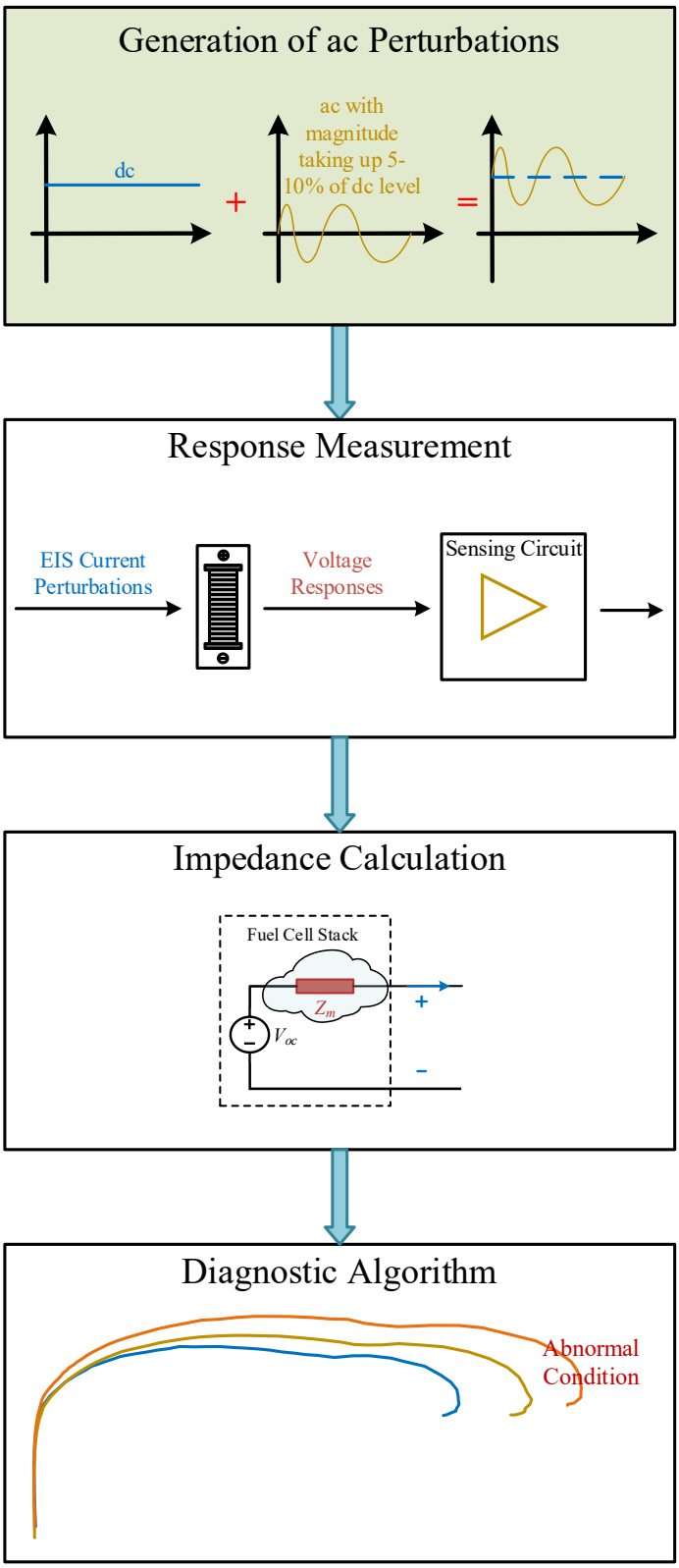

Fig. 1.1. Four stage process of applying EIS as a diagnostic tool for fuel cell stacks.

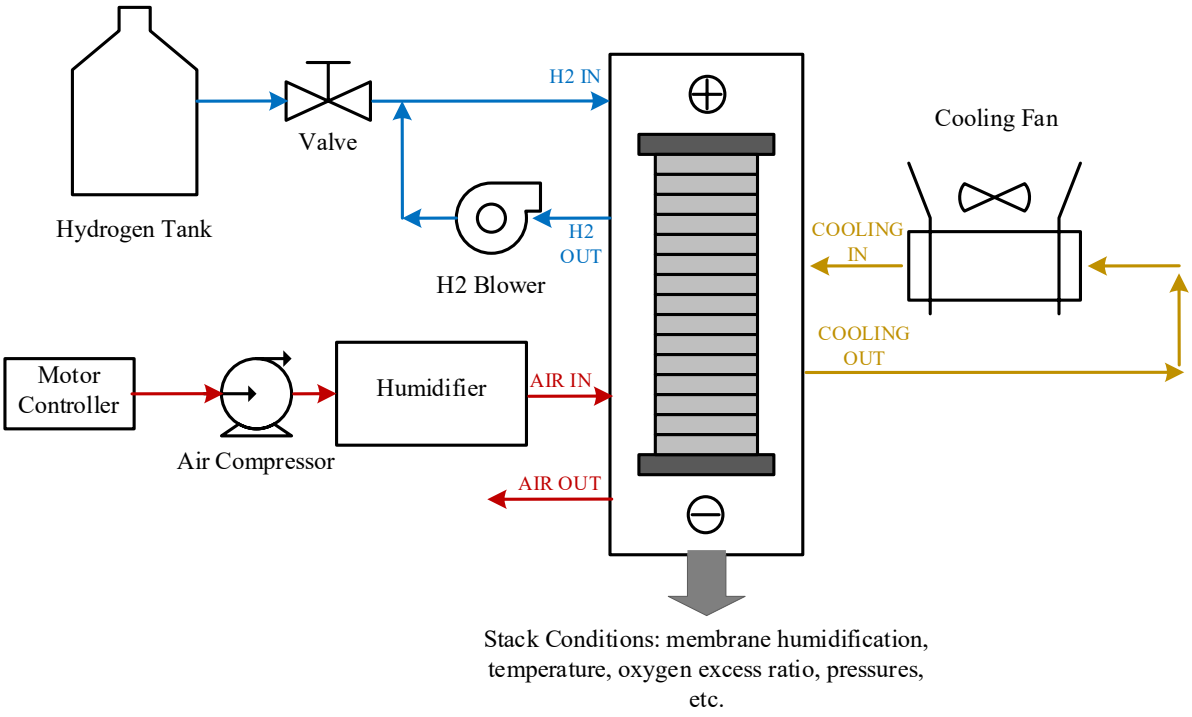

Fig. 1.2. Simplified diagram of a fuel cell stack and its subsystems.

To use EIS as a diagnostic tool, the entire process is divided into four stages, i.e., generating perturbations, measuring responses, calculating impedances, and performing diagnostics, as illustrated in Fig. 1.1. Each stage of the process is elaborated as follows.

1. **To begin an EIS operation, the FCS is held at a certain steady state operating point and variable frequency ac perturbations are imposed on this operating point as the first stage.** All commercially available FCS come with embedded controllers to manage its sub-systems, as shown in Fig. 1.2. The internal conditions are adjusted by the embedded controllers to deliver the needed output powers, and therefore, the FCS is a black box from the system output control's perspective. This is directly reflected as the condition-dependent impedance spectrum changes with different dc current outputs. Therefore, during the EIS testing, the dc operating point should be held to obtain a stable and usable EIS result. In the case of a testing or a maintenance servicing bench, the fixed dc operating point of the FCS is easily achieved by setting a constant load bank. However, a grid-connected inverter is necessary for testing at high output power levels of a multi-kilowatt stack. On the other hand, when EIS is applied for on-board diagnostics, the energy storage in the hybrid fuel cell powertrain, normally a battery bank, can be adopted to hold the FCS

operating point and the EIS operation would be performed with the propulsion motor staying in either the running or idling mode. In the on-board approach, the capacity of the energy storage needs to be considered to avoid being over-charged or discharged in coordination with system level energy managements. Operating EIS with the motor running might achieve higher fuel cell dc currents. Overall, adopting stack-level EIS in a servicing testing bench is easier to achieve with the more controllable environment, while on-board adoption is more challenging and needs cooperation from the powertrain system's perspective. Once the dc operating point is set, variable frequency ac perturbations are applied to the FCS. Since each FCS module is made up of series-connected cells, the galvanic mode is normally adopted when applying ac excitations to a stack. The magnitude of the required current perturbations is normally set to 5%-10% of the dc component. The selection of this magnitude is a tradeoff between the linearity of the operation and the measurability and accuracy of ac voltage responses [16]. The effective frequency range for fuel cell EIS is between a few kilohertz to sub-hertz.

2. **Once the ac current perturbations are presented, the voltage responses need to be measured.** The ac components in the voltage responses are of concern in an EIS operation. For high-voltage stack-level EIS operations, the voltage responses contain a relatively high dc level, where the needed ac responses are easily submerged. The internal impedance of an FCS is relatively small, usually only a few milliohms, and the magnitude of ac perturbations is only 5% to 10% of the dc current. Conventional signal conditioning circuits proportionally reduce both ac and dc components at the same time. Therefore, the ac component in the fuel cell voltage is not easily detectable, and the needed ac components information takes up only a few bits when being sent to an analog-to-digital converter (ADC), leading to inaccurate response measurements. To this end, dc level reduction sensing circuits were proposed and discussed in [17][18]. By only reducing the dc component, the ac perturbations are the main component in the sensed signal, allowing accurate detections of its magnitude and phase shift.

3. **The internal impedance is calculated with obtained responses using calculation algorithms.** Fourier and wavelet [7][19] transformations were used for calculating the impedances with the fuel cell excitations and responses. Since the excitation frequency is known to the system, lock-in amplifier was proposed in [20] to achieve the high noise immunity and was also adopted in [17][21]. Besides the digital implementation of impedance calculations, dedicated ICs are also available, such as AD5964 from Analog Device Inc. From the product development perspective,

using a dedicated impedance calculating IC saves time and costs on validating the code and proving its effectiveness and reliability, while a low cost communicating MCU could be used for displaying and transferring the impedance data.

4. **Finally, the impedance spectrum is acquired as the result of an EIS operation and used for mapping with different conditions of an FCS.** Most diagnostic rules are not based on an analytical fuel cell model since there are no explicit expressions revealing the relations between an impedance spectrum and specific conditions of a fuel cell. Moreover, the designs of FCS vary between manufacturers and a unified model to represent all is not practically possible. As such non-model-based approaches such as fuzzy logic based methods would be more feasible in diagnostics. Equivalent circuit models (ECMs) were widely adopted for facilitating the understanding of the resulting impedance spectrum and the use of them was also introduced as an approach for fuel cell diagnostics. Different ECMs were proposed according to the shape of the impedance spectrum.

The foremost issue of triggering an EIS operation on a high-power FCS lies in how to properly present the required ac perturbations to an FCS, which is the main focus of this thesis. The quality and frequency range of the presented ac perturbations decide the accuracy and the contained information of calculated impedances, thus, determining the diagnostic results. This thesis is devoted to exploring using converters for generating EIS ac perturbations as the first step of triggering an entire EIS operation. A few works have been proposed to use the main power processing converter (PPC) of the FCS to generate ac perturbations by adding ac references to the fuel cell current control loop. EIS enabled by a power converter provides the capability of *in situ* characterization of a commercial high-power high-voltage FCS. It offers a promising solution to bring EIS from laboratories to field applications as an *in situ* health monitoring tool. The concept of using on-board fuel cell converter as the ac perturbation source has been discussed in previous literature. However, several issues related to converter based EIS were not well recognized and addressed. This thesis further explores the topic of converter based EIS for FCS and aims to develop more feasible and practical solutions. What previously neglected are offset, and systematic analysis and verifications are provided to enhance its readiness for practical implementations. In the end, research gaps are filled, and a series of analyses and solutions are proposed and validated as the outcomes of this thesis work.

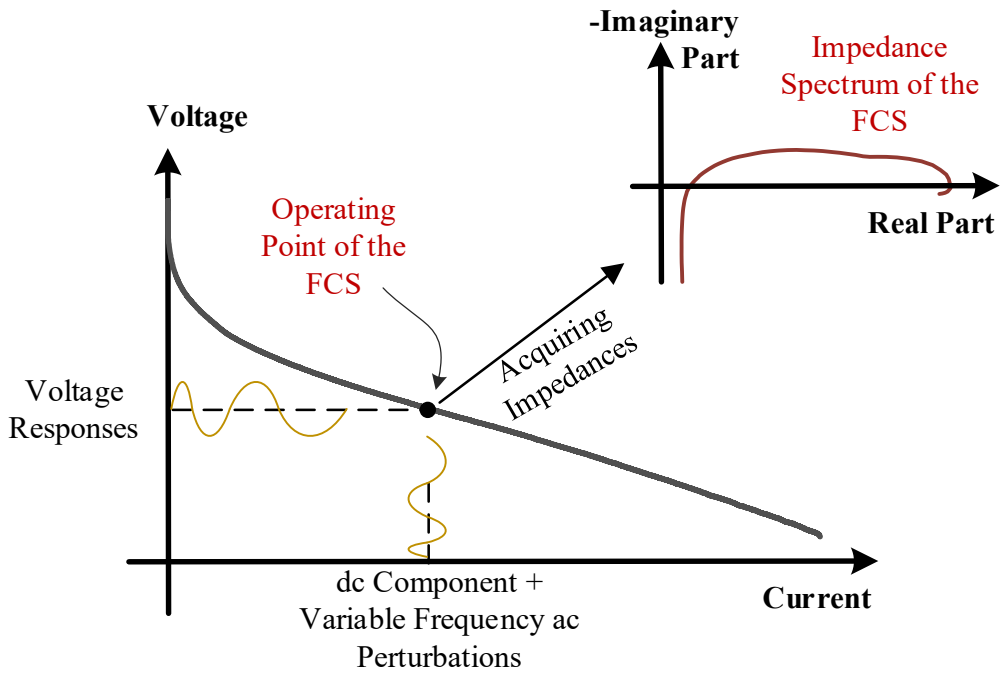

Fig. 1.3. Illustrative diagram of the relationship between a steady state V-I curve and an impedance spectrum.

1.2 Literature Review

EIS operation holds the same concept as the loop measurement for power converters, where a relatively small magnitude of ac perturbation is imposed upon the current dc operating point. By changing the frequencies of ac perturbations and obtaining the responses, internal impedances of an FCS at this dc operating point are acquired. In other words, EIS operation 'linearizes' the nonlinear internal impedance of an FCS at a certain operating point and obtains the 'linearized' impedance model. The relation between a steady-state V-I curve of an FCS and its impedance spectrum is shown in Fig. 1.3, where the V-I curve shows the fuel cell dc output voltage according to its output current. In this figure, a typical impedance spectrum is presented with high frequency impedance at the left side and the lower ones at the right side of the curve. This form of representation of an impedance spectrum is commonly used in fuel cell EIS.

The converter based EIS can directly work with a high-power FCS module and overcome the low-power and low-voltage limitations of conventionally used linear instruments in the offline testing. As commercially used FCS for stationary power supplies or vehicular powertrains comprises of hundreds of cells, excitations generated from converters allow EIS to be used in the field on a practical running FCS, instead of applying to only single-cells or short stacks in the lab.

For example, in a vehicle, a high-power FCS module is kept in the powertrain and the EIS excitations are directly presented to it with its on-board fuel cell converter. Therefore, no extra costs are generated, only the converter control software needs to be updated. The result, an impedance spectrum, can be therefore obtained and advanced diagnostics are applied with the rich information provided. In the end, it saves a great amount of time and costs by identifying the faults and degradation conditions without displacing and disassembling the stack, and in a practical implementation, an up-to-date impedance spectrum can be readily obtained by simply pressing a button from the operator's perspective.

The concept of using converters as the perturbation source was discussed in previous literature. The following sections discuss previous efforts in EIS diagnostics and converter based EIS solutions and the unresolved challenges are identified.

1.2.1 Applications of EIS in Fuel Cell

Three main factors affecting the shape of an impedance spectrum are the operating point, faulty conditions, and degradation. The dc operating point affects the shape of impedance spectrums greatly, where the dc operating point is normally set by the dc current pulling from the FCS as internal conditions are managed by the embedded controllers in a commercially available stack. Various faults occur during the usage of an FCS resulting from inappropriate controls or unexpected conditions, giving a relatively larger variation on the impedance spectrum. Moreover, due to the phenomena such as material aging, the impedance spectrum changes gradually during its usage. Therefore, this forms the basis of adopting the results of the EIS operation for diagnostics.

The changes of the impedance spectrum of an FCS according to dc current, air stoichiometry, relative humidity, and temperature were revealed in [22]. In [23], EIS was performed on a 1.2 kW Nexa PEM fuel cell from Ballard Power Systems Inc. under different current demands, where mass transportation losses are more visible at higher dc currents. In [9], it was shown that EIS results can identify flooding and drying conditions and resulted in a higher resolution than the output voltage measurements. Appropriate humidification of the fuel cell membrane is critical for its conductivity and proper operations of the stack, while flooding will form droplets inside the gas channels preventing oxygen and hydrogen from reaction. Oxygen starvation happens when a sudden current demand change is applied to the stack output and the air compressor fails to supply enough oxygen. This is one of the results that FCS under dynamic load cycles has shorter lifetimes.

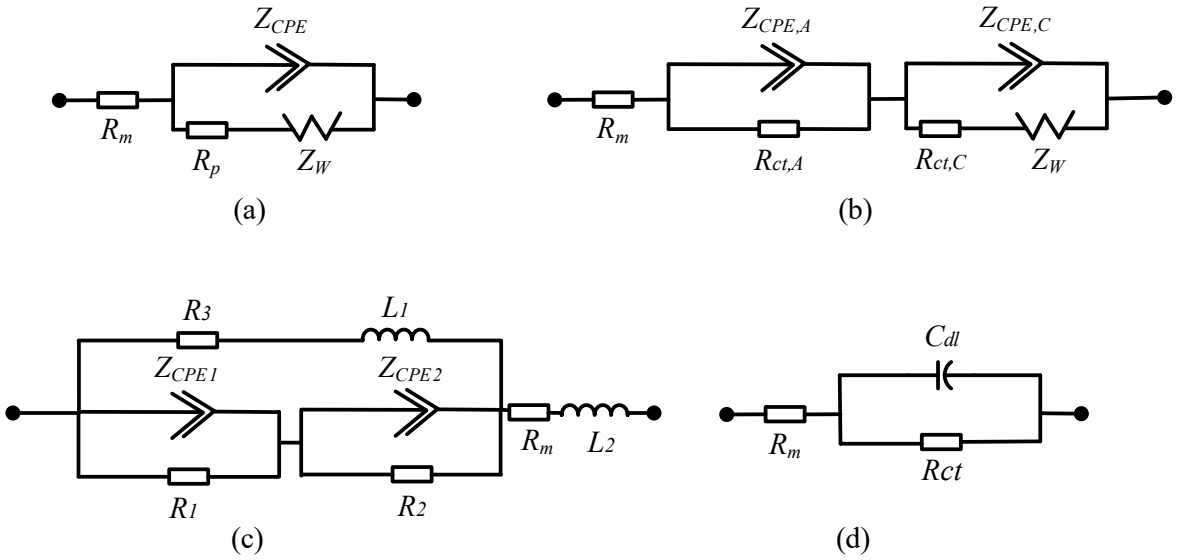

Fig. 1.4. ECMs used in the literature for fitting internal impedances of FCS.

The impedance spectrum affected by it and hydrogen leakage were revealed in [24]. CO poisoning happens when hydrogen is mainly produced by reforming hydrocarbons on-board and its influences on impedance spectrums were shown in [25]. From these studies, it proves that EIS is a capable and promising technique for revealing internal fuel cell faulty conditions.

Several previous works have discussed the degradation mechanisms of an FCS [2], [26], [27]. In [2], it is shown that fast transients could cause a stack of inappropriate water management and differential pressure of the membrane, leading to mechanical stresses, and fuel/oxygen starvations. To further promote the understanding of the fuel cell degradation process, a data challenge was initialized in 2014. The data is now made available online [28]. Prognostics of fuel cell stacks is an increasingly interesting field of research [3]. Voltage is the most important and accessible quantity for the remaining useful life (RUL) estimation, which has been extensively considered in [29]- [33]. In these works, the fuel cells were normally used in stationary applications, while the RUL estimation is more challenging when the voltage varies dynamically with different current demands in vehicular applications. Therefore, the case under dynamic load cycles was explored in [34]. Despite the voltage, EIS was also considered as a promising candidate for degradation estimation. In [12], the fuzzy cluster based on impedance spectrum parameters was adopted to distinguish the age of an FCS. Moreover, the parameters of an ECM were used to indicate the degradation of an FCS [13] under low frequency ripples.

The impedance spectrum from EIS is commonly interpreted by an ECM. Different conditions of an FCS are mapped to the variations of parameters in an ECM. As fuel cells vary from manufacturer to manufacturer, various impedance models were proposed to this end. A few example ECMs from previous literature are illustrated in Fig. 1.4, where different electrical components are used to represent various phenomena in a fuel cell. ECM in Fig. 1.4 (a) was adopted in [9] for flooding and drying diagnosis, in which R_m is ohmic resistance; R_p is the polarization resistance; Z_{CPE} represents the double layer effect; and Z_w is related with the diffusion process. Fig. 1.4. (b) was proposed in [23] to fit the impedance spectrum from a 1.2 kW Nexa PEM fuel cell at low current demands. Here R_m is ohmic resistance; $R_{ct,A}$ is the charge transfer resistance at the anode; $R_{ct,C}$ is the charge transfer resistance at the cathode; $Z_{CPE,A}$ represents the double layer effect at the anode; $Z_{CPE,C}$ represents the double layer effect at the cathode; and Z_w is related with the diffusion process. The dataset from the 2014 IEEE PHM Data Challenge Competition [28] was fitted by the ECM in Fig. 1.4 (c) and yields the best results of degradation prediction [35]. In this subfigure, R_m is ohmic resistance; R_1 is the charge transfer resistance at the anode; R_2 is the charge transfer resistance at the cathode; Z_{CPE1} represents the double layer effect at the anode; Z_{CPE2} represents the double layer effect at the cathode; R_3 and L_1 represent inductive related side reactions; and L_2 represents the inductor of external wires. An ECM with all linear elements, named Randle circuit, is illustrated in Fig. 1.4 (d) and was adopted in [36], [37] for hydrogen leakage identification and degradation analysis accelerated by low-frequency oscillations [13]. Here, R_m is ohmic resistance; R_{ct} is the charge transfer resistance; and C_{dl} represents the double layer effect. In these ECMs, traditional linear elements, such as resistors, capacitors and inductors, were used as well as non-linear ones, such as constant phase element Z_{CPE} and Warburg element Z_w. A necessary step for using ECMs is finding the values of circuit parameters with a fitting algorithm. With the increasing complexity of the model, the optimization process of a fitting algorithm is sensitive to initial values, may fail into local minimal and returns error circuit parameters. This was discussed and address in [38].

Several diagnostic methods were proposed using fuel cell impedance spectrums. A fuzzy system was used to mine the diagnostic rules and implement the diagnostic system in [11]. Neural networks were adopted for quantifying the leakage while fuzzy rules were used to implement it online in [24]. In [17], the parameter of an ECM is correlated to the oxygen reduction rate in a fuel cell. An ECM was built for modeling the degradation trend of the 1.2 kW Nexa module accelerated

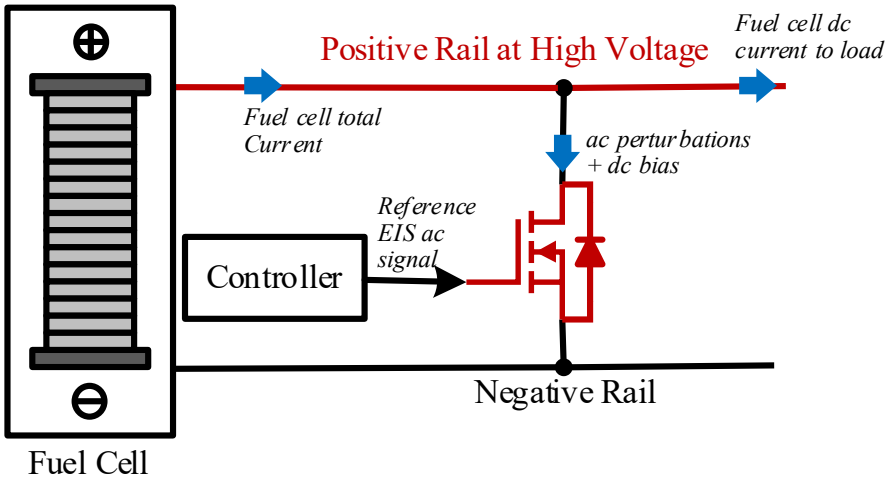

Fig. 1.5. Fuel cell EIS by ac perturbations generated from a power MOSFET in linear mode.

by low frequency ripples [13]. The ECM approach was also used for diagnosing water related faults in [9]. In this approach, the parameters of an ECM are used to best describe different internal conditions. The root cause that EIS results can be used for diagnostics is that the shape of an impedance spectrum changes according to different fuel cell internal conditions, therefore, features or signature points can be extracted to represent its shape. Three fixed frequencies were excited to describe the shape of impedance spectrums in [39]. The maximal absolute phase and the difference between polarization and internal resistances were identified as two signatures of a fuel cell impedance spectrum [12]. Significant features were found by fuzzy based rule-mining in [11] and dc current and angles between the frequency decades from 1 kHz to 100 Hz and 1 Hz to 0.1 Hz were selected as the features in [40]. Overall, these diagnostic methods tried to obtain the best and simplest signatures to describe the shape of an impedance spectrum that is most sensitive to faults or degradations.

1.2.2 Previous Works on Converter based EIS

Linear instruments based EIS tools were normally used for single-cell or short-stack testing [41] but are constrained by their low power ratings and high expense when used for high-power applications. The illustrative diagram in Fig. 1.5 shows the use of a power metal–oxide–semiconductor field-effect transistor (MOSFET) in its linear region to generate ac perturbations for triggering the EIS, where the main portion of dc energy is pulled by a dc load setting the dc operating point of the fuel cell. The power MOSFET is controlled by a reference EIS ac signal. It

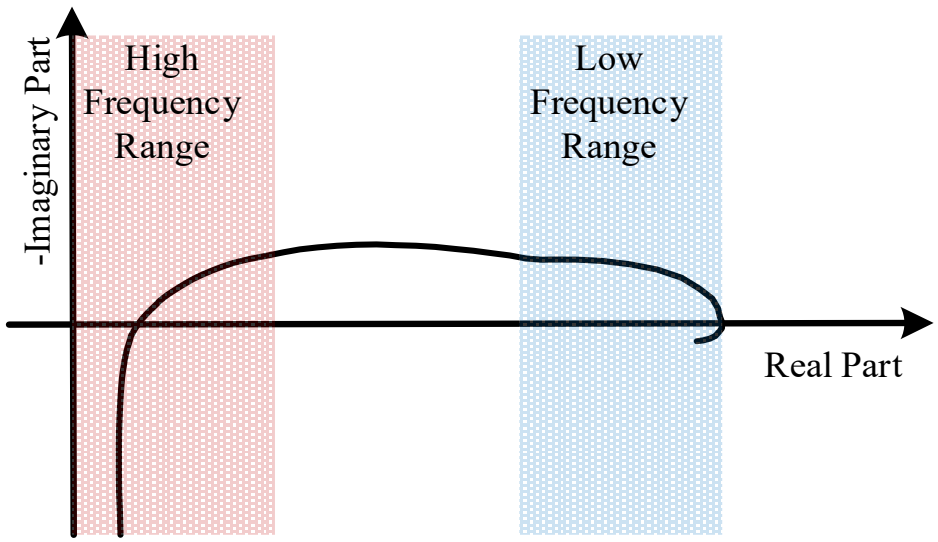

Fig. 1.6. An illustrative diagram of an impedance spectrum of FCS with two extremes in frequencies highlighted.

is noted here that a dc bias is necessary for operating the MOSFET and this bias should be counted into the dc operating point of the fuel cell. Therefore, the MOSFET passes both the ac perturbations and dc bias, and connects with the high-voltage FCS, leading to high power losses, and this portion of power is expected to be dissipated through the MOSFET. For high-power stacks, this solution is difficult to be achieved with regular linear power MOSFETs and involves significant challenge in the thermal design. Therefore, linear instruments are not suitable to be adopted for stack-level EIS operations.

In the converter based EIS solution, by controlling the switching actions of a power converter, the right excitation signals can be generated to the FCS. It was proposed in [42] and [43] that the switching ripples from converters can be used for fuel cell humidification diagnostics. In [44], switching ripples combined with low-frequency ac sinusoidal perturbations were proposed to extend the diagnostic frequency range. Ac perturbations using dc/dc boost converters were further explored in [45] and [20], where PI controllers were adopted, and high-frequency perturbations are accomplished through directly increasing the switching frequencies. EIS was integrated into an isolated converter in [46] to detect impedances from 2.5 Hz to 500 Hz. Superimposed multi-sine signals were generated with the power converter to a low-power FCS in [45] using a battery to hold the load voltage. A fuel-cell-battery hybrid system was also proposed in [46], achieving

EIS frequency range from 0.1 Hz to 1 kHz with a 100 kHz switching frequency. To increase the accuracy of ac perturbations from a PPC, model predictive control was proposed in [47], however resulting in complex controller designs. A parallel connected dc/dc converter was proposed in [48], [49], specifically designed for producing ac perturbations. The converter based EIS approach was also applied to batteries in [50]-[54]. Elmo Piccolo motor controller with the maximal bandwidth of 3.2 kHz was used in [50] to generate needed perturbations. EIS was also adopted in the dc/dc boost converters for performing EIS in battery applications [51], [54]. Furthermore, it was embedded in the battery management system in [53], and high-power battery chargers in [52]. By replacing linear instruments with switching power converters and moving it from offline to on-board, EIS is incorporated as an extra function of a PPC when impedance calculation is included in the same converter digital controller. This enables the capabilities of conducting impedance detection at stack levels and in real-time, leading to a complete diagnostic tool using the obtained impedance information. However, few unresolved issues of converter based EIS still remain.

1.2.3 Unresolved Challenges

Previous works mainly focused on realizing the concept of converter based EIS by adding the perturbation references to the converter control loop, while neglecting the frequency range for an effective and informative EIS operation. As illustrated in Fig. 1.6 of a typical fuel cell impedance spectrum, the significant frequencies required for a wide-range EIS of an FCS normally lies between only a few hertz (or even sub-hertz) and a few kilohertz [42]-[54]. The results of EIS at different frequencies reflect various statuses of an FCS. For example, impedances at high frequencies indicate the humidification level of the membrane, which is capable of diagnosing flooding and drying conditions [42]-[44], while impedances at the low end are responsible for mass transport process, which were used for detecting hydrogen leakage and/or oxygen concentration [36], [37] and degradation analysis [12], [35]. However, previous works neglected the practical hardware constrains on achieving the wide frequency range in the converter based EIS solutions. Moreover, the influences from EIS on the interconnected system and the practical implementation and design considerations of this technique in the field are not well considered.

In [42] and [43], switching ripples from the converters were used as the source of perturbations, while the EIS frequency was fixed to the converter switching frequency. This method cannot work in the lower frequency range and it is difficult to measure the phase of impedances. ac perturbations

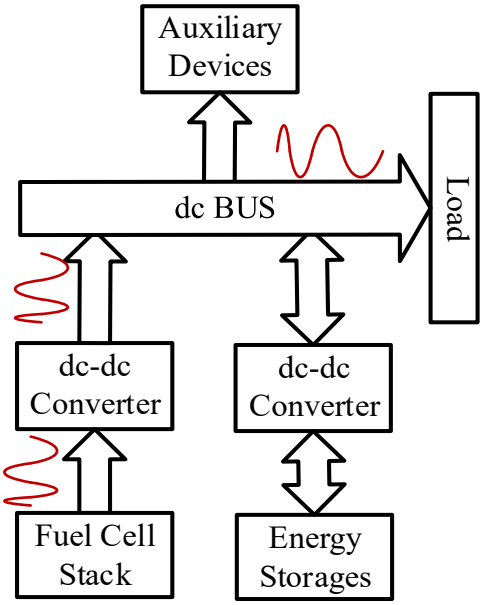

Fig. 1.7. The transfer of oscillations in a hybrid fuel cell powertrain incurred by EIS operation.

with a wider frequency range were achieved by adopting PPC designs with MOSFETs switched at high frequencies (over 100 kHz) in [44]-[46]. These designs, however, fall short of being practical solutions in higher-power applications such as in a heavy-duty vehicle powertrain. In practical implementations, the switching frequency is normally limited due to the switching loss in high-power applications, especially with the hard-switched topologies used in [44]-[49]. Considering the power and voltage rating requirements, such applications normally favor Si insulated gate bipolar transistors (IGBTs) as the dominant power device choice for the PPC due to their maturity and lower cost, where the switching frequency is usually limited to below 20 kHz. Even with silicon carbides (SiC) MOSFETs that have been adopted in a few new designs [55], a switching frequency over 100 kHz is rarely achievable considering the significant switching losses in high-power applications. Moreover, the bandwidth of the PPC controller is further limited by the computational delay and zero-order hold (ZOH) effect associated with a digital implementation. Up to now, no simple and effective method is available to induce high-frequency perturbations with a limited switching frequency in high-power fuel cell powertrains.

On the other hand, the ac current perturbations generated at the input side of a PPC propagate to its output side, showing as significant oscillations on the dc bus voltage in a powertrain, especially for low-frequency EIS perturbations, as illustrated in Fig. 1.7. In this figure, a typical hybrid fuel cell powertrain is demonstrated, where the fuel cell converter is used to generate ac

current perturbations at the fuel cell port for fuel cell EIS. These perturbations will cause voltage oscillations on the dc bus. Due to the nature of EIS, the frequency of excitations can be as low as few sub-hertz, and its magnitude is normally set to 5%-10% of the fuel cell output current. Hence, it poses a great challenge on a powertrain which is usually designed with considerations of only the switching ripples coming from the converters. It is essential to ensure the upper swing of the oscillation on the dc link voltage does not exceed the electrical ratings of the connected components, and the lower swing to be at least higher than the fuel cell output voltage for maintaining the proper boost operation to modulate the sinusoidal ac perturbations in a commonly used boost-derived fuel cell PPC. Moreover, if the EIS mode is triggered when the motor is operating in an FCV powertrain, it is necessary that the magnitude is attenuated to a certain degree. Typical controllers for motor drive inverters are designed with nearly constant dc bus voltages, and an oscillating dc bus can introduce significant harmonics on the inverter's outputs [56]. Though the EIS is usually operated for short periods, as pointed out in [57], large oscillations may cause heavy torque ripples at the same frequency on the propulsion motor, leading to mechanical stresses on the shaft. Moreover, if large oscillations are excited at the resonant frequency of the inverter, which is highly possible with EIS excitations triggered at various frequencies to obtain rich information, the excessive torque ripples may endanger the safety of the entire system. To the best of the author's knowledge, oscillations brought by the converter based *in situ* EIS were never addressed previously.

To expose the full potentials of an EIS operation and obtain rich diagnostic results, perturbations at various frequencies at both high and low ends are expected to be generated from the PPC. Impedances obtained at a wide frequency range help with extracting more information related to the internal conditions of an FCS since the measured impedances at specific frequencies reflect specific internal phenomena. Moreover, accurate parameters can be obtained with more impedance data in fitting an ECM of FCS. This requires the frequency range of EIS and the characteristics of an FCS are taken into consideration in the designing and controlling of a power converter to generate needed ac perturbations. Overall, further research is needed in this area to develop more practical and improved solutions for converter based fuel cell EIS.

1.3 Summary of Contributions and Outline of the Thesis

Facing the challenges and gaps between previous works in this area and the practical implementation needs for *in situ* EIS triggered by converters for high-power FCS, this thesis presents a comprehensive research to improve the readiness of converter based EIS in practical applications. The presented work focuses on enabling a wide range of perturbations generated by switching power converters to high-power stacks and variations of converter based EIS units. To this end, a series of methods and analyses are proposed and conducted.

Compared with previous works, the proposed solutions aim to tackle neglected issues in the literature. Firstly, the limitation of converter controller bandwidth was not considered and analyzed previously when implementing *in situ* EIS with the fuel cell on-board PPC. Chapter 2 addresses and resolves this issue by adopting the PI plus resonant controllers. Moreover, an impedance processing method with minimal computational requirements is proposed as well, forming a complete EIS based diagnostic approach with the existing PPC hardware. Secondly, the influences of oscillations from EIS operations enabled by the main PPC on a typical hybrid fuel cell powertrain are systematically analyzed in Chapter 3. Chapter 4 presents a main PPC design approach by considering both the fuel cell output characteristics and embedding the wide-frequency-range EIS excitations while eliminating EIS oscillations to the load side. Lastly, Chapter 5 presents a flexible auxiliary converter module for generating ac perturbations, separating the main power processing stage of FCS and the ac perturbation source.

The contributions and details of each chapter are summarized as follows.

1.3.1 Converter based EIS for High-Power Fuel Cell Stacks with Resonant Controllers

Chapter 2 recognizes the limitations on generating high-frequency ac perturbations using high-power converters, as converter based EIS is intended for stack-level testing or directly incorporated in stationary or mobile powertrains. The switching frequencies are constrained in the high-power converter modules, and thus, limiting the control bandwidth. Therefore, needed effective high-frequency perturbations for EIS cannot be excited, which can be a few kilohertz. To this end, the resonant controllers are proposed in this chapter to include high-frequency perturbations for converter based EIS in high-power applications. The detailed design of resonant controllers for this application is elaborated and verified with experiments. In the end, EIS ac perturbations at 2 kHz are achieved given an IGBT based three-phase interleaved dc/dc converter switched at the 10

kHz switching frequency. With the high frequencies enabled by the proposed resonant controllers, a new diagnostic method utilizing the measured impedances for health evaluations of an FCS is also presented. As just one application example taking advantage of the capabilities of the proposed EIS method, the presented diagnostic approach features high sensitivity to impedance changes in the FCS and is fast and computationally inexpensive, making it suitable to be incorporated directly into the digital controller of the PPC. Together with the *in situ* EIS and impedance calculations, they complete an efficient solution for condition monitoring of high-power FCS without the need for any hardware changes.

1.3.2 Oscillation Analysis in Fuel Cell Powertrain Brought by Converter based EIS

This chapter presents a comprehensive analysis of the oscillations brought by the converter based EIS, especially on the common dc link in a typical hybrid fuel cell powertrain. Such influences from integrating EIS to the PPC were neglected previously, not to say, a systematic analysis. Aiming at filling this gap, this chapter focuses on the oscillations brought by *in situ* converter based EIS operation and their transfer in a typical hybrid fuel cell powertrain. Small signal analysis is applied to derive the mathematical expressions of the oscillations that can appear on the common dc link. Various factors in this setting are considered and their influences on the oscillations are revealed. The presented results indicate that it is favorable to operate EIS during the motor is idling. The oscillation on the dc link reaches its maximum at the resonant frequency of the energy storage converter, while its magnitude is influenced by various factors, i.e., system parameters and operating conditions. Moreover, it is found that the worst-case condition of oscillation can be determined by a healthy stack at the beginning of its life. The presented analysis forms a basis on providing guidelines for hybrid fuel cell powertrain designs where the intended ac perturbations generation are implemented by on-board power converters.

1.3.3 Fuel Cell Oriented Design of an CF Isolated Converter with a Wide-Frequency-Range EIS

The limitations of achieving frequencies at high and low ends are revealed, where the high end is constrained by converter control bandwidth and the low end causes significant ripples on the output. A type of converter is adopted to address these issues to this end. It is designed considering the output characteristics of an FCS to achieve the decoupled control and soft switching. Therefore,

given the high efficiency, high-frequency perturbations are excited with the extended switching frequency. On the other hand, the oscillations, especially low-frequency ones, occurred from EIS operation are tackled by guiding the oscillations from the load side to the primary side energy storage (PSES) in the proposed converter topology. In the end, a fuel-cell-dedicated PPC capable of presenting a wide frequency range of perturbations is achieved. A design case is presented, and its experimental results reveal the effectiveness of the proposed converter in this chapter.

1.3.4 A New Auxiliary Converter Solution for Generating ac Perturbations for FCS EIS

This chapter proposes an auxiliary converter used for generating ac perturbations enabling *in situ* EIS in the powertrains of automotive or stationary power supplies, or in an offline testing bench. The auxiliary converter is independent of the main power transfer path in the powertrain as an add-on component, dedicated for EIS operations. Therefore, on-board EIS is brought to an FCS without any modifications to the existing design of the fuel cell powertrain. It processes pure ac current perturbations with only a sized energy buffer on the load side, featured with great flexibility. The conceptual illustrations as well as detailed designs are given in this chapter. Finally, experimental verifications are presented.

Chapter 2 Converter based EIS for High-Power Fuel Cell Stacks with Resonant Controllers

As discussed above in section 1.2.3, the bandwidth of the fuel cell PPC is constrained in high-power applications due to high switching losses, and therefore the high-frequency perturbations cannot be achieved with the existing PPC of an FCS. The proposed methods in this chapter addresses this limitation, leading to an *in situ* diagnostic tool using existing PPCs. As a total software method, this approach can be used to retrofit fuel cell systems to incorporate the EIS function for advanced diagnostics.

To achieve quality high-frequency ac perturbations and enable PPC-based EIS for high-power FCS in a wide frequency range, this chapter proposes a new solution by incorporating the combination of PI and resonant controllers in the PPC's current control loop. In fact, as high bandwidth is not necessarily required during the normal operation of an FCS, therefore a PI controller can be readily used in this operation. The resonant controllers are designed as a plug-in module to be used only during the EIS operation, and each resonant controller is designed to provide a high gain at the needed EIS frequency, corresponding to the imposed ac perturbations reference, to achieve high quality ac perturbations. By properly shaping the control loop with parallel-connected resonant controllers, ac perturbations are generated with high accuracies using the PPC. Compared with previous works on converter based EIS, the proposed solution does not require a redesign or modification of the PPC hardware and produces high quality ac perturbations in a wide frequency range with only updates to the PPC controller firmware. It provides a practical and effective means to enable wide frequency range EIS in high-power systems where the PPC's switching frequency is constrained by its power semiconductor devices.

With the wide frequency range converter based EIS tool, a new diagnostic method utilizing the measured impedances for health evaluations of an FCS is also presented. As just one application example taking advantage of the capabilities of the proposed EIS method, the presented diagnostic approach features high sensitivity to impedance changes in the FCS and is fast and computationally

inexpensive, making it suitable to be incorporated directly into the existing digital controller of the PPC. Together with the *in situ* EIS and impedance calculation, it completes an efficient solution for diagnostics of high-power FCS without the need of any hardware changes.

This work intends to contribute by addressing the gap between previous converter based EIS efforts and the practical application of this concept in high-power FCS systems. By the proposed use of PI plus Resonant controllers on the FCS converter with a limited switching frequency, it enables a wide frequency range EIS at minimal cost. Hence, efficient diagnostic algorithms can be developed utilizing the rich information offered by the extended frequency range. It also contributes by proposing the example application of the EIS tool with the health indicators (HIs) created from impedance information in different frequency regions. With the demonstrated sensitivity to FCS impedance changes, they provide better recognition of FCS internal phenomena than the terminal voltage alone. A complete software-based approach which can be incorporated as an advanced health monitoring function into the converter controller is thus obtained.

The rest of the chapter is organized as follows: Section 2.1 explains the basic operating principles and system descriptions of the fuel cell converter where EIS is integrated, as well as the proposed resonant controllers. Section 2.2 describes the design of the proposed resonant controllers for producing high-frequency ac perturbations with the PPC and the impedance calculation technique in details. Experimental verifications of the proposed method on a laboratory prototype using an emulated fuel cell and an example application of using it for FCS fault diagnostics are presented in section 2.3, where it provides an efficient approach of utilizing the detected impedances and can be directly incorporated into a converter controller. Therefore, it completes a fully software updates for existing high-power converter to included EIS based diagnostics for FCS. Conclusions are given in section 2.4.

2.1 System Description

As shown in Fig. 2.1, in a typical hybrid FCV powertrain, with converter based EIS implemented, the PPC can be leveraged to perform advanced diagnostics enabled by proper control and impedance calculation using the existing sensors of the converter. The diagnostic algorithm can be embedded in the converter controller to report the real-time condition of an FCS once an EIS operation is completed. Hence, EIS can be embedded as an additional function of a PPC in this approach.

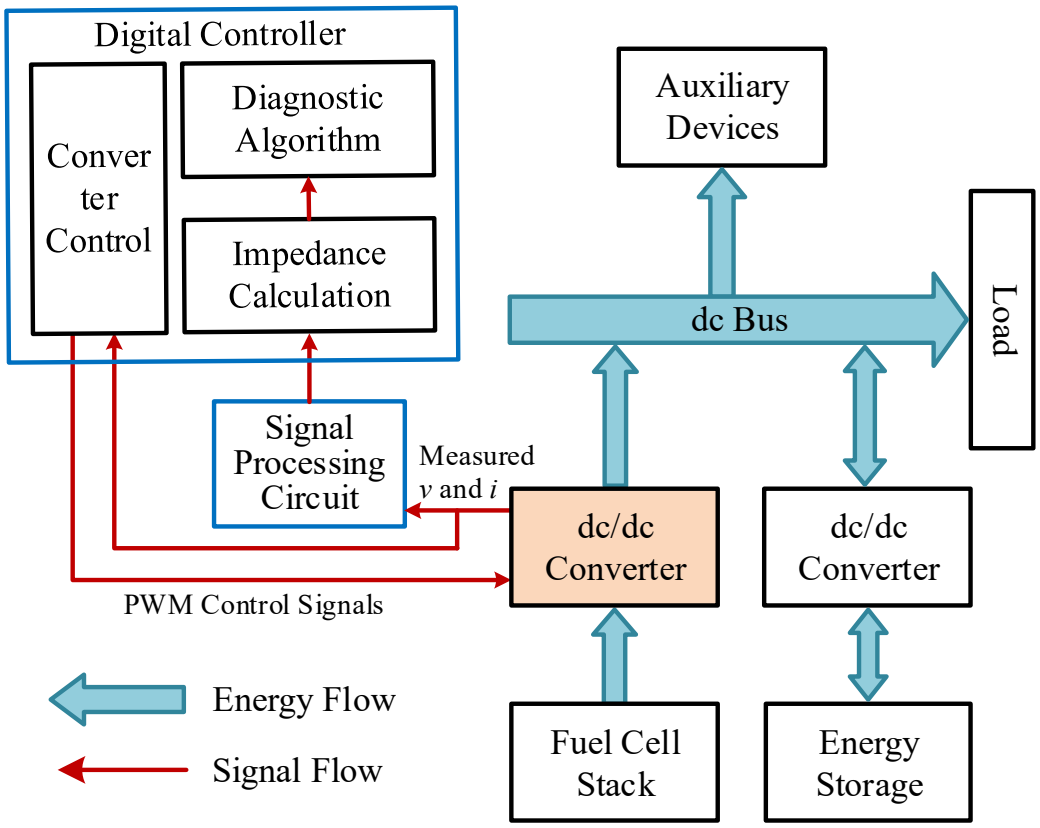

Fig. 2.1. Simplified block diagram of a hybrid fuel cell powertrain with converter based EIS embedded for on-board diagnostics of the fuel cell stack.

In applications such as FCVs, due to the low-voltage high-current output characteristics of the FCS, an *n*-phase interleaved boost converter is a popular topology choice for its PPC. As shown in Fig. 2.2, S_{fc1} -S_{fcn} and D_{fc1}-D_{fcn} are the switching devices (e.g., IGBTs) and power diodes of the boost converters on phases 1~n, and L_{fc1}-L_{fcn} and R_{fc1}-R_{fcn} are the phase inductors and the equivalent phase resistors. C is the dc-bus capacitor, and the load are modeled as a resistor of R_L. The fuel cell output voltage is V_{fc} and I_{fc1}-I_{fcn} are the currents at each phase. In a typical hybrid configuration, the load voltage is regulated to V_o by an ESU converter, e.g., a battery or a supercapacitor, connected to the dc bus via a separate dc-dc converter. The purpose of the ESU includes assisting with the start-up process of the FCS and absorbing fast load dynamics during driving conditions. The interleaved boost converter controls the output current of an FCS and determines its dc operating point.

The current of each converter phase is controlled separately with a reference equaling to $1/n$ of the total fuel cell current. Here, averaged current mode control (ACMC) with a one-sample-per-

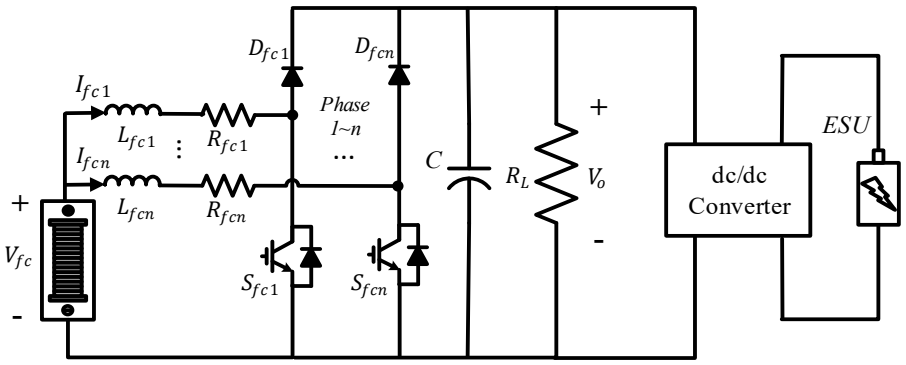

Fig. 2.2. High-power FCS with an *n*-phase interleaved boost converter as the PPC.

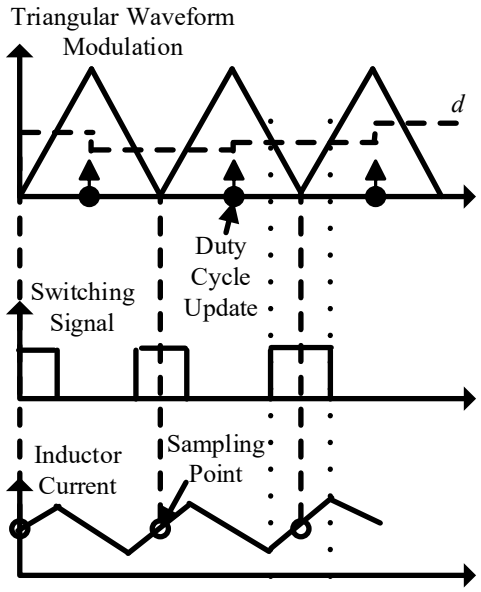

Fig. 2.3. Switching and sampling patterns of ACMC in each phase of the interleaved boost converter.

cycle approach is adopted for the phase current control. The sampling and duty cycle updating patterns of the ACMC are illustrated in Fig. 2.3 for each phase. The sampled current is the averaged current over one switching period eliminating the interferences of the switching noise. The voltage responses are sampled synchronously for impedance calculation during the EIS operation. The number of sampling points in each switching period is *n* with the interleaved structure, and thus *n* times of the averaged values are obtained for each period of ac perturbations during the EIS as compared with a single-phase converter. Hence, the maximum frequency of the EIS can be pushed

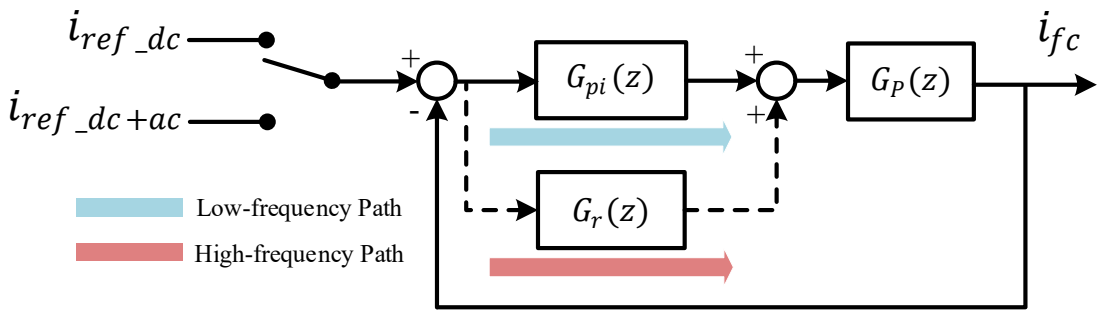

Fig. 2.4. Proposed current control loop with PI and resonant controllers for FCS PPC with the resonant controller assisting with quality high-frequency ac perturbations.

higher with more converter phases in interleave with the same number of sampling points for impedance calculation.

Fig. 2.4 shows the current control loop of each converter phase. The current reference only sets the dc operating point, and a PI controller is used during normal operation. After the triggering of an EIS operation, the current reference is switched to a combination of the dc operating point and an ac perturbation at the needed EIS frequency. The dc component is still mainly regulated by the PI controller, while the parallel resonant controller designed at the frequency of the ac perturbation is engaged to make the path for the high-frequency components. The resonant frequency creates a high gain at the selected frequency, therefore enables achieving high quality ac perturbations at higher frequencies. With this arrangement, the PI controller mainly regulates the dc operating point whereas the resonant controller provides a better tracking performance of the reference ac signals.

A digital controller is used to implement both the control and the impedance calculation. It allows easy switching between the normal and EIS operation modes. The plant is thus modeled in the discrete domain. Considering the equivalent series resistance of the power inductor, the continuous duty-cycle-to-current transfer function in the s-domain is

$$G_p(s) = \frac{V_o}{L_{fc}S+R_{fc}} \tag{2.1}$$

With the ACMC scheme, the computational delay is fixed to half of the sampling period; and the pulse-width modulation (PWM) effect is modeled with ZOH discretization. The discrete transfer function of the control plant is thus derived as

$$G_p(z) = (1-z^{-1})Z_m[e^{-0.5sT_s}\frac{V_o}{s(L_{fc}S+R_{fc})}] \tag{2.2}$$

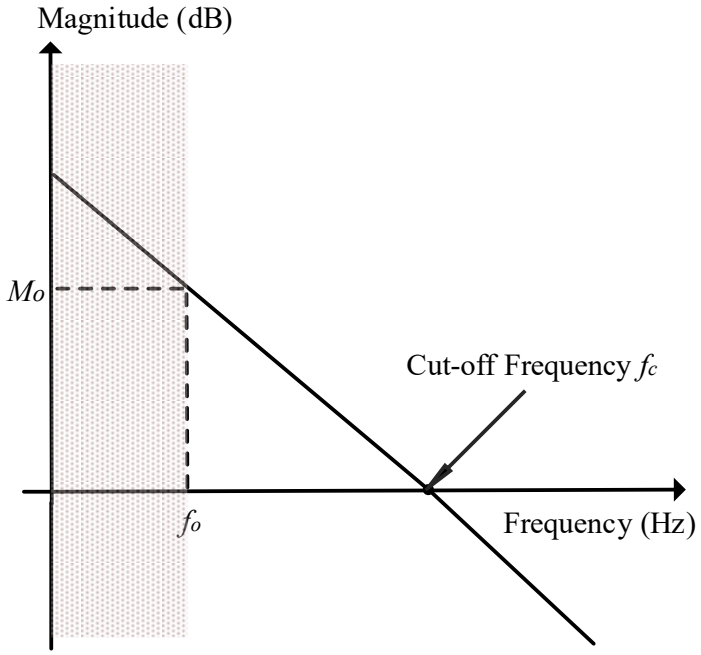

Fig. 2.5. FCS PPC current control loop illustration with a PI controller only.

where $Z_m[\cdot]$ is the modified Z transformation [26] with half sample delay and T_s is the switching period of PPC. The plant model in the z-domain is

$$G_p(z) = \frac{V_o\left(1-e^{-0.5R_{fc}T_s/L_{fc}}\right)}{R_{fc}} z^{-1} \frac{z+e^{-0.5R_{fc}T_s/L_{fc}}}{z-e^{-R_{fc}T_s/L_{fc}}} \tag{2.3}$$

With (2.3), a PI controller is designed, where the proportional term K_p is used to set the cut-off frequency and the integral term K_i is found by the targeted phase margin. The transfer function of PI controller with Tustin discretization is

$$G_{pi}(z) = \frac{\left(K_p+K_iT_s/2\right)z+\left(K_iT_s/2-K_p\right)}{z-1} \tag{2.4}$$

2.2 Resonant Controller Design

Fig. 2.5 gives an illustrative diagram of the open-loop gain when a PI controller is adopted for the fuel cell output current control. The cut-off frequency f_c is normally set to 1/10 ~ 1/20 of the switching frequency f_s to ensure enough separation from the latter to avoid commutation noise. The maximum frequency of EIS, f_o, needs to be lower than the cut-off frequency to have a large enough magnitude of M_a [58], such that good tracking of the reference can be guaranteed. Hence, only frequencies below f_o are reachable for the EIS with PI controller alone whose bandwidth is limited by the f_s of the PPC.

To provide a high gain at selected higher frequencies for better tracking of the ac perturbation references during EIS operation, resonant controller is proposed here to be put in parallel with the PI compensator. Resonant controller is widely used in grid-connected inverters for sinusoidal reference tracking [59]. In this application, multiple resonant controllers are designed with different resonant frequencies according to the needed ac perturbation frequencies of the EIS.

A general non-ideal resonant controller in the s-domain is

$$G_r(s) = K_r \frac{s\cos(\varphi) - \omega_r \sin(\varphi)}{s^2 + \omega_r^2} \tag{2.5}$$

where K_r is the resonant controller gain, ω_r is the resonant frequency and φ is the phase compensation term.

Transferring (2.5) to the z-domain with frequency pre-warping discrete method ($s=\omega_r/\tan(\omega_r T_s/2)\times(z-1)/(z+1)$), the discrete resonant controller is given by

$$G_r(z) = \frac{K_r}{\omega_r} \frac{az^2 + bz + c}{z^2 + dz + 1} \tag{2.6}$$

in which $a = \frac{\sin(\omega_r T_s + \varphi) - \sin(\varphi)}{2}$; $b = [\cos(\omega_r T_s) - 1]sin(\varphi)$; $c = \frac{-\sin(\omega_r T_s - \varphi) - \sin(\varphi)}{2}$ and $d = -2\cos(\omega_r T_s)$.

In this application, the resonant peak appears at various frequencies according to the EIS needs. It increases the loop magnitude by creating a peak within or above the PI bandwidth. A resonant controller creates a sharp 180 degrees change in the phase plot and two more zero-magnitude crossovers in the magnitude plot when the resonant frequency is above the cut-off frequency set by the PI. The phase compensation φ needs to be carefully selected to ensure system stability.

The situation involving the resonant peak falling out of the controller bandwidth was discussed in [60] and stability margin was maximized with a geometric approach in the Nyquist plot. However, the method only considers a proportional plus resonant controller. In this work, as the proposed control structure for EIS is a PI plus resonant controller, the more generalized formulation proposed in [61] is adopted.

During EIS, the total open-loop gain is $G_p(s)[G_{pi}(s)+G_R(s)]$. The closed-loop error rejection function is expressed as

$$\begin{aligned} E(z) &= \frac{1}{1 + (G_{pi}(z) + G_r(z))G_p(z)} \\ &= \frac{1}{1 + G_{pi}(z)G_p(z)} \frac{1}{1 + G_r(z)G_p(z)/(1 + G_{pi}(z)G_p(z))} \\ &= E_1(z)E_2(z) \end{aligned} \tag{2.7}$$

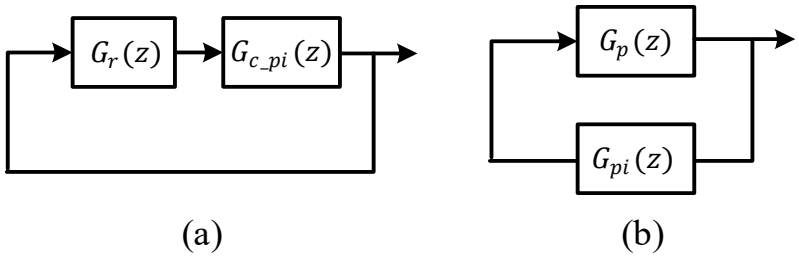

Fig. 2.6. Equivalent feedback loops: (a) $E_2(z)$; (b) $G_{c\_pi}(z)$.

To ensure system stability, the poles of $E(z)$ need to stay within the unit circle in the z plane. In (2.7), $E(z)$ is factorized, and the stability criterion becomes whether the poles of $E_1(z)$ and $E_2(z)$ are within the unit circle. From the formula in (2.7), $E_1(z)$ is the closed-loop error rejection function of normal operation with the PI controller. Its stability is ensured by properly designing the PI parameters. Thus, the stability of the system during EIS depends on the stability of the second function, which is given as

$$E_2(z) = \frac{1}{1+G_r(z)G_{c\_pi}(z)} \tag{2.8}$$

where $G_{c\_pi}(z) = G_p(z)/(1 + G_{pi}(z)G_p(z))$.

As shown in Fig. 2.6 (a) and (b), $E_2(z)$ is the closed-loop error rejection function of $G_r(z)$ and $G_{c\_pi}(z)$, whereas $G_{c\_pi}(z)$ is the closed-loop transfer function with a PI controller in the feedback path. Determining the stability of $E_2(z)$ is equivalent to determining the closed-loop stability of the loop in Fig. 2.6 (a), where the plant is $G_{c\_pi}(z)$ and the controller is $G_r(z)$. For an uncompensated $G_r(z)$, i.e., φ=0, the phase drops from 90 to -90 degrees at the resonant frequency. Adding the phase delay introduced by $G_{c\_pi}(z)$, the stability margin is reduced, or the phase plot would even cross -180 degrees, leading to an unstable system. System stability at the resonant frequency is ensured by letting φ compensate for the plant delay of $G_{c\_pi}(z)$, as in

$$\varphi = -\angle G_{c\_pi}(e^{j\omega_r T_s}) \tag{2.9}$$

Hence, the selection of compensation term is given in (2.9) and the controller gain K_r is set to 2000. Based on the system parameters given in Table I and the compensation terms calculated using (2.9), the system closed-loop pole map of four selected resonant frequencies at 100 Hz, 500 Hz, 1000 Hz, and 2000 Hz are presented in Fig. 2.7. It can be seen that all the poles stay within the unit circle indicating a stable system design with the PI plus resonant controller in EIS operation.

In an actual application, once the frequencies needed for EIS are selected, all the parameters of

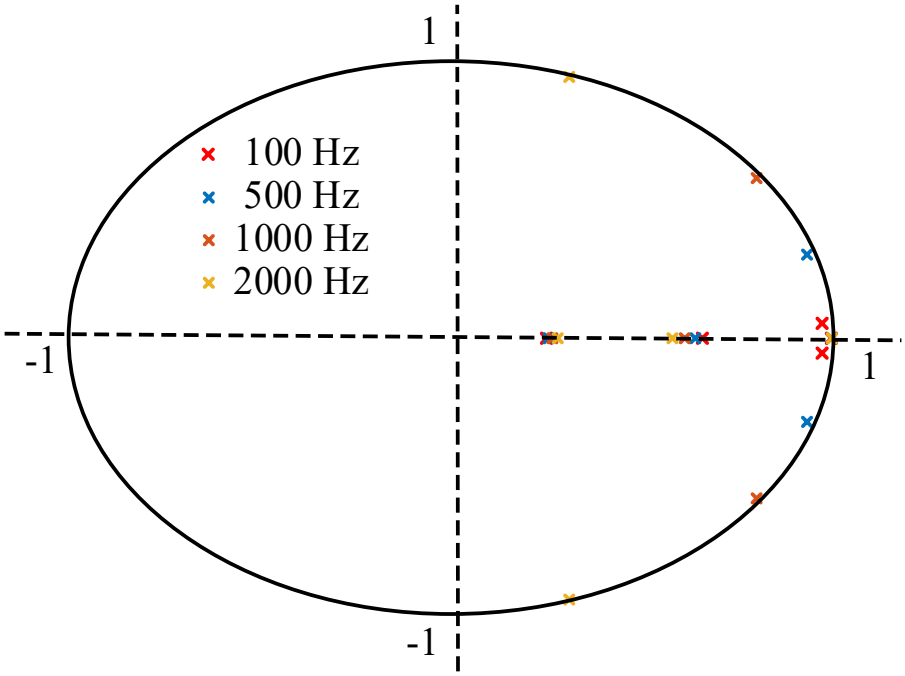

Fig. 2.7. Closed-loop pole map of the FCS PPC current control loop with resonant controllers at 100 Hz, 500 Hz, 1000 Hz and 2000 Hz.

the resonant controller can be calculated offline and stored in the memory of the digital controller.

In EIS mode, the measured current and voltage values are combinations of the dc component and ac perturbations. The amplitude of the ac current is 10% of the dc level as designed. As the response of the EIS perturbation, the ac voltage from fuel cell is

$$V_{ac} = -Z_m I_{ac} \tag{2.10}$$

where V_{ac} and I_{ac} are the magnitudes of the ac voltage and current, respectively; and Z_m is the FCS internal impedance to be calculated. As Z_m is normally only a few milliohms, the magnitude of V_{ac} is relatively low.

The FCS internal impedance is calculated with digital lock-in amplifiers. The measured current and voltage sampled by an ADC contain the dc components (I_{dc} and V_{dc}), the ac terms of EIS perturbations ($I_{ac}sin(\omega t_n+\theta_i)$ and $V_{ac}sin(\omega t_n+\theta_v)$), and higher-order terms plus noises ($n_i(t_n)$ and $n_v(t_n)$). The ac perturbation terms have amplitudes of I_{ac} and V_{ac} at the angular EIS frequency of ω with the phases of θ_i and θ_v respectively, as given in

$$\begin{cases} i(t_n) = I_{dc} + I_{ac}\, sin(\,\omega t_n + \theta_i) + n_i(t_n) \\ v(t_n) = V_{dc} + V_{ac}\, sin(\,\omega t_n + \theta_v) + n_v(t_n) \end{cases} \tag{2.11}$$

Multiplying the sampled current and voltage signals with $sin(\omega t_n)$ and $cos(\omega t_n)$ and applying

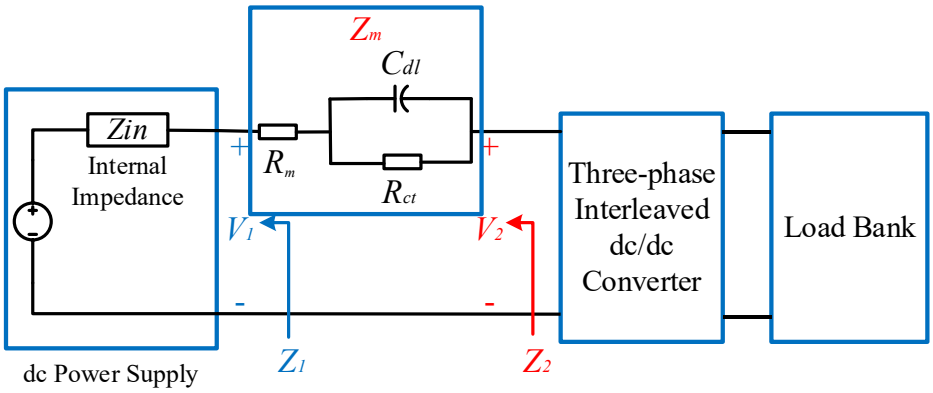

Fig. 2.8. Block diagram of the experimental setup.

low-pass filters (moving average filter is used here) to them, the amplitudes and phases of the ac perturbations are extracted as

$$\begin{cases} X_I = 0.5I_{ac}\, cos(\theta_i) \\ Y_I = 0.5I_{ac} \sin(\theta_i) \\ X_V = 0.5V_{ac} \cos(\theta_v) \\ Y_V = 0.5V_{ac}\, sin(\theta_v) \end{cases} \tag{2.12}$$

Hence, the real and imaginary parts of the FCS impedance are obtained by

$$\begin{cases} Re(\omega) = \frac{X_I X_V + Y_I Y_V}{X_I^2 + Y_I^2} \\ Im(\omega) = \frac{X_I Y_V - Y_I X_V}{X_I^2 + Y_I^2} \end{cases} \tag{2.13}$$

2.3 Experimental Verification

2.3.1 Experimental Setup

To verify the proposed method, a laboratory setup is built with a dc power supply (ITECH IT6535C) for producing the dc voltage, emulation circuits of resistors and capacitors for emulating the FCS impedance, a three-phase interleaved dc/dc boost converter (Semikron SKiiP_613_GD123) as the PPC, and a digital controller platform built around a TMS320F28335 microcontroller. Fig. 2.8 shows the block diagram of the setup. All the control and impedance calculation algorithms are implemented in the digital controller. A load bank is configured to constant resistance mode to emulate the load demand for the FCS, assuming the load dynamics are absorbed by energy storages or dumping resistors. The testing equipment used are Tektronix DPO2014 digital oscilloscope, Tektronix TCP0030 current probe and P5205A-NEW high-voltage differential probe.

Table 2.1. Experimental System Parameters

Parameter		Value	Parameter		Value
L_{fc1}, L_{fc2}, L_{fc3}		1 mH	R_{fc1}, R_{fc2}, R_{fc3}		5 mΩ
V_o		70 V	f_s		10 kHz
V_{fc_oc}		48 V	*# of phases*		n = 3
Case I	R_m	0.1397	Case II	R_m	0.3398
	R_{ct}	0.0742		R_{ct}	0.0732
	C_{dl}	0.03		C_{dl}	0.03
Case III	R_m	0.1399	Case IV	R_m	0.1361
	R_{ct}	0.1476		R_{ct}	0.0746
	C_{dl}	0.03		C_{dl}	0.02

The FCS is assumed to be operating in a current-controlled mode, emulated by the dc power supply producing a 45 V output and the impedance emulation circuits built from a linear ECM. With the system parameters given in Table 2.1, four different emulation circuits are tested in the experiments. Case I is a base case, whereas the other three are obtained by modifying one parameter of the ECM. The parameters of Case I are chosen to closely emulate the internal impedance of a 1.2 kW Nexa module [13]. It should be noted that compared with an actual FCS, the adopted experimental setup may have certain inaccuracy brought by the emulation circuit elements and the switching mode dc power supply. As the values of power resistors are affected by the temperature, they are re-measured before each EIS operation. It should be noted that because the dc power supply is in fact a switching converter with an internal impedance varying with frequency, its effects on the experiment are considered. The voltage outputs across the dc power supply and after the impedance emulation circuit, shown in Fig. 2.8 as V_1 and V_2 respectively, are both measured and two impedances, Z_1 and Z_2 in the figure, are calculated. The impedance needed for the EIS is their difference, Z_2- Z_1.

2.3.2 Experimental Results

With a 10 kHz converter switching frequency, the designed parameters of PI give a cut-off frequency of 500 Hz and a phase margin of 60 degrees. To demonstrate the proposed control

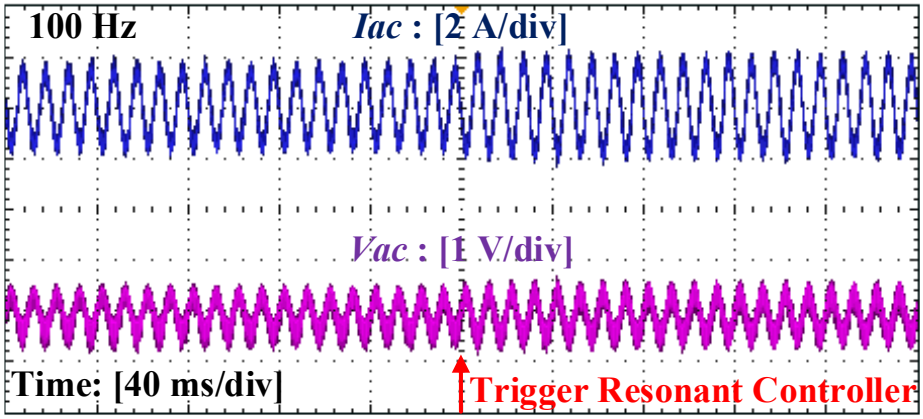

Fig. 2.9. Experimental result of 100 Hz ac current perturbation.

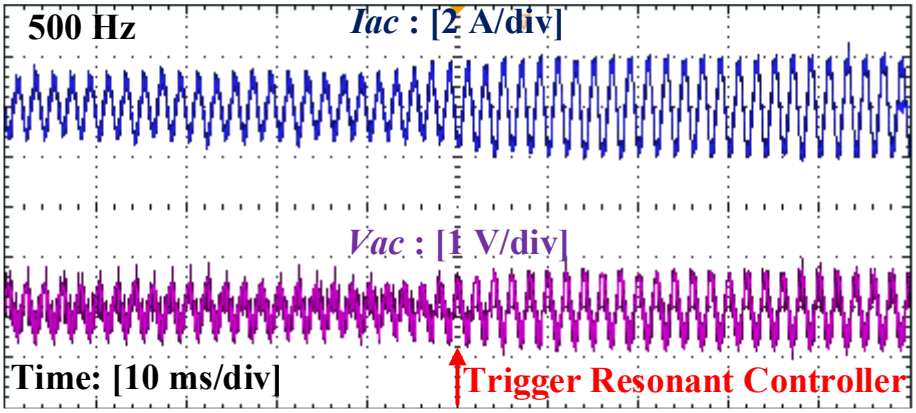

Fig. 2.10. Experimental result of 500 Hz ac current perturbation.

architecture, four resonant controllers are designed with resonant frequencies at 100 Hz, 500 Hz, 1000 Hz, and 2000 Hz. The one at 100 Hz is designed within the cut-off frequency to increase the magnitude of the control loop. The other three create magnitude peaks at and above the cut-off frequency.

Fig. 2.9- Fig. 2.12 provide the experimental waveforms of the ac current perturbations and the resultant voltage responses obtained at the four selected frequencies with the Case I emulation circuit. Results achieved with PI controller alone at the beginning and with the resonant controllers triggered afterwards are both shown in the plots.

As can be seen, the PI controller alone can still provide satisfactory tracking performance at 100 Hz. However, as the required perturbation frequency increases, the PI controller no longer can

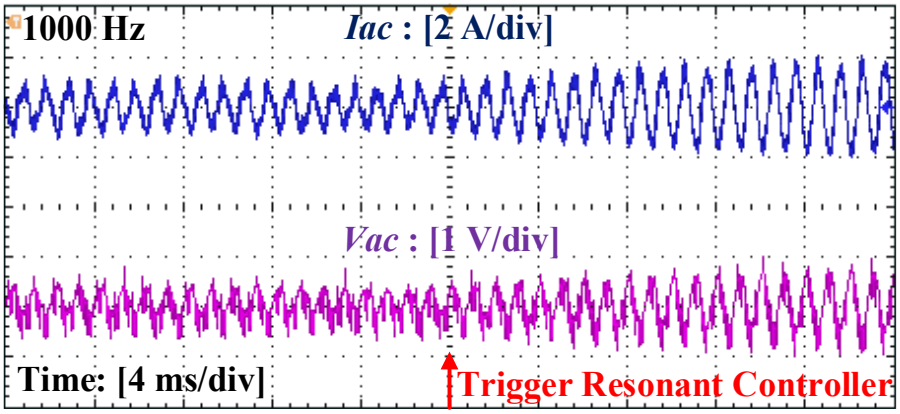

Fig. 2.11. Experimental result of 1000 Hz ac current perturbation.

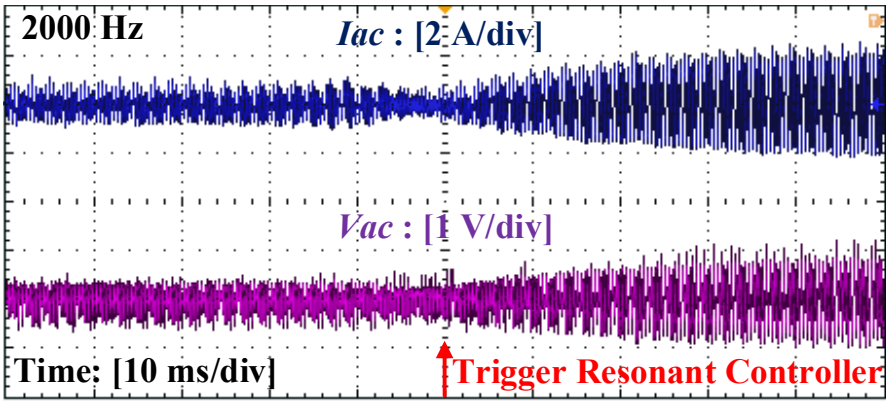

Fig. 2.12. Experimental result of 2000 Hz ac current perturbation.

generate the needed sinusoidal excitations properly. Satisfactory sinusoidal waveforms are produced only when the resonant controllers are enabled to assist. At higher resonant frequencies, fewer sampling points are taken in each perturbation period. For example, when the resonant frequency is set to 2000 Hz, only 5 switching and sampling instances take place in each perturbation period with a 10 kHz converter switching frequency, as shown in Fig. 2.13 (a). With three-phase interleaving operation a total of 15 averaged values are sampled, leading to a good quality sinusoidal waveform as shown in Fig. 2.13 (b). The resonant frequency is less likely to be pushed higher as satisfactory result will not be achieved with fewer instances of switching in each perturbation period.

Fig. 2.14 demonstrates the detected impedances from the experimental setup at various frequencies with the Case I emulation circuit. The samples at 100 Hz and below are generated with

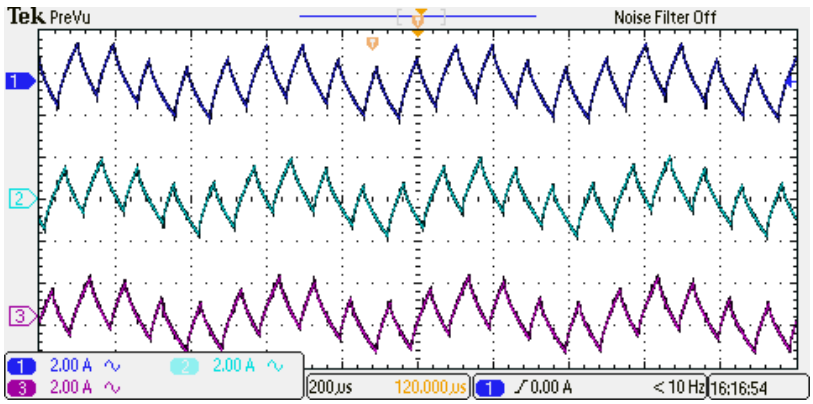

(a)

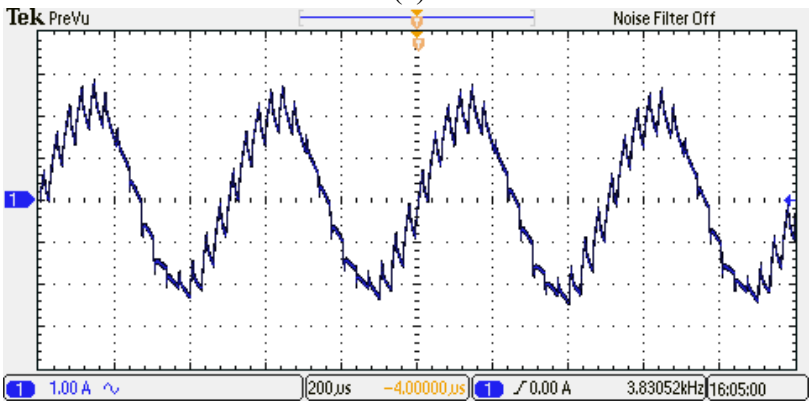

(b)

Fig. 2.13. Zoom-in experimental results of 2000 Hz ac current perturbation: (a) three-phase current (2 A/div and 200 us/div) and (b) total output current (1 A/div and 200 us/div).

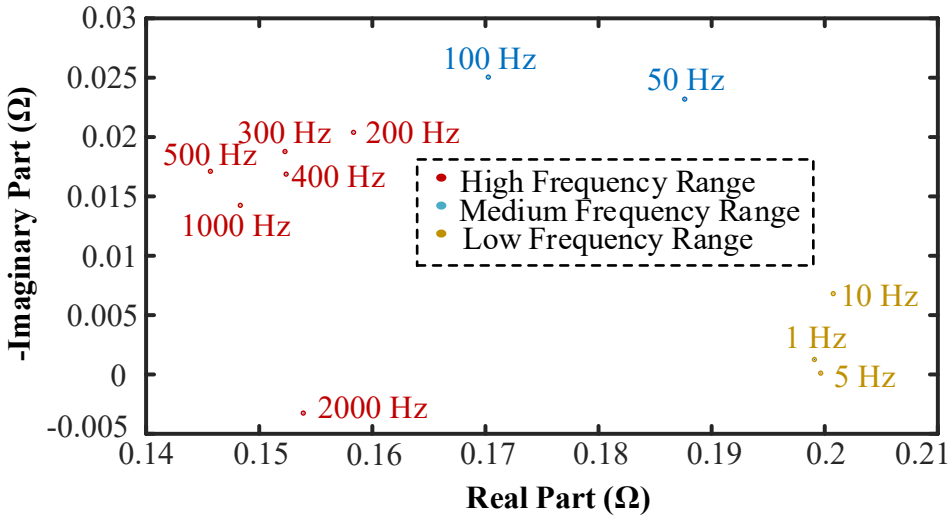

Fig. 2.14. Detected impedances from the experimental setup of impedance emulating circuit Case I.

PI controller alone while the others are obtained with the designed resonant controllers. The impedance data are divided into high-frequency, medium frequency and low-frequency ranges. Identified from the real-parts at high- and low-frequency portions and the imaginary-part from the medium-frequency ones, the measured results match well with the emulation circuit. As shown in the figure, impedance detected at 2000 Hz has a negative imaginary part. This results from unmodeled frequency-dependent inductive effects of the connection wires. Other factors such as the equivalent series resistance and inductance of the capacitor, and the noise and inaccuracies from the sensing circuits, also contribute to the error of the detected impedances. In a real implementation of the PPC-based EIS, similar measurement errors resulting from connection wires and sensing circuits also present. These factors may be taken into account in the system model and compensated for improved results.

2.3.3 Example Application in Early Fault Diagnostics

An example of using the EIS results for identification of impedance changes which correlate with health conditions of the FCS is proposed in this subsection. The impedance spectra obtained from EIS contain much richer information as compared with the terminal voltage of the FCS, as the latter only reflects the magnitude of the internal impedance at 0 Hz. Conventionally, with perturbations generated at various frequencies EIS results are used to fit an ECM. Conditions of an FCS are obtained by detecting changes on the parameters of the ECM. This process is time consuming and requires large computational resources, and thus is not suitable to be embedded directly into a converter controller. In this regard, the proposed example application aims to serve as a simple and effective solution for monitoring variations of the internal impedances of an FCS and thereby can be potentially used for identifying abnormal conditions online.

Three significant points are chosen to represent an impedance spectrum of the FCS in this application. With the resonant controllers enabling wide-range frequency perturbations, the real part of a high-frequency sample reflecting the internal resistance, the real part of a low frequency sample reflecting the polarization resistance, and the imaginary part of a medium frequency sample reflecting the double-layer capacitance, are collected with the proposed converter based EIS. The main characteristics of an impedance spectrum is thus captured with these three signatures, requiring only three EIS operations to be performed at the selected frequencies. The four emulation circuits in Table 2.1 are all tested with this procedure and the obtained results are listed in Table

Table 2.2. Testing Results of the Example Application

		Case I	Case II	Case III	Case IV
Impedance	Real at 1 Hz	0.1991	0.3916	0.2670	0.1964
	-Imaginary at 50 Hz	0.0232	0.0235	0.0554	0.0214
	Real at 1000 Hz	0.1483	0.3543	0.1482	0.1510
Health Indicator # 1	Value	0.2493	0.5286	0.3104	0.2487
	Change (%)	0	112.03	24.51	-0.24
Health Indicator # 2	Value×10^{-3}	0.5893	0.4383	3.2908	0.4858
	Change (%)	0	-25.62	458.43	-17.56
Voltage	Value	41.37	38	40.17	41.36
	Change (%)	0	-8.15	-2.90	-0.02

2.2 with 1 Hz, 50 Hz and 1000 Hz EIS frequencies. These three frequencies are selected empirically based on the results from Fig. 2.14 on the Case I circuit, where they closely reflect the characteristics of an impedance spectrum. In practical application, as the internal impedance varies in different FCSs, preliminary testing can be conducted to decide which three specific frequencies to choose for a particular case. It should be noted that the four sets of emulation circuit parameters do not constitute direct models of a specific faulty/degraded condition of a specific FCS, rather, they are used to verify the capability of the proposed method on detecting changes of the FCS internal impedance.

Impedance changes reflect the internal conditions of an FCS, and these three signatures alone can be considered as individual HIs pointing to different internal phenomena. To combine them and provide comprehensive health information of the FCS, two possible forms of HIs are proposed here. The first one is to use the Euclidean distance from the origin in the 3D space of the three signatures, whereas the second one is to use the area created by them in the complex plane. These two HIs are expressed as

$$\begin{cases} HI\#1 = \sqrt{R_{1Hz}^2 + I_{50Hz}^2 + R_{1kHz}^2} \\ HI\#2 = 0.5(R_{1Hz} - R_{1kHz})(-I_{50Hz}) \end{cases} \tag{2.14}$$

where R_{1Hz}, I_{50Hz} and R_{1kHz} are the real part at 1 Hz, the imaginary part at 50 Hz and the real part at 1000 Hz, respectively.

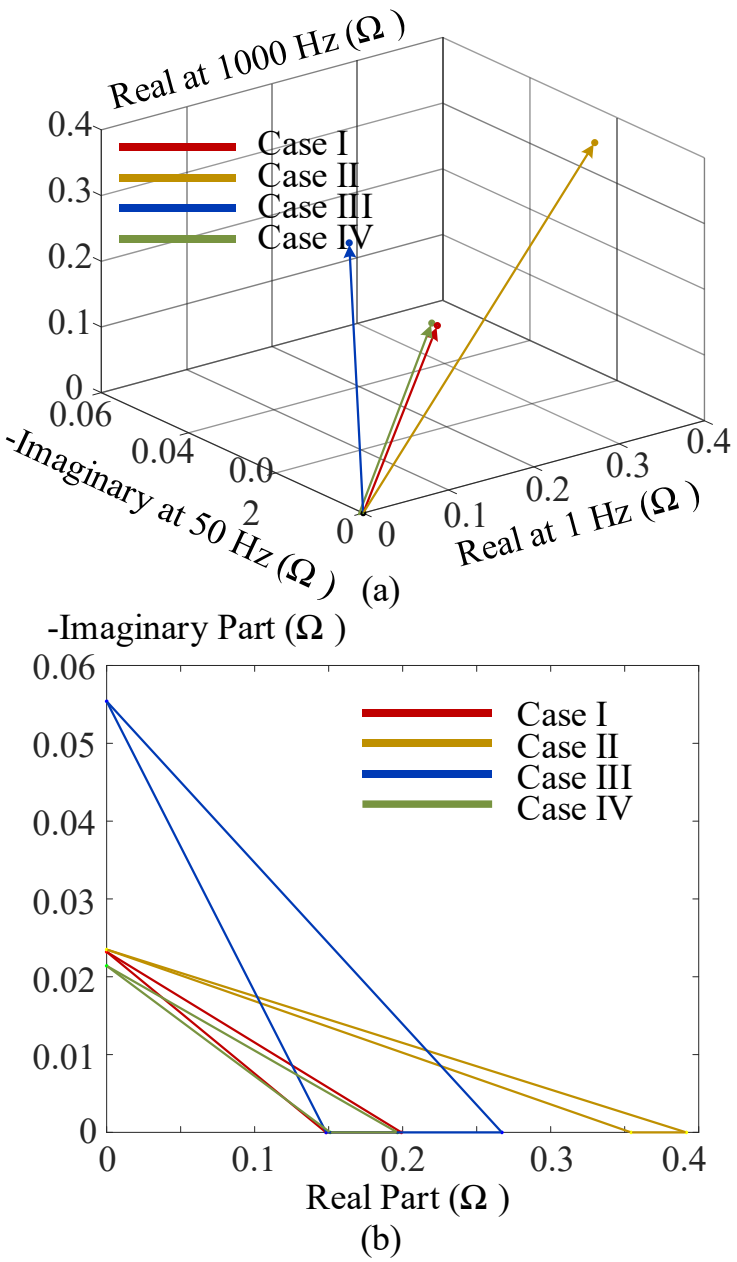

Fig. 2.15. Illustrative diagrams of (a) Health Indicator #1 and (b) Health Indicator #2.

Both indicators are illustrated in Fig. 2.15 with the obtained experimental data. The values are presented in Table II and compared with output voltage changes. The two proposed HIs provide a higher resolution on identifying impedance changes. As shown in the figure and table, HI#1 is able to separate Case I from changes on resistances, while change on C_{dl} is not clear as variations on I_{50Hz} is relatively low. HI#2 shows better performance on distinguishing all changes. On the other hand, the output voltage has resolutions below 10 % in all cases and cannot detect changes on C_{dl}.

Therefore, the proposed HIs have a good resolution to detect changes of the internal impedance. It is known from previous works [9]-[14], [35]-[37], [42]-[44] that faults/degradation cause variations on the impedance spectrum. As the formation of a fault or degradation in an FCS is a cumulative process [9], [12], the high sensitivity of the proposed HIs to the internal impedance variations allows them to detect smaller changes corresponding to the early stages of an abnormal condition. Hence, proper measures and actions can be executed earlier to prevent further damages.

This method is very efficient computationally and only needs impedances at three different frequencies, and thus can be easily embedded in the converter controller. The application shows only one possible utilization of the capability offered by the proposed PPC-based EIS. It is worth noting that the presented approach is not a direct diagnostic method for detecting any specific conditions of an FCS. However, with its demonstrated capability in providing higher resolution detection of impedance changes, advanced diagnostic and condition monitoring algorithms can be developed based on it to make the most out of an impedance spectrum covering wide frequency ranges.

2.3 Conclusions

In this chapter, the practical challenges of applying ac perturbations for EIS using a high-power FCS converter with a limited switching frequency are addressed with proposing the incorporation of resonant controllers in the current control loop. *In Situ* EIS in the high-frequency range becomes thus achievable with a high-power PPC. The effectiveness of the proposed method is verified by experimental results from a laboratory test setup. A fast impedance processing method utilizing the extended EIS results for detecting impedance changes is also presented and its simplicity and effectiveness are demonstrated as well. With only updates in the firmware of the PPC controller, a promising diagnostic function is included in the fuel cell powertrain which has the potential to save maintenance cost and guide hybrid powertrain operational strategies.

Chapter 3 Oscillation Analysis in Fuel Cell Powertrain Brought by Converter based EIS

With the required EIS ac perturbations generated by the high-power PPC of an FCS in the powertrain, the oscillation effects of adding such an extra function to a converter have not been investigated previously. Aiming at filling this gap, this chapter focuses on the oscillations brought by the converter based EIS operation and their transfer in a typical hybrid fuel cell powertrain, and thereby providing guidelines to ensure proper and safe design of the EIS mode and operation of the load.

Typical EIS operation requires a relatively small ac perturbation to keep the linearity of the operating fuel cell [62]. This criterion permits to adopt the small signal technique for analyzing the oscillations. The frequency of ac perturbations is expected to vary in a wide range to produce an informative impedance spectrum. Hence, the analysis of oscillation needs to be conducted in a wide frequency range. Moreover, the dc operating point should be fixed during the *in situ* EIS operation, and the battery is always needed for this purpose in a hybrid fuel cell powertrain. Two possible situations are considered for the *in situ* EIS, based on whether the motor is operating or not. They are discussed in detail in the following sections.

The rest of the chapter is organized as follows: Section 3.1 presents the modeling of each component in the powertrain and the small signal analysis is used to obtain the transfer functions of input ac current to output ac current of the fuel cell converter, and output impedances of battery converter and load. With the obtained models, the influences of system parameters and operating conditions on the dc link oscillations during the EIS operation are presented. Simulation results are given next for verifications. The final section concludes this chapter.

3.1 Oscillation Analysis with Small Signal Modeling

The two configurations and their small signal models of implementing converter based EIS in a hybrid fuel cell powertrain with the motor operating and idling are illustrated in Fig. 3.1,

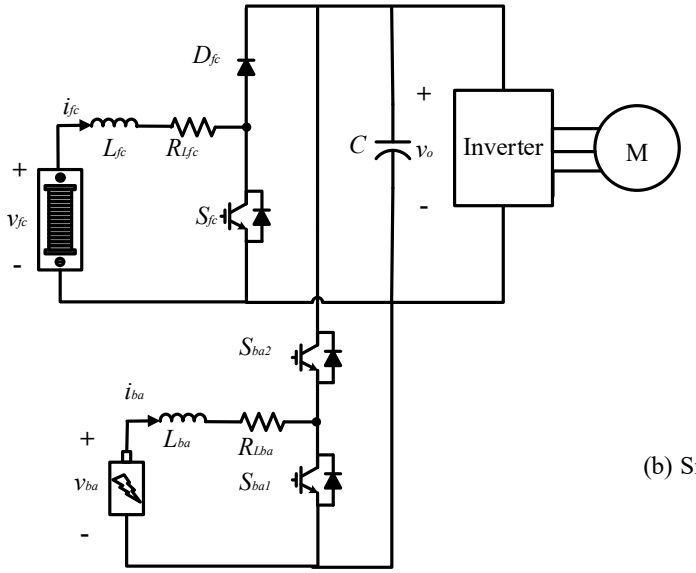

(a) Configuration 1

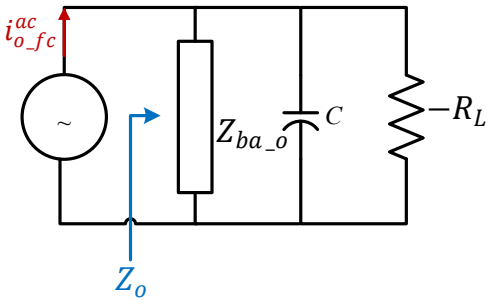

(b) Small Signal Models at dc Link of Configuration 1

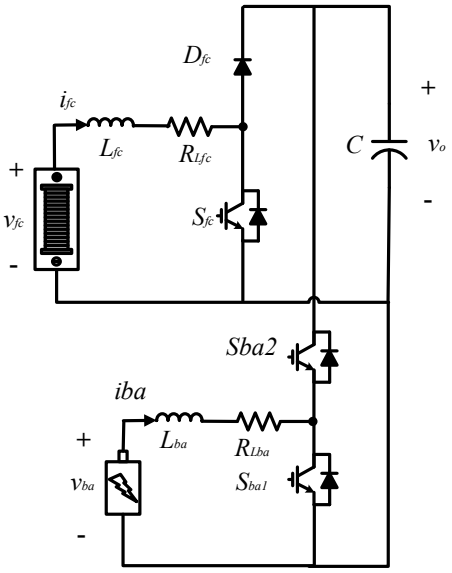

(c) Configuration 2

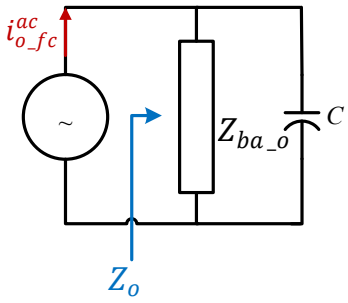

(d) Small Signal Models at dc Link of Configuration 2

Fig. 3.1. Converter based EIS implementation in a hybrid powertrain when motor is in operation and idling modes. (a) Schematic diagram of configuration 1; (b) Small signal model of configuration 1; (c) Schematic diagram of configuration 2; (d) Small signal model of configuration 2.

respectively. In the figures, v_{fc} and i_{fc} are the fuel cell output voltage and current, respectively. The output voltage and current of the battery are v_{ba} and i_{ba}. A boost converter is selected for conditioning FCS outputs while a bidirectional buck-boost is used for interfacing the battery. For high-power applications, interleaved structures are normally adopted for the converters [63].

However, since the main focus of this work is on the EIS caused oscillations that contain lower frequency components as compared with the switching ripples, single phase topology is selected here for analysis and the results are applicable for interleaved topologies as well. The inductors in the circuits are denoted as L_{fc} and L_{ba} with parasitic resistances of R_{Lfc} and R_{Lba}, respectively. The power switches and the diodes are designated as S_{fc}, D_{fc}, S_{ba1} and S_{ba2}. The output capacitor is C, and the dc link voltage is v_o. For configuration 1, the load is a propulsion motor drive in a vehicle powertrain, while for configuration 2, the load is eliminated as the motor is assumed to be idling.

Small signal modeling is widely used in the control system design and power electronics [58]. The outcome is a linear transfer function around a steady-state operating point, which reveals the relation between two dynamic variables. This technique is applied here to find out the linkage between perturbations from EIS and the oscillations appearing on the dc link under various operating conditions, as the ac perturbations are relatively small in magnitude in comparison with the dc components and thus satisfy the requirement of a "small signal".

As shown in the small signal models in Fig. 3.1, converter based EIS operation introduces oscillations and they are transferred from the fuel cell port to the dc link and received by the components connected to it, which collectively form a total impedance of Z_o. In the following sections, the dc components of all variables are denoted with a superscript of *dc* and ac components induced by the EIS operation are denoted with a superscript of *ac*.

3.1.2 Components Modeling in the Powertrain

As an electrochemical device, an FCS features a soft output curve due to its internal impedance. The internal impedance is affected by the different conditions of an FCS and it is why impedances detected by EIS can be used for diagnosis, e.g., flooding conditions tend to increase the high-frequency resistance [9], [42]- [44].

At steady-state dc operation, the internal impedance equals its polarization resistance, and the fuel cell can be approximated as a first-order model, as shown in Fig. 3.2. It is expressed as

$$V_{fc}^{dc} = V_{oc} - R_{fc} I_{fc}^{dc} \tag{3.1}$$

where V_{oc} and R_{fc} are the open-circuit voltage and internal polarization resistance, respectively. They can be obtained from the maximal and minimal voltages and currents provided in the datasheet of a fuel cell or through testing. It should be noted here that this first-order linearized model is only valid for analyzing the dc components of fuel cell outputs.

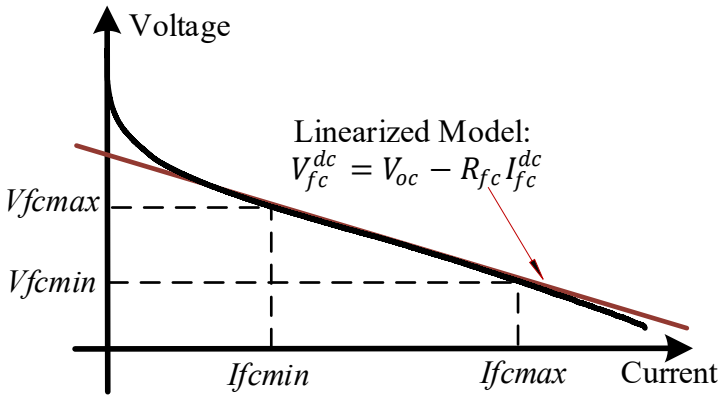

Fig. 3.2. V-I curve of an FCS output and its linearized model in the linear region.

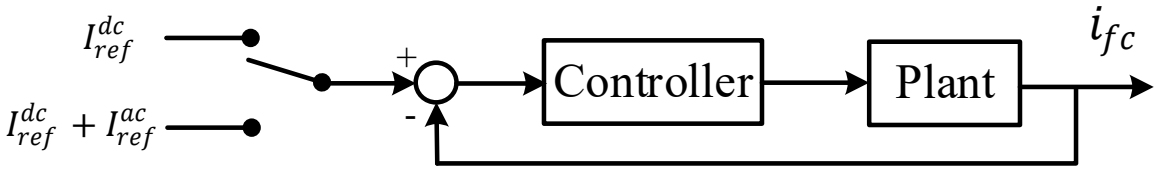

Fig. 3.3. Current control loop of fuel cell converter.

With the linear model in (3.1), the fuel cell output current and voltage are obtained for its given power demand of P_{fc}

$$\begin{cases} I_{fc}^{dc} = \dfrac{V_{oc} + \sqrt{V_{oc}^2 - 4R_{fc}P_{fc}}}{2R_{fc}} \\ V_{fc}^{dc} = \dfrac{V_{oc} - \sqrt{V_{oc}^2 - 4R_{fc}P_{fc}}}{2} \end{cases} \tag{3.2}$$

A fuel cell converter is operated in the current control mode and a sinusoidal reference is added to the current reference at the starting of an EIS procedure, as shown in Fig. 3.3. Assuming the reference is followed well with the closed loop current control and neglecting the switching ripples, during EIS, the fuel cell output current comprises of both dc and ac components and is written as

$$i_{fc} = I_{fc}^{dc} + i_{fc}^{ac} = I_{fc}^{dc} + 0.1 I_{fc}^{dc} \sin(\omega t) \tag{3.3}$$

in which the magnitude of the ac perturbation typically takes 10% of the dc current magnitude.

The output current from the FCS to the dc link is the current at the diode of the boost converter, written as

$$i_{o\_fc} = d_{fc} i_{fc} \tag{3.4}$$

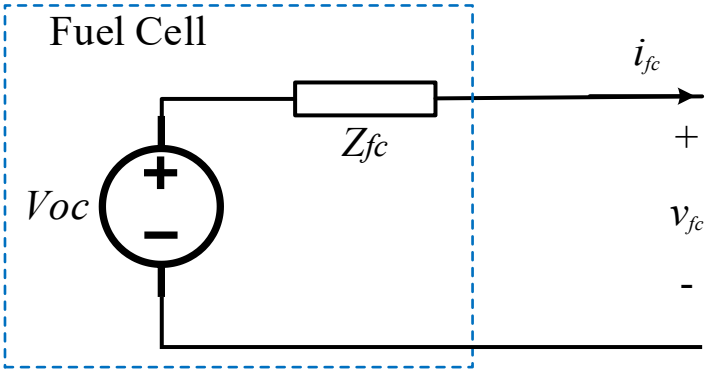

Fig. 3.4. Fuel cell model with the open-circuit voltage and internal impedance.

Considering the ac perturbation as a small signal added upon the dc component, equation (3.4) is rewritten as

$$i_{o\_fc}^{dc} + i_{o\_fc}^{ac} = \left(1 - D_{fc}^{dc} - d_{fc}^{ac}\right)\left(I_{fc}^{dc} + i_{fc}^{ac}\right) \tag{3.5}$$

where D_{fc}^{dc} and d_{fc}^{ac} are the dc and ac components of the duty cycle of the boost converter, respectively. By eliminating the second-order component and extracting the ac output current, the following expression is obtained as

$$i_{o\_fc}^{ac} = \left(1 - D_{fc}^{dc}\right)i_{fc}^{ac} - I_{fc}^{dc} d_{fc}^{ac} \tag{3.6}$$

The dynamic model of the FCS current is

$$L_{fc}\frac{di_{fc}}{dt} + r_{Lfc} i_{fc} = v_{fc} - (1 - d_{fc}) v_o \tag{3.7}$$

Applying ac perturbations to the variables in (3.7) and transforming to Laplace domain, the ac components are extracted as

$$\left(L_{fc}s + r_{Lfc}\right)i_{fc}^{ac} = v_{fc}^{ac} + V_o^{dc} d_{fc}^{ac} - (1 - D_{fc}^{dc}) v_o^{ac} \tag{3.8}$$

where the second order component is eliminated from (3.8). v_{fc}^{ac} is the ac component of the fuel cell output voltage induced by i_{fc}^{ac}, expressed as

$$v_{fc}^{ac} = -Z_{fc} i_{fc}^{ac} \tag{3.9}$$

in which Z_{fc} is the complex internal impedance of an FCS to be detected with EIS, as shown in Fig. 3.4.

Substituting (3.6) and (3.8) into (3.4), by a few steps of manipulation, it is expressed in the Laplace domain as

$$i_{o\_fc}^{ac}(s) = \frac{V_{fc}^{dc} i_{fc}^{ac} + I_{fc}^{dc} v_{fc}^{ac}}{V_o^{dc}} - \frac{\left(L_{fc}s + r_{Lfc}\right) I_{fc}^{dc}}{V_o^{dc}} i_{fc}^{ac} - \frac{P_{fc}}{V_o^{dc2}} v_o^{ac} \tag{3.10}$$

From (3.10) it can be seen, the oscillation brought to the dc link of the powertrain is affected by the parameters of the fuel cell and its converter. Moreover, the dc operating point also plays a role here.

The ac ripple currents injected to the dc link is given in (3.10), which is shared by the battery, capacitor of dc link and the motor load in the case of the configuration 1 in Fig. 3.1 (a). On the other hand, the oscillations are received by the dc link capacitor and battery only in configuration 2, which is basically charging the battery from FCS. The capability of the load side components absorbing and buffering the ripples generated by EIS operation is determined by its output impedance.

As an electrochemical energy source, the battery also has its own internal impedance [45]. However, it is relatively small, also because the focus of this chapter is on the FCS, the internal impedance of the battery is neglected from here.

For simplicity while not losing generality, single voltage loop control is used to control the battery in this chapter. The battery control loop is shown in Fig. 3.5 (a) and its equivalent transformation is given in Fig. 3.5 (b) to reveal the output impedance of the converter. By combining the block diagrams in Fig. 3.5 (b), the output small signal impedance is obtained as

$$Z_{ba_o}(s) = \frac{1}{\left(V_{ba}^2/V_o^{dc^2} - G_v V_{ba}\right)/(L_{ba}s + r_{Lba}) + I_{ba}^{dc} G_v} \tag{3.11}$$

From (3.11), apart from the converter parameters and operating conditions, the voltage controller G_v is an important factor in determining Z_{ba_o}.

For reference, when dual-loop control is adopted, the control block diagram is transferred to the one as shown in Fig. 3.5 (c) and (d), and the output small signal impedance is

$$Z_{ba\_o}(s) = \frac{1}{\left[-\left(V_{ba}^2/V_o^{dc^2} + G_i G_v V_{ba}\right)/(L_{ba}s + r_{Lba} + V_o^{dc} G_i) + I_{ba}^{dc} G_v - I_{ba}^{dc} G_i (V_{ba}^{dc}/V_o^{dc} + G_i G_v V_o)/(L_{ba}s + r_{Lba} + V_o^{dc} G_i)\right]} \tag{3.12}$$

In a running vehicle, the load in the powertrain is a motor drive, while for an idling car the load is eliminated. A tightly regulated motor drive is considered as a constant power load (CPL) [64], [65]. The relation between the load current and voltage is given as

$$i_{o\_L} = \frac{P_L}{v_o} \tag{3.13}$$

The small signal model of (3.13) is obtained by taking derivatives on both sides as

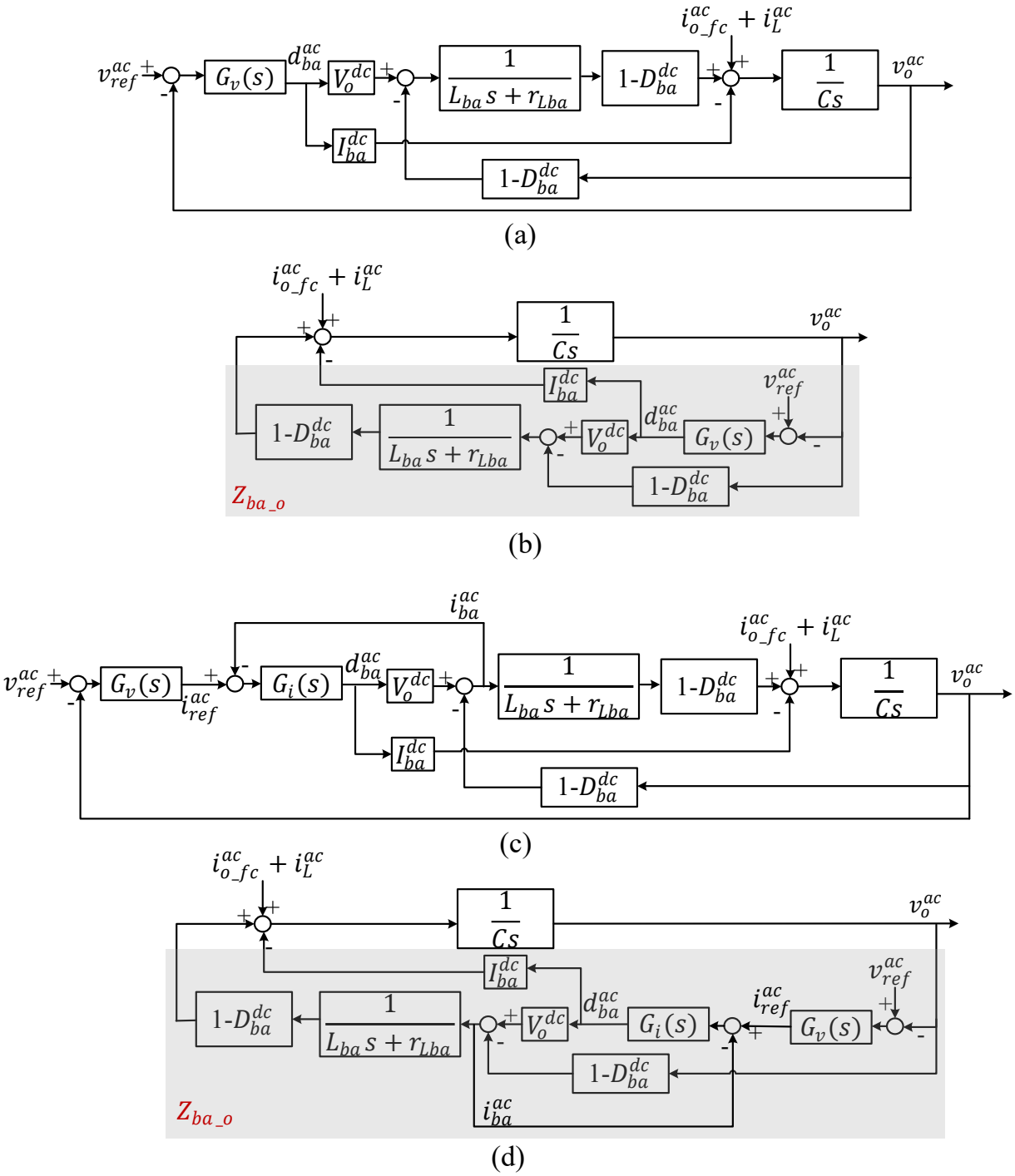

Fig. 3.5. Block diagram of single and dual loop voltage control of the battery converter. (a) original diagram of single loop control; (b) diagram transformation of single loop control to find out Z_{ba_o}; (a) original diagram of dual loop control; (b) diagram transformation of dual loop control to find out Z_{ba_o}.

$$\frac{i_{o\_L}^{ac}}{v_o^{ac}} = -\frac{P_L}{V_o^{dc^2}} = -\frac{1}{R_L} \tag{3.14}$$

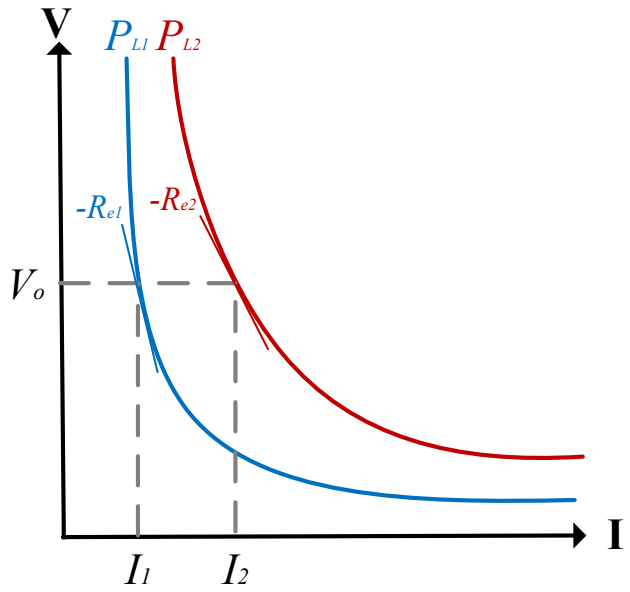

Fig. 3.6. Equivalent resistance of CPL under different load power.

where the load appears as a negative resistance in the small signal model. P_L is the load power and R_L is the equivalent resistance. The value of R_L depends on P_L, as shown in Fig. 3.6.

Considering the capacitor of the dc link, the total small signal impedance at the load side is

$$Z_L(s) = \frac{1}{sC - 1/R_L} \tag{3.15}$$

As shown in (3.15), the CPL provides a negative damping and tends to increase the magnitude of oscillation on the dc link. On the other hand, when the motor is idling, the load side small signal impedance is

$$Z_L(s) = \frac{1}{sC} \tag{3.16}$$

In practice, the motor load is a non-ideal CPL. Its bandwidth is affected by the current control loops of the motor drive. However, in the scope of this chapter, the frequencies of oscillations from EIS are of interest, where the highest frequency is limited by the bandwidth of the dc/dc converter. This frequency should lie within the bandwidth of the current controllers of a well-designed drive for vehicles. Moreover, modeling the load as an ideal CPL gives the worst-case condition. Hence, the load can be viewed as an ideal CPL during the EIS operation.

With the negative impedance of CPL, the bandwidth of the battery voltage loop is greatly limited. Many efforts were made to resolve the effect of CPL with advanced controllers [66], [67]. In this chapter, however, the main aim is to present a general analysis of oscillations brought by

the converter based EIS instead of resolving stability issues caused by CPLs; also, linear PI controllers are still widely adopted in practice. Therefore, the conventional linear controller is used here for the analysis.

3.1.3 Oscillation analysis on the dc Link

With the models obtained in Section 3.1.2, the transfer function between i_{fc}^{ac} and V_o^{ac} is derived for the two configurations. For configuration 1, the transfer function is expressed as

$$T_{vo\_ifc}(s) = \frac{v_o^{ac}}{i_{fc}^{ac}} = \frac{Z_o\left[\left(V_{fc}^{dc} - Z_{fc}I_{fc}^{dc}\right) - I_{fc}^{dc}\left(L_{fc}s + r_{Lfc}\right)\right]}{V_o^{dc}\left(1 + Z_o P_{fc}/V_o^{dc^2}\right)} \tag{3.17}$$

in which Z_o is

$$Z_o(s) = \frac{1}{sC - P_L/V_o^{dc^2} - \left(V_{ba}^2/V_o^{dc^2} - G_v V_{ba}\right)/\left(L_{ba}s + r_{Lba}\right) + I_{ba}^{dc}G_v} \tag{3.18}$$

In the case of configuration 2, Z_o is replaced with

$$Z_o(s) = \frac{1}{sC - \left(V_{ba}^2/V_o^{dc^2} - G_v V_{ba}\right)/\left(L_{ba}s + r_{Lba}\right) + I_{ba}^{dc}G_v} \tag{3.19}$$

In this section, influences of system parameters and operating conditions on the oscillation of dc link during EIS are assessed. The parameters of a base case are given in the study case of Section 3.2.1, which will be adopted here for illustration.

In (3.17), the contributions of parameters related to the FCS and its converter are defined as

$$C_{fc}(s) = \left(V_{fc}^{dc} - Z_{fc}I_{fc}^{dc}\right) - I_{fc}^{dc}\left(L_{fc}s + r_{Lfc}\right) \tag{3.20}$$

Separating Z_{fc} into real and imaginary parts, RE_{fc} and IM_{fc}, the absolute value of C_{fc} is written as

$$\left|C_{fc}\right|^2 = \left[V_{fc}^{dc} - \left(r_{Lfc} + RE_{fc}\right)I_{fc}^{dc}\right]^2 + \left(L_{fc}\omega + IM_{fc}\right)^2 I_{fc}^{dc^2} \tag{3.21}$$

Z_{fc} is unknown here, as it is to be detected with EIS. For the impedances of a typical FCS, IM_{fc} is normally of negative values within the frequency range of interest of an FCS, i.e., 1-1000 Hz. From (3.17), it is shown the worst-case condition of oscillations on the dc link happens when C_{fc} is the highest. The upper limit of $|C_{fc}|$ can be found with the lowest RE_{fc} and highest IM_{fc}. Therefore, in order to find the worst condition, Z_{fc} can be replaced with polarization resistance R_{fc} of a healthy stack at the beginning of the FCS life, where IM_{fc} is zero and RE_{fc} is the lowest, as faults and degradation tend to increase the value of RE_{fc} [9]-[14], [35]-[37], [42]-[44]. The worst-case condition is expected to be found here to provide guidelines for future designs.

Fig. 3.7 shows the variation of $|C_{fc}|$ under different frequencies with different value of inductor

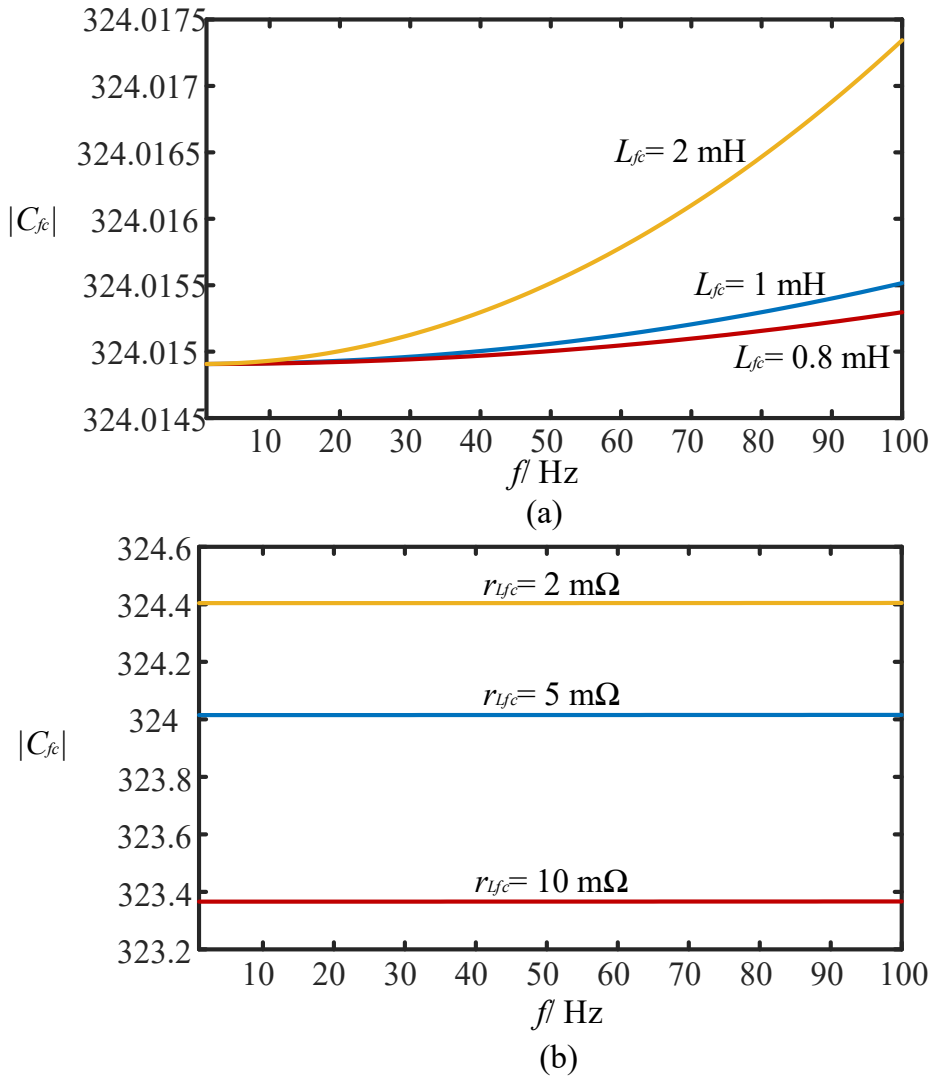

Fig. 3.7. Effects of L_{fc} and r_{Lfc} on $|C_{fc}|$.

and its parasitic resistance. The frequency range chosen here for illustration is 0-100 Hz, as the higher frequency EIS oscillations are diminished well by the dc link capacitor. Higher L_{fc} increases $|C_{fc}|$ at high frequencies and the influence on the low frequencies is relatively small. The change on r_{Lfc} introduces variations on all frequencies for $|C_{fc}|$ equally, and a higher value of r_{Lfc} tends to increase the value of $|C_{fc}|$. From (3.21), the effects of r_{Lfc} and RE_{fc} on $|C_{fc}|$ are the same. It indicates that a used FCS and its converter inductor, which is with the higher internal fuel cell resistance and inductor parasitic resistance, tends to introduce lower oscillation magnitudes.

The influence of dc link capacitor C is illustrated in Fig. 3.8 along with Z_{ba_o} of the base case for comparison. The variation of C has a great impact on the total output impedance. The magnitude of oscillations from EIS can be reduced greatly at the expense of higher capacitances.

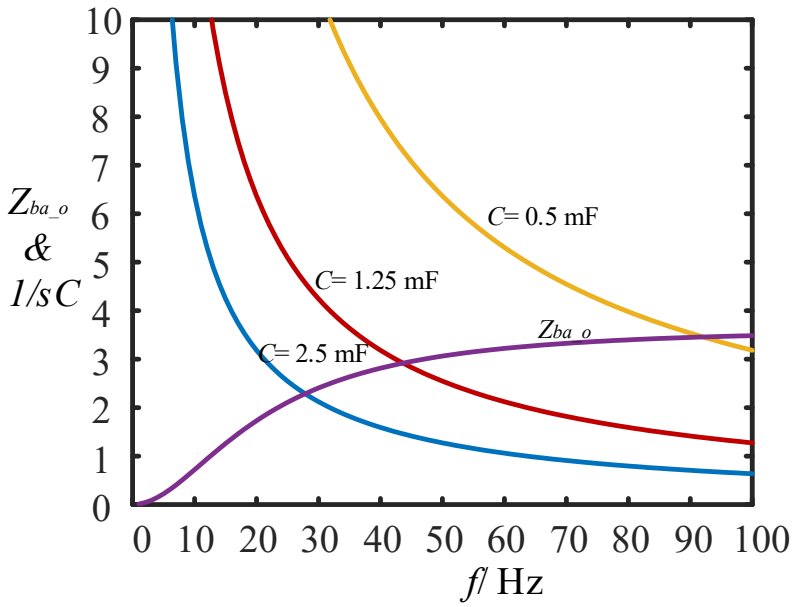

Fig. 3.8. Impedance of load capacitor with different capacitor values.

The parameters of the battery converter are included in Z_{ba_o} as shown in (3.11), which together with the load and load capacitor, define the total impedance Z_o. As shown in (3.18), a resonance is generated by L_{ba} and C. The resonant frequency is

$$f_r = \frac{V_{ba}/V_o}{2\pi\sqrt{L_{ba}C}} \tag{3.22}$$

As shown in Fig. 3.9 (a) for configuration 1 and Fig. 3.9 (b) for configuration 2 of the total output impedance Z_o, a L_{ba} of 0.2 mH and a C of 2500 uF give a resonant frequency around 85 Hz. Due to the resonance, there is a peak in the value of Z_o at the resonant frequency, leading to a high rejection of oscillations to the battery. Hence, it will cause high-magnitude oscillations on the dc link when EIS is triggered at or close to this frequency.

Defining a power splitting parameter η, the output powers from the fuel cell and battery are

$$\begin{cases} P_{fc} = \eta P_L \\ P_{ba} = (1-\eta)P_L \end{cases} \tag{3.23}$$

Given the power demands for the FCS, the output current and voltage of the FCS are obtained by (3.2). Different load powers and splitting parameters for Z_o are presented in Fig. 3.9. Both P_L and η have effects on Z_o for configuration 1, while not affecting configuration 2 since they were not included in (3.19). From Fig. 3.9, a higher P_L leads to a higher impedance Z_o, indicating less portion of oscillations will be absorbed by the battery. However, a higher total power output demands more power from the fuel cell for the same power splitting parameter, which gives a

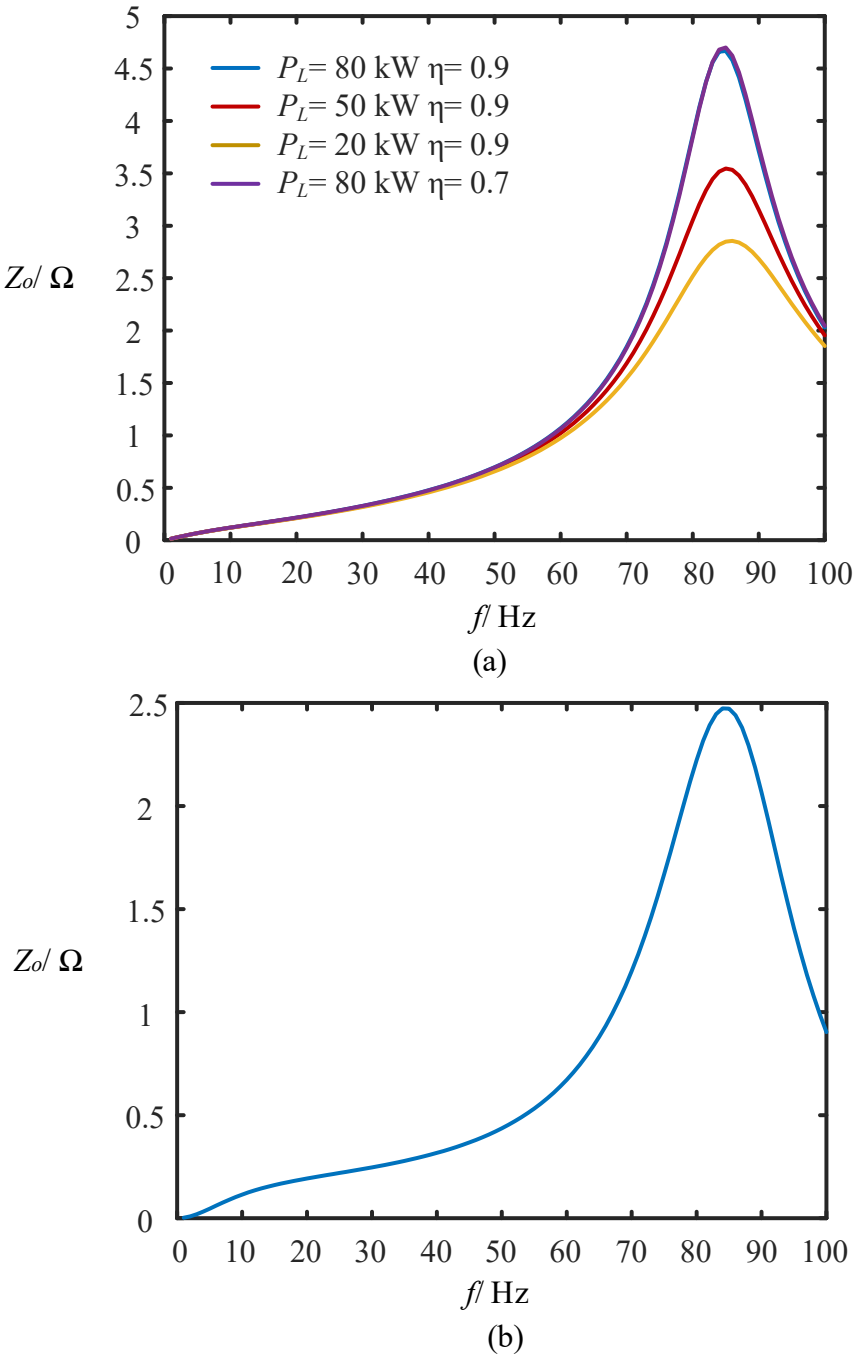

Fig. 3.9. Effects of P_L and η on total impedance Z_o of motor running and idling.

higher magnitude of i_{fc}^{ac} and reduces T_{vo_ifc} as P_{fc} is in the denominator of (3.17). Given the same P_L, different η shows a similar load impedance, while a lower η presents a smaller i_{fc}^{ac} and higher T_{vo_ifc}. Therefore, multiple factors play a role here in determining the final magnitude of oscillation at the dc link.

On the other hand, Z_o is the same for configuration 2 regardless of P_{fc} and it is generally smaller

than configuration 1 since CPL is eliminated. The final dc link oscillation is therefore determined by the fuel cell output power, which affects both i_{fc}^{ac} and T_{vo_ifc} differently.

3.2 Simulation

3.2.1 Description of Study Case

The studied case in this chapter emulates a hybrid powertrain with an FCS and a battery bank. Parameters of the Toyota Mira and the characteristics of Ballard HD100 heavy-duty fuel cell module are used. The parameters are listed below:

Maximal load power P_{Lmax}= 114 kW; dc link voltage V_o= 650 V; fuel cell open-circuit voltage V_{oc}= 585.907 V; fuel cell internal polarization resistance R_{fc}= 0.8907 Ω; battery voltage V_{ba}= 245 V.

The parameters of converters are listed below:

L_{fc}= 1 mH; r_{Lfc}= 5 mΩ; L_{ba}= 0.2 mH; r_{Lba}= 20 m Ω; C= 2500 uF.

The controller parameters of the fuel cell current loop and battery voltage loop are given below, which set bandwidths to 1 kHz and 10 Hz respectively.

K_{pfc}= 0.0083714; K_{ifc}= 30.3714; K_{pba}= 0; K_{iba}= 0.035935.

3.2.2 Results

Simulations are conducted in Matlab/Simulink and the results are presented in this section with the parameters given in above as the base case. The results of I_{fc} and V_o are shown in Figs. 3.10-3.17 under various conditions for configurations 1 and 2, respectively, as labeled in red texts top of each sub-figure. The EIS is triggered at 0.1 s. From 0 to 0.1 s, the initial ripple is caused by the limited bandwidth of the voltage control loop. The selection of simulation timeline as 0.7 seconds is in consideration of the EIS frequency excited and clearness of the demonstrations.

Overall, the EIS conducted under motor idling condition introduces much smaller oscillations since no negative damping is presented in the powertrain. Moreover, higher oscillations can be allowed in configuration 2 as long as the EIS operation is maintained, as no motor operation is involved in this condition. Therefore, it is more favorable to carry out *in situ* EIS when the motor is not in operation.

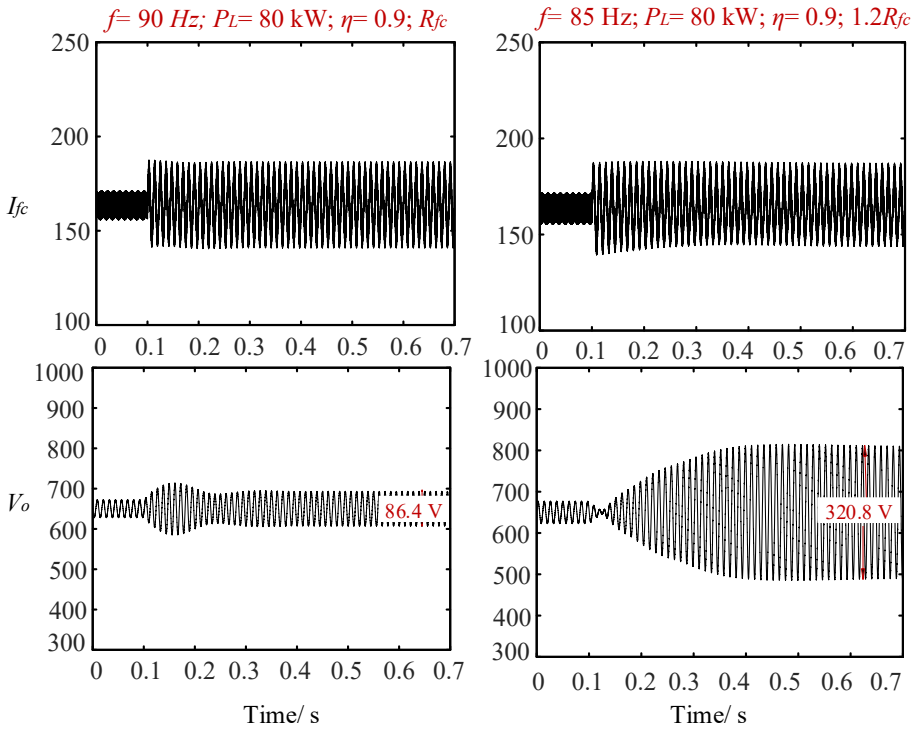

Fig. 3.10. Simulation results of configuration 1.
(a) $f = 90$Hz, $P_L = 80$ kW, $\eta = 0.9$, R_{fc}; and (b) $f = 90$ Hz, $P_L = 80$kW, $\eta = 0.9$, $1.2R_{fc}$.

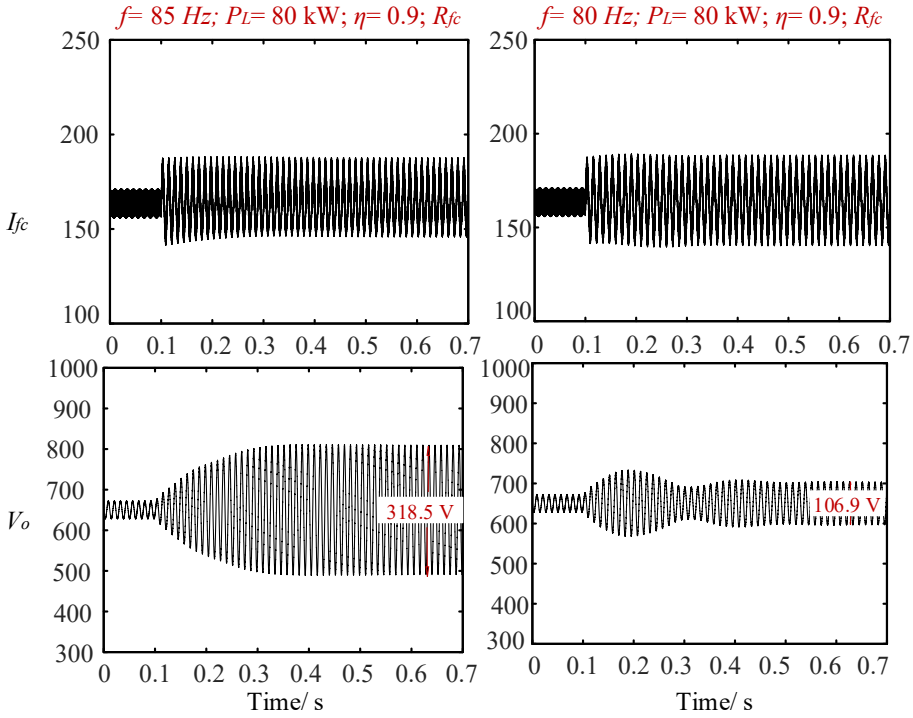

Fig. 3.11. Simulation results of configuration 1.
(a) $f = 85$ Hz, $P_L = 80$ kW, $\eta = 0.9$, R_{fc}; and (b) $f = 80$ Hz, $P_L = 80$ kW, $\eta = 0.9$, R_{fc}.

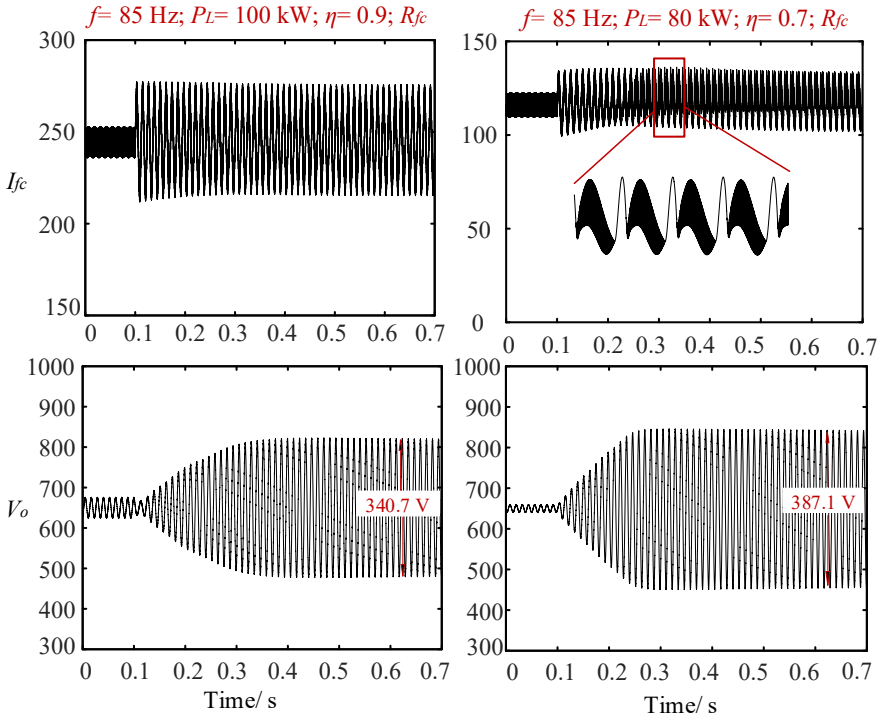

Fig. 3.12. Simulation results of configuration 1.
(a) f = 85 Hz, P_L = 100 kW, η = 0.9, R_{fc}; and (b) f = 85 Hz, P_L = 80 kW, η = 0.7, R_{fc}.

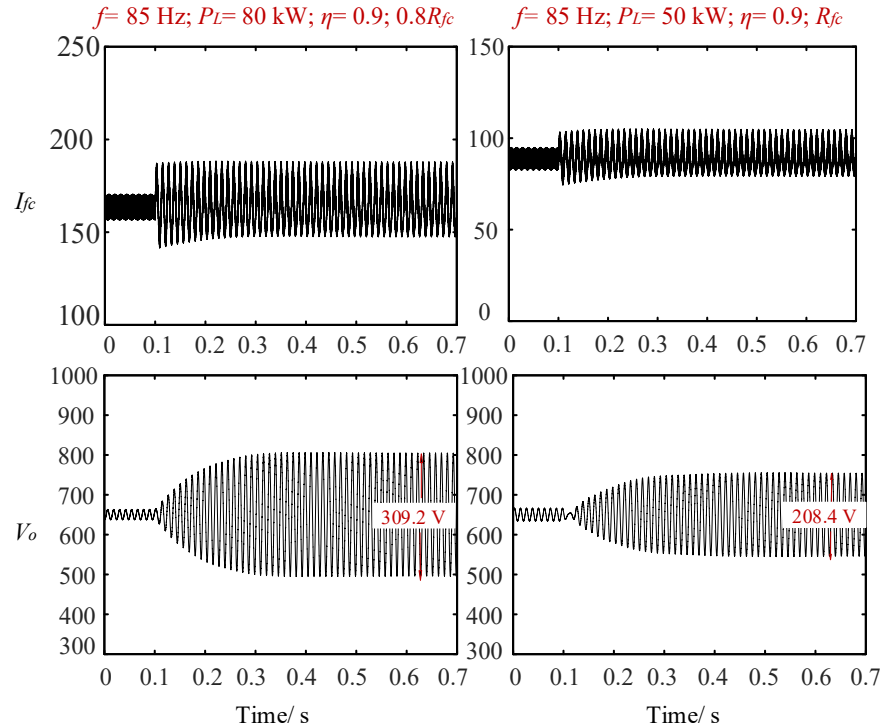

Fig. 3.13. Simulation results of configuration 1.
(a) f = 85 Hz, P_L = 80 kW, η = 0.9, 0.8R_{fc}; and (b) f = 85 Hz, P_L = 50 kW, η = 0.9, R_{fc}.

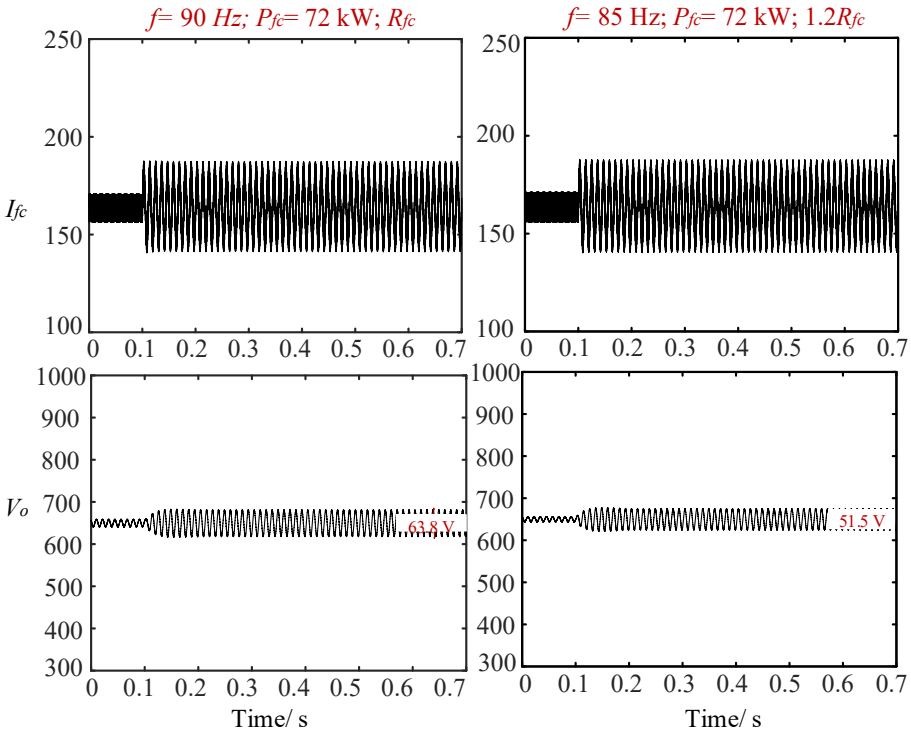

Fig. 3.14. Simulation results of configuration 2.
(a) f = 90 Hz, P_L = 72 kW, R_{fc}; and (b) f = 85 Hz, P_L = 72 kW, 1.2R_{fc}.

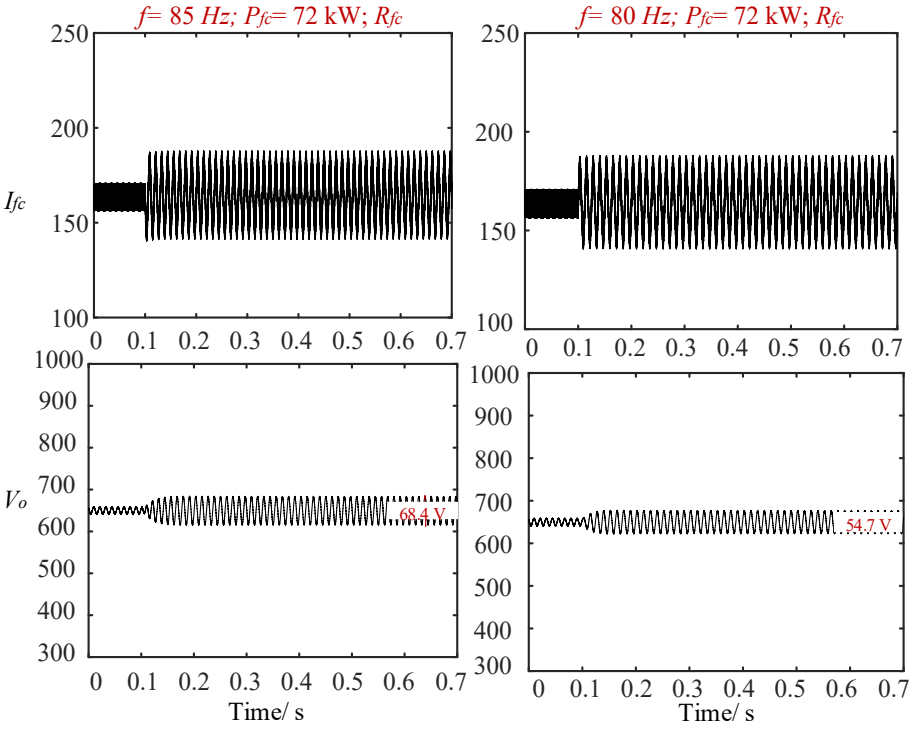

Fig. 3.15. Simulation results of configuration 2.
(a) f = 85 Hz, P_L = 72 kW, R_{fc}; and (b) f = 80 Hz, P_L = 72 kW, 1.2R_{fc}.

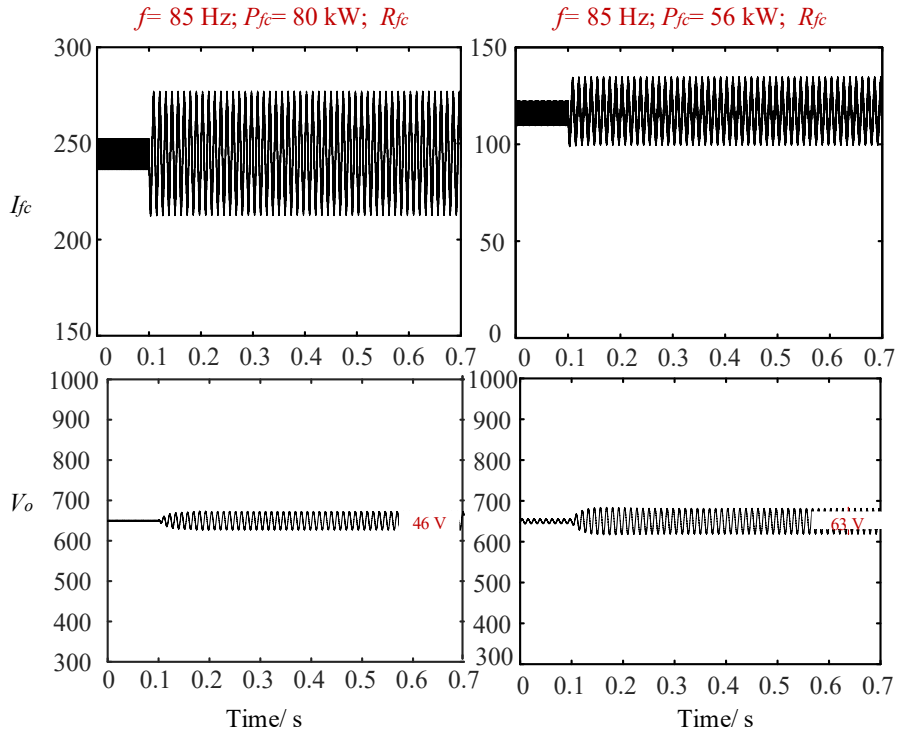

Fig. 3.16. Simulation results of configuration 2.
(a) f = 85 Hz, P_L = 80 kW, R_{fc}; and (b) f = 85 Hz, P_L = 56 kW, R_{fc}.

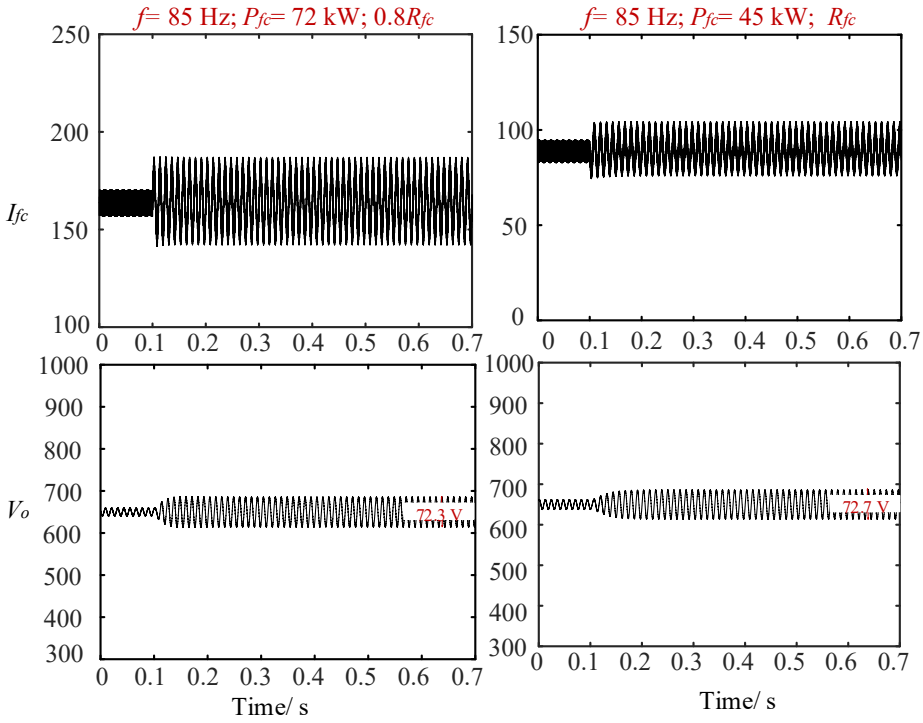

Fig. 3.17. Simulation results of configuration 2.
(a) f = 85 Hz, P_L = 72 kW, 0.8R_{fc}; and (b) f = 85 Hz, P_L = 45 kW, R_{fc}.

From the previous analysis, the maximal oscillation happens at the resonant frequency of the battery converter. Hence, the EIS is applied at 85 Hz through the current control loop of fuel cell and EIS is also triggered at 80 Hz and 90 Hz for comparisons as well in both configurations. As shown in the figures, the oscillations at the dc link have highest magnitudes when EIS is excited at 85 Hz, reaching 318.5 V in configuration 1 and 68.4 V in configuration 2 and oscillations are lower in both configurations of EIS being triggered at 80 Hz and 90 Hz under the same conditions.

To illustrate the effect of internal resistance of the fuel cell, three simulation results are given by increasing and decreasing the internal impedance of the base case and compared (in plots (b), (c) and (g) of condition 1 in Fig. 3.10, 3.11 and 3.13), where the base case original R_{fc} is multiplied by 1.2 and 0.8. As predicted from previous analysis, the increase of internal resistance reduces the oscillation on the dc link and the oscillation magnitude becomes larger when R_{fc} is lower. Since R_{fc} normally increases for a used FCS, shown as a decrease in efficiency, the oscillation will not get worse with more servicing cycles. Therefore, the powertrain can be designed according to the parameters of a healthy stack at the beginning of its usage only, which already corresponds to the worst case of oscillations on the dc link during the EIS mode.

The results of increasing to 100 kW and decreasing to 50 kW from 80 kW of the load power are illustrated for configuration 1 (in (c), (e) and (h) for configuration 1 in Fig. 3.11- 3.13), while η is kept the same at 0.9. It is shown that higher load power leads to higher oscillations on the dc link. The result when η equals 0.7 is also given. In this case, as shown in (f) in Fig. 3.12, the magnitude of the transfer function of T_{vo_ifc} increases and is the dominating factor, while the output power from the fuel cell is reduced, leading to a lower magnitude of ac perturbation. The oscillation showing on the dc link is presented and the magnitude is 387.1 V. The dc link voltage swings to a level that is lower than the fuel cell output voltage in this case. Therefore, the modulated current is not in the shape of a sinusoidal waveform in the expanded waveform.

Generally, the oscillation is much reduced when the motor is idling of configuration 2. Changes on P_L and η in configuration 1 refers to the variations of P_{fc} of configuration 2, which are shown in corresponding positions in Fig. 3.14- 3.17 with the same fuel cell operating point. It is shown that the magnitude of oscillation is not proportionally changing with P_{fc}, as the magnitude of i_{fc}^{ac} and T_{vo_ifc} are directly and inversely proportional to P_{fc} respectively. It is found that the change of oscillation with P_{fc} is relatively small in this configuration.

3.3 Summary and Conclusions

Converter based EIS enables the possibility of performing *in situ* characterization and diagnostics of an FCS. However, its effects in the powertrain of a hybrid FCV, mainly the oscillations triggered from the EIS ac perturbations, are largely overlooked in the literature, not to say, a systematic analysis. This chapter fills this gap by adopting the small signal approach to analyze oscillations on the common dc link in a hybrid fuel cell powertrain. Detailed modeling of the powertrain and system analysis are presented, along with simulation cases to find out the worst-case condition.

The main intended contributions and conclusions of this chapter are summarized below:

1. For the first time, the oscillations brought by converter based *in situ* EIS to a powertrain are recognized and systematically analyzed.

2. The analyzing results of EIS with hybrid powertrains reveal that the resonance related the energy storage converter increases the oscillation on dc link to its maximum. The resonant frequency is related to the converter parameters and operating conditions as shown in (3.22). It is suggested that advanced control methods can be used to shape the output impedance of the energy storage converter to eliminate this effect. Otherwise, the resonant frequency should be avoided for EIS operations.

3. In general, the oscillations are larger when the EIS is performed during the motor is running. In consideration of protecting the motor, the requirement of oscillation is stricter in this case. Therefore, operating EIS with an idling motor is preferred. If EIS must be performed with the motor in operation, the EIS frequencies should be chosen to have enough separation from the powertrain resonant frequency, and operating conditions should be considered to minimize the dc link oscillations.

4. The magnitude of oscillation at the resonant frequency is also affected by the internal resistance of a fuel cell, total load power and power split parameter. It is critical to find a suitable operating point to perform EIS close to the resonant frequency.

5. As revealed in this chapter, increasing of internal resistance tends to mitigate the oscillation on dc link. The worst-case condition can be found through testing on a healthy stack, as the magnitude of oscillation reduces with the usage of an FCS.

Chapter 4 Fuel Cell Oriented Design of an CF Isolated Converter with a Wide-Frequency-Range EIS

As presented in previous chapters, the need for a wide-frequency-range EIS poses great constraints on the converter design. The limitations of achieving frequencies at high and low ends are revealed, where the high end is constrained by converter control bandwidth and the lower ones causes significant ripples on the output. A type of converter is adopted to address these issues to this end here. It is designed considering the output characteristics of an FCS to optimal. Therefore, given the high efficiency, high-frequency perturbations are excited with the extended switching frequency. On the other hand, the oscillations, especially low-frequency ones, occurred from EIS operation are tackled by guiding the oscillations from the load side to the PSES in the proposed converter topology. In the end, a fuel-cell-dedicated PPC capable of presenting a wide frequency range of perturbations is achieved. A design case is presented, and its experimental results reveal the effectiveness of the proposed approach in this chapter.

The rest of this chapter is organized as follows: The proposed type of converter and its operating principles are presented in Section 4.1. The designing process of the converter considering the output characteristics of an FCS during the normal operation and the capacitor sizing of PSES during the EIS operation are also given in this section. An example converter is designed with the proposed methods. Experimental results are presented in Section 4.2. Finally, conclusions are given in Section 4.3.

4.1 Proposed Type of Converter

The topologies of current fed dual active bridge (CF-DAB) and its derivations are selected in this chapter, which renders two degrees of control freedoms, phase shift and duty cycle, and a PSES. Isolated converters have higher conversion ratios, fitting well with the low-voltage high-current output characteristic of an FCS. Moreover, galvanic isolation is provided, and soft switching is achievable. The interleaved CF input reduces the switching ripples at the output port

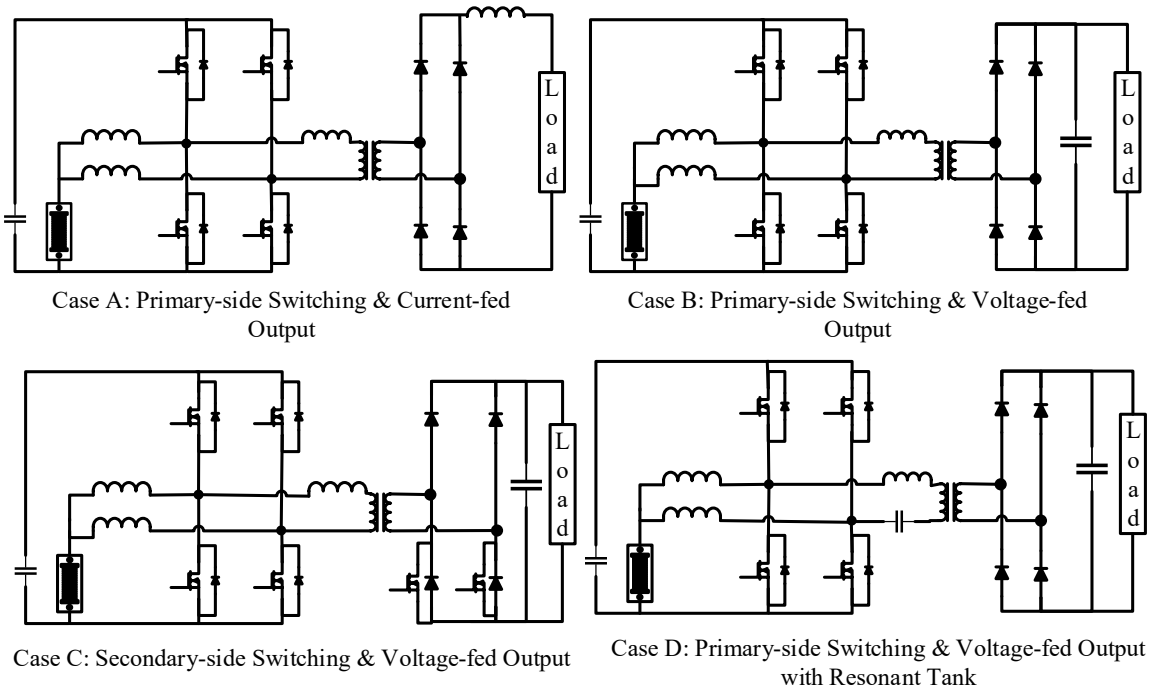

Fig. 4.1. Examples of proposed types of isolated converters.

of an FCS, which helps to extend its lifetime. PSES, which was originally used for clamping the primary side voltage, is adopted here in EIS mode for absorbing oscillations as well. By appropriate controls, the output power and the EIS operation are separately managed by the two control parameters. The oscillations brought by EIS, especially the low-frequency ones, are led to PSES, leaving no disturbance on the dc link.

Various forms of CF isolated converters were proposed previously [68]-[73] and can be adopted for this application. A few examples are demonstrated in Fig. 4.1. Other topologies are also applicable as long as the decoupled control is achievable, and the PSES is available for absorbing oscillations. More phases can be added in case of a higher power rating [72]. Moreover, the primary-side or secondary-side can be configured to a three or higher voltage level structure [73] to achieve a higher voltage blocking capability and better performance. Case B is selected here as an example and is analyzed and discussed in detail in the rest of this chapter to demonstrate the proposed approach.

In this converter, PSES can be realized by a battery, a supercapacitor, or a capacitor. In the case of a battery or a supercapacitor, it forms a three-port converter and the voltage at PSES is relatively stable. Moreover, the energy storage can help to fix the operating point of the FCS during EIS. If it

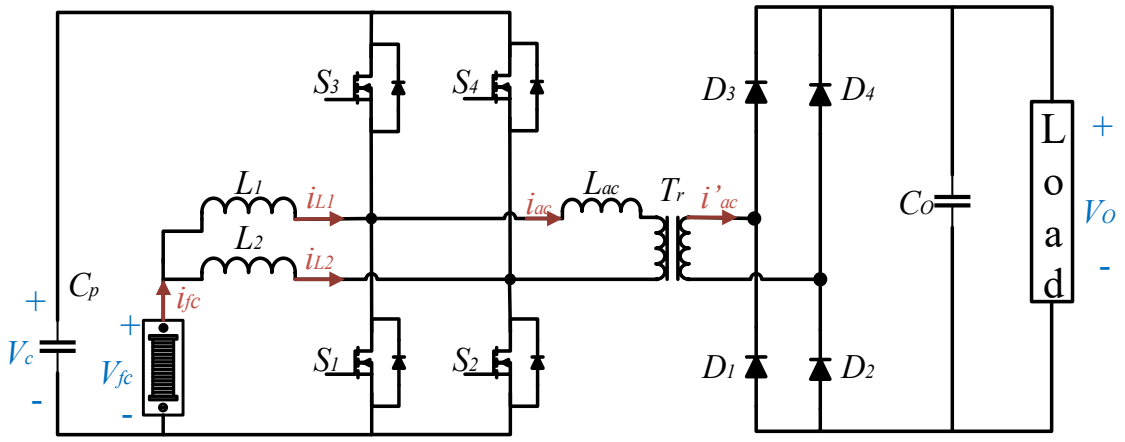

Fig. 4.2. Circuit diagram of Case B.

is expected to be used in the powertrain of an FCV and regenerative braking is needed, the secondary side diodes of Case B need to be replaced with power switches. On the other hand, the operating point is fixed with an extra energy storage or a dumping resistor on the dc link when a capacitor is used as the PSES. In this case, what proposed is a stand-alone two-port converter. Unlike the capacitor on the dc link, certain voltage ripples on PSES are accepted, as long as it is within the electrical rating and retains functional operations of the converter. Hence, the capacitance of PSES can be sized smaller, while the dc link capacitor is designed to switching ripple only. As using a capacitor is more complex in designing, it is further elaborated in this chapter.

4.1.1 Operating Principle of the Proposed Isolated Converter

The proposed converter is depicted in Fig. 4.2 in detail, where the input side is formed by an H bridge with S_1, S_2, S_3 and S_4 as power switches, L_1 and L_2 are input inductors and C_p is the PSES. T_r is the high-frequency transformer with N:1 conversion ratio, and L_{ac} is the leakage inductor. The output side comprises of a full-bridge diode rectifier and an output filter capacitor C_o. The fuel cell output voltage and current are V_{fc} and I_{fc} respectively, and I_{fc} is shared by the currents on inductors I_{L1} and I_{L2}. V_c is the voltage of PSES. Currents at primary-side and secondary-side of T_r are I_{ac} and I_{ac}' respectively. The output voltage is V_o. The duty cycle d is referred to the turn-on period of upper switches S_3 and S_4. The phase shift φ is defined as the leading turn-on angle of S_3 in respect to S_4.

A similar topology and its modeling and control were discussed in [74], applied to interface multiple energy sources. To achieve the decoupled control, phase shift φ needs to satisfy $\varphi \leq$

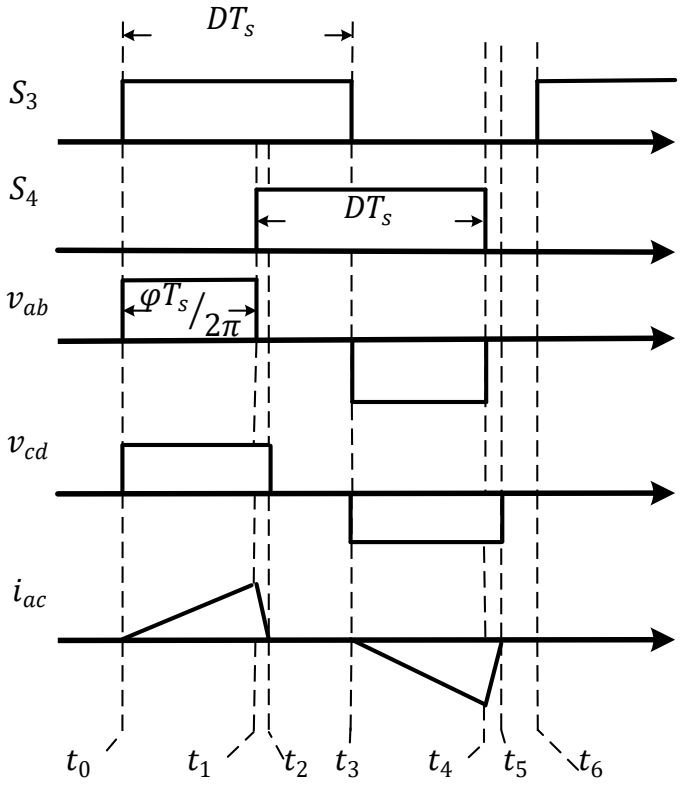

Fig. 4.3. Converter waveforms in the decoupled control mode.

$\min\{2\pi D, 2\pi(1-D)\}$. The key waveforms under this condition are depicted in Fig. 4.3. It is intuitively known from this figure that the overlapped period of S_3 and S_2 is solely controlled by φ under this condition, which changes the length of the non-zero period of v_{ab} and i_{ac}. The power transferred from the primary side to secondary side is the product of v_{ab} and i_{ac}. Thus, the power transferred to the load is controlled only by φ in this mode. Ignoring the deadtime and assuming all components are ideal, the time domain analysis of each period is given as below.

- $[t_0\text{- } t_1]$: At t_0, S_3 is turned on, and S_2 is still on, $v_{ab} = V_c$. D_2 and D_3 are conducting on the secondary side, $v_{cd} = NV_o$. i_{ac} increases with a slop of $(V_c\text{-}NV_o)/L_{ac}$ to its peak $i_{ac\text{-}pk}$. This stage ends when S_4 turns on.
- $[t_1\text{- } t_2]$: In this stage, S_2 is turned off, and S_3 and S_4 are on, $v_{ab} = 0$. On the secondary side, D_2 and D_3 continue to conduct, $v_{cd} = NV_o$. i_{ac} starts to decrease from $i_{ac\text{-}pk}$ and reaches zero before t_3. The falling slop is $-NV_o/L_{ac}$.
- $[t_2\text{- } t_3]$: At t_2, i_{ac} reaches zero and D_2 and D_3 stops to conduct, $v_{cd} = 0$. S_3 and S_4 continue to conduct on the primary side and this stage ends when S_3 is switched off.

Periods from t_3 to t_6 are the same as [t_0- t_3] with an opposite direction of i_{ac}. So, the analysis is omitted here. In this mode, i_{ac} is discontinuous and phase shift and duty cycle are decoupled, named as the decoupled mode, it reduces the control complicity in separating the controls of output power and EIS operations. Although the power transfer capability is limited in the decoupled mode [74], no circulating power has occurred, as shown in Fig. 4.3, where v_{ab} and i_{ac} hold the same polarity in all periods. Therefore, higher efficiency is achieved and it is preferred to operate converter in this mode.

4.1.2 Converter Design Case of Proposed CF-Isolated Converter

The fuel cell output curve is taken into consideration in this section to ensure the converter is operated in the decoupled mode in the entire operating range of an FCS, while achieving soft switching as well.

From the above time period analysis, the peak value of i_{ac} is obtained as

$$I_{ac\_pk} = \frac{V_c - NV_o}{L_{ac}} \frac{\varphi}{2\pi} T_s \tag{4.1}$$

From t_2 to t_1, i_{ac} decreases from its peak value to zero. Thus, the duration of this period is

$$t_2 - t_1 = \frac{V_c - NV_o}{NV_o} \frac{\varphi}{2\pi} \tag{4.2}$$

The output power is calculated as

$$P_o = \frac{1}{T_s} \int v_{ab} i_{ac} dt = \frac{V_c(V_c - NV_o)}{L_{ac}} \left(\frac{\varphi}{2\pi}\right)^2 T_s \tag{4.3}$$

As shown in (4.3), the output power is proportional to φ. In steady state, the duty cycle equals the ratio of V_{fc} and V_c. Therefore, the constrain of decoupled mode is rewritten here as

$$\varphi \leq min\left\{2\pi \frac{V_{fc}}{V_c}, 2\pi\left(1 - \frac{V_{fc}}{V_c}\right)\right\} \tag{4.4}$$

By combining (4.3) and (4.4), the following inequality is obtained:

$$P_o \leq \frac{T_s}{L_{ac}} min\left\{\frac{V_c - NV_o}{V_c} V_{fc}^2, \frac{V_c - NV_o}{V_c}\left(V_c - V_{fc}\right)^2\right\} \tag{4.5}$$

From (4.5), in the case of $V_c > 2V_{fc}$, a higher output power range is achieved.

An illustrative V-I curve of an FCS output is depicted in Fig. 4.4. This curve can be obtained by testing or from the datasheet of an FCS. The output of the FCS has a soft output characteristic, and it is normally preferred to operate in the linear range. Operating close to the open-circuit voltage tends to accelerate the degradation of FCS as pointed out in [75], Pt particles will dissolve in this condition. The FCS output curve can be approximated with a first-order linear model with

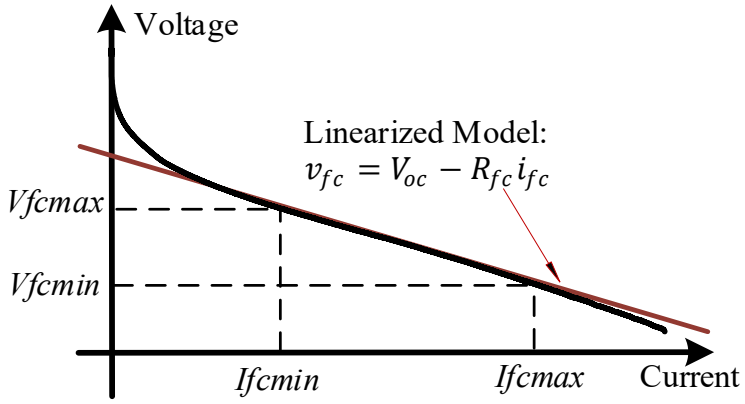

Fig. 4.4. V-I of an FCS output and its linearized model in the linear region.

the output voltage from V_{fcmax} to V_{fcmin} in the linear range. The approximated steady state model is given as

$$v_{fc} = V_{oc} - R_{fc} i_{fc} \tag{4.6}$$

where V_{oc} is the open-circuit voltage and R_{fc} is the total internal resistance.

To illustrate the design process, 1.2 kW Nexa fuel cell module [76] is taken as an example here. This example is a scale-down FCS, however, still convey the proposed designing principles. The full operating voltage is between 26 V and 43 V, while the output voltage varies from 27 V to 36 V in the linear range, and its current changes from 45 A to 10 A accordingly. Therefore, its linearized model is derived as $v_{fc} = 38.5714 - 0.2571 i_{fc}$. The output power curves, the red dash line, and the converter output power limits are illustrated in Fig. 4.5 according to (4.5) with different values of V_c in the whole operating range of the FCS. The solid lines need to be above the fuel cell output power dash line indicating the decoupled control is achieved in the entire fuel cell linear range with the selected values of V_c. With the increase of V_c, the output power range is enlarged at the expense of higher voltage stress on primary side switches. From this figure, it is shown that V_c is at least 70 V in order to operate in the decoupled mode within the entire linear region of the fuel cell module. V_c is selected as 80 V in the following discussions.

On the other hand, achieving zero voltage switching (ZVS) is one of the advantages of adopting isolated phase-shifted converters. ZVS turn-on is achieved when the antiparallel diode of MOSFET is still on before the turn-on gating signal arrives, which gives the following criteria for each switch on the primary side:

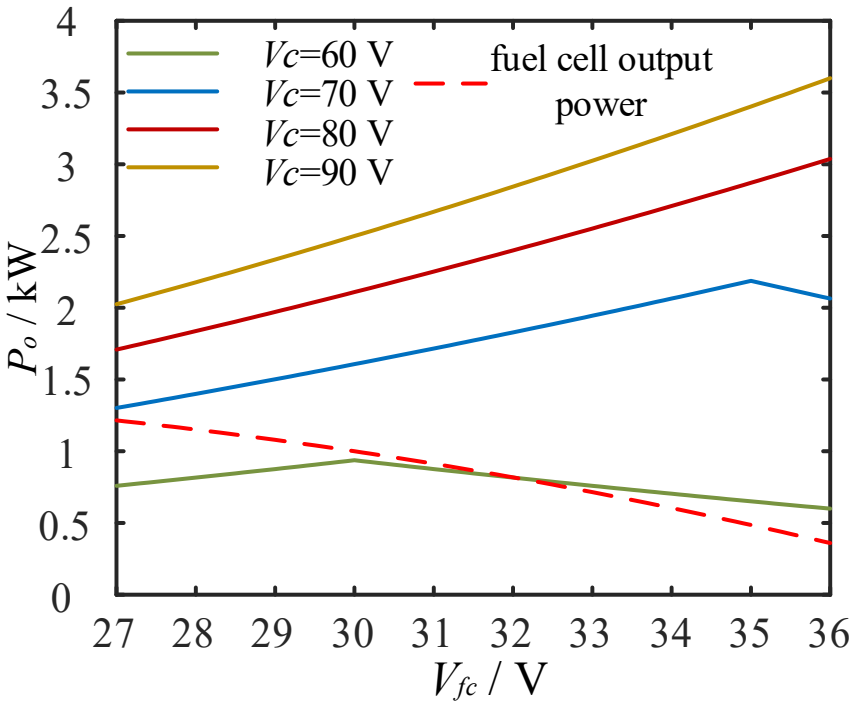

Fig. 4.5. Comparison of power transfer capability with different values of V_c under decoupled control. The parameters are: T_s = 0.02 ms; L_{ac} = 3.2 uH; N = 0.5 and V_o = 100 V; the dash line is the fuel cell output power, and the solid lines are the maximal converter output power in the decoupled mode with different values of V_c.

$$\begin{cases} i_{ac}(t_3) - I_{LL} \geq 0 & S_1 \\ i_{ac}(t_4) + I_{LL} \leq 0 & S_2 \\ i_{ac}(t_0) - I_{LH} \leq 0 & S_3 \\ i_{ac}(t_1) + I_{LH} \geq 0 & S_4 \end{cases} \tag{4.7}$$

where $\begin{cases} I_{LH} = \frac{P_o}{2V_{fc}} + \frac{V_{fc}(1-D)T_s}{2L_1} \\ I_{LL} = \frac{P_o}{2V_{fc}} - \frac{V_{fc}(1-D)T_s}{2L_1} \end{cases}$ and $\begin{cases} i_{ac}(t_3) = 0 \\ i_{ac}(t_4) = -i_{ac\_pk} + \frac{NV_o t_d}{L_{ac}} \\ i_{ac}(t_0) = 0 \\ i_{ac}(t_1) = i_{ac\_pk} - \frac{NV_o t_d}{L_{ac}} \end{cases}$. t_d is the deadtime between two gating signals between the upper and lower switches in the same leg.

As shown in (4.7), ZVS is guaranteed for S_3 and S_4, while it is not possible to achieve ZVS for S_1. ZVS region of S_2 according to the variation of V_{fc} is obtained:

$$-\sqrt{\frac{T_s V_{fc}(V_c - NV_o)(V_{oc} - V_{fc})}{V_c L_{ac} R_{fc}}} + \frac{NV_o}{L_{ac}} t_d + \frac{V_{oc} - V_{fc}}{2R_{fc}} - \frac{T_s V_{fc}(V_c - V_{fc})}{2L_1 V_c} \leq 0 \tag{4.8}$$

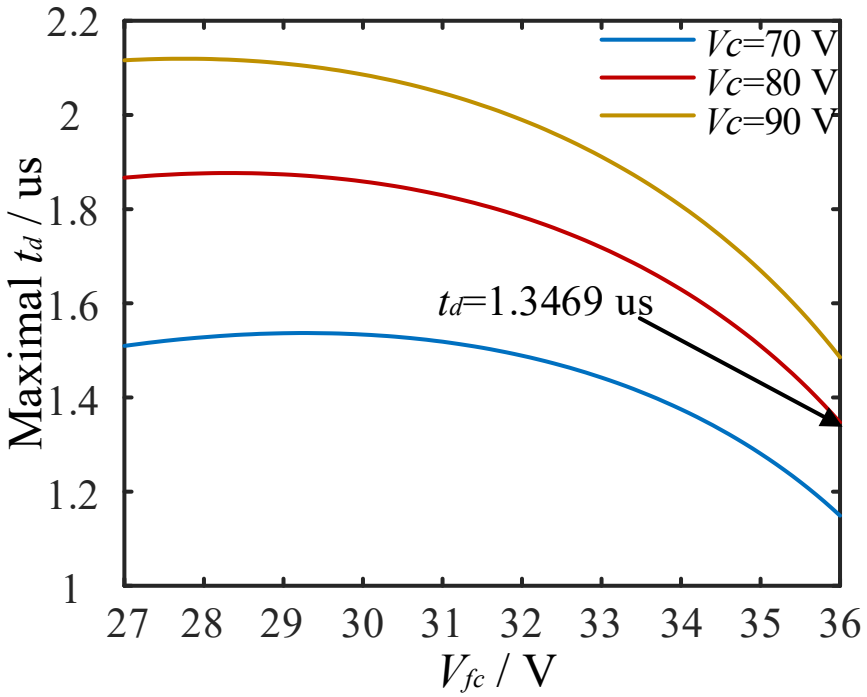

Fig. 4.6. Maximal deadtime to achieve ZVS of S_2 for different V_c (Same parameters as in Fig. 4.5.).

From the inequality in (4.8), the maximal deadtime in the whole operating range is illustrated in Fig. 4.6 under different V_c. The maximal t_d is 1.3469 us to ensure ZVS of S_2 when V_c is 80 V. t_d is selected as 0.2 us in the following to accomplish ZVS in the entire operating range of fuel cell.

Moreover, as the output diodes turn off when i_{ac} reaches zero, zero current switch (ZCS) is accomplished for all diodes, avoiding reverse recovery losses. By achieving soft switching, operating in decoupled mode and adopting SiCs with superior switching performances or low on-resistance MOSFETs for S_1- S_4, the converter efficiency is increased and switching frequency can be pushed higher than hard-switching converters to achieve perturbations at a higher frequency for EIS.

As described above, the oscillations brought by EIS are guided to the PSES as the design target of the proposed converter during EIS. Thus, its capacitance needs to be properly sized here to maintain the highest oscillations within an acceptable range to make sure that the converter works appropriately.

The output power from an FCS during EIS is divided into dc and ac components, given as

$$P_{fc} = \left(V_{fc}^{dc} + v_{fc}^{ac}\right)\left(I_{fc}^{dc} + i_{fc}^{ac}\right) \tag{4.9}$$

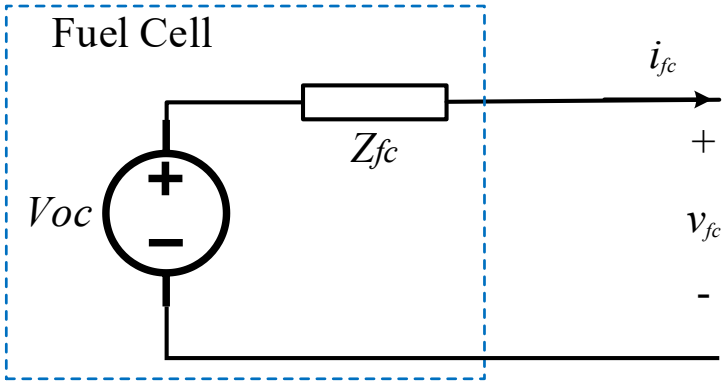

Fig. 4.7. FCS model.

where I_{fc}^{dc} and i_{fc}^{ac} are the dc and ac component of the output current during EIS and V_{fc}^{dc} and v_{fc}^{ac} are the corresponding components of output voltage induced. Therefore, the dc power is transferred to the load and the ac ones are expected to be mainly absorbed by PSES.

A simplified FCS model is depicted in Fig. 4.7 with an open-circuit voltage V_{oc} and internal impedance Z_{fc}, where Z_{fc} is expected to be detected with EIS. Z_{fc} is differentiated from R_{fc} in (4.6) as it is a complex impedance with both real and imaginary parts here, $Z_{fc} = RE_{fc} + jIM_{fc}$. The relation between the output current and voltage is

$$V_{fc} = \underbrace{\left(V_{oc} - Z_{fc}I_{fc}^{dc}\right)}_{V_{fc}^{dc}} - \underbrace{Z_{fc}i_{fc}^{ac}}_{v_{fc}^{ac}} \tag{4.10}$$

In (10), the first part is the dc component V_{fc}^{dc} and the second part are the ac component v_{fc}^{ac}. Assuming the generated ac current perturbation is $0.1I_{fc}^{dc}\sin(\omega t)$ and taking (4.10) to (4.9) gives

$$P_{fc} = P_{fc}^{dc} + 0.1P_{fc}^{dc}\,sin(\omega t) - 0.1Z_{fc}{I_{fc}^{dc}}^2\,sin(\omega t) - 0.01Z_{fc}{I_{fc}^{dc}}^2\,sin^2(\omega t) \tag{4.11}$$

where P_{fc}^{dc} is the production of dc components of voltage and current.

The ripple power caused by EIS operation is expressed as

$$P_{ripple} = 0.1P_{fc}^{dc}\,sin(\omega t) - 0.1Z_{fc}{I_{fc}^{dc}}^2\,sin(\omega t) - 0.01Z_{fc}{I_{fc}^{dc}}^2\,sin^2(\omega t) \tag{4.12}$$

All the instantaneous ripple power caused by EIS in (4.12) at the fuel cell output is expected to be absorbed or supported by the PSES.

The instantaneous energy stored in a capacitor is given by

$$E = 0.5C_p v_c^2 \tag{4.13}$$

where the PSES voltage v_c is composed of its dc and ripple components, V_c and Δv_c.

The instantaneous energy balance between the ripple power in (4.12) and the stored energy in PSES in (4.13) gives

$$\int P_{ripple} dt = 0.5 C_p \Delta v_c^2 + C_p V_c \Delta v_c \tag{4.14}$$

By a few steps of manipulations, it can be expressed as

$$\Delta v_c = -V_c + \sqrt{V_c^2 + \frac{2|P_{ripple}|}{C_p \omega}(1 - cos(\omega t))} \tag{4.15}$$

The magnitude of this oscillation is given as

$$|\Delta v_c| = -V_c + \sqrt{V_c^2 + \frac{4|P_{ripple}|}{C_p \omega}} \tag{4.16}$$

Equation (4.16) reveals the factors influencing the oscillation magnitude when all the oscillations are ideally absorbed by the PSES. To select a sufficient C_p, the highest P_{ripple} can be estimated here as $0.1P_{fc}^{dc}\sin(\omega t)$. This is because that $Z_{fc}(I_{fc}^{dc})^2$ is the power dissipated on the internal impedance, which is significantly smaller than the power delivered from fuel cell P_{fc}^{dc}, and the second-order harmonic term is even smaller. Therefore, (4.15) can be rewritten as

$$|\Delta v_c| = -V_c + \sqrt{V_c^2 + \frac{0.4P_{fc}^{dc}}{C_p \omega}} \tag{4.17}$$

As shown in the above equation, the magnitude of oscillation is affected by the dc operating point of the FCS, EIS frequency and the capacitance of PSES. Looking at (4.12) and (4.16), the increase of internal resistance tends to damp the oscillations, as the result of reduced P_{ripple}, and helps to reaches a lower EIS frequency for the same magnitude of oscillation. This is a favorable feature. Since the total resistance of an FCS tends to increase with the usage and the occurrence of faults [9]-[14], [35]-[37], [42]-[44], the capacitance of PSES is sufficiently sized for its entire lifetime to a healthy stack at the beginning of its service.

4.2 Experimental Verifications

The experimental results of the proposed converter, targeting to an emulated FCS, are presented here. The FCS is emulated through a dc voltage source and an impedance emulating circuit, which is a linear Randle's circuit as used for experimental verifications in chapter 2. The parameters of the emulated FCS and converter are given in Table 4.1.

The designed control loop is shown in Fig. 4.8, where φ is used to regulate output current and d is adopted for PSES voltage control in normal operation and generating ac perturbation in EIS

Table 4.1. Fuel Cell and Converter Parameters of Isolated Converter

	Symbol	Value
Parameters used in Emulated Circuit	V_{fc0}	45 V
	R_m	0.1396 Ω
	R_{ct}	0.0742 Ω
	C_{dl}	30 mF
Parameters of Converter	L_1 & L_2	300 uH
	C_p	2 mF
	C_o	1 mF
	N	0.5
	L_{ac}	3.2 uH

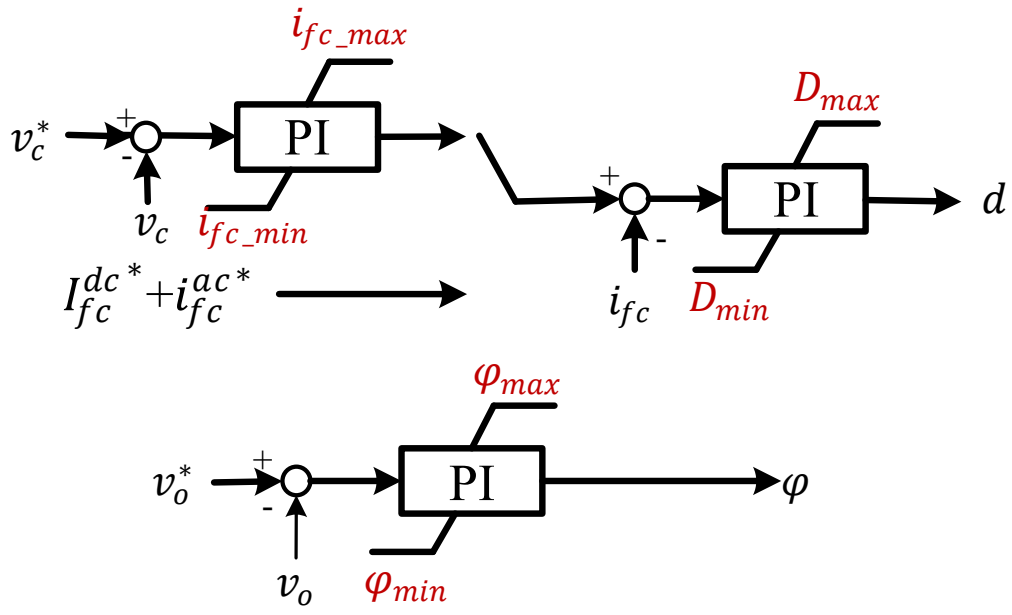

Fig. 4.8. Control loops for the isolated CF converter.

mode. The fuel cell current reference is switched from PSES voltage outer loop to a current reference when the EIS is triggered. It is a combination of the dc operating point and the reference of imposed ac perturbations. I_{fc}^{dc*} is the averaged reference output from v_c control loop obtained

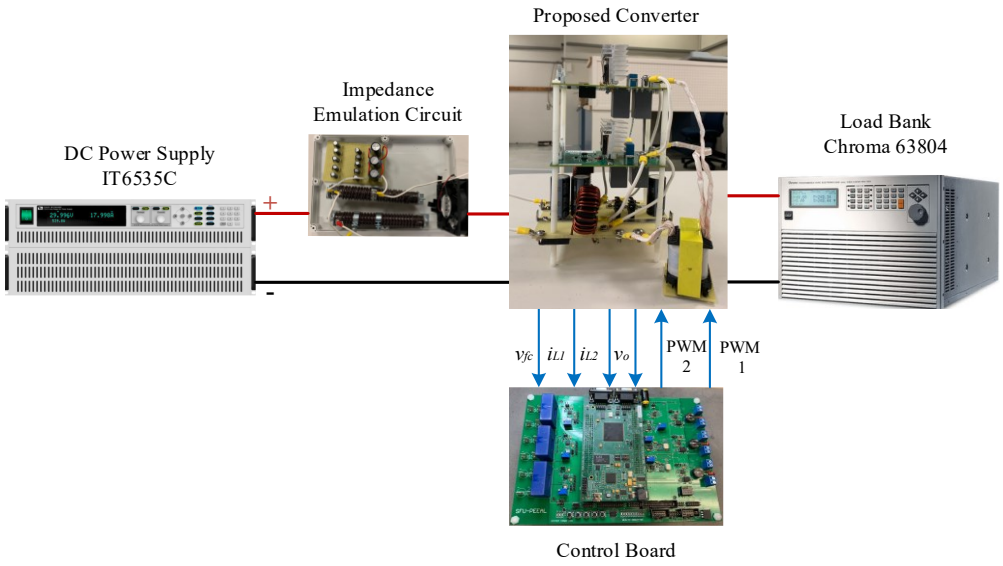

Fig. 4.9. Experimental setup of the proposed isolated CF converter.

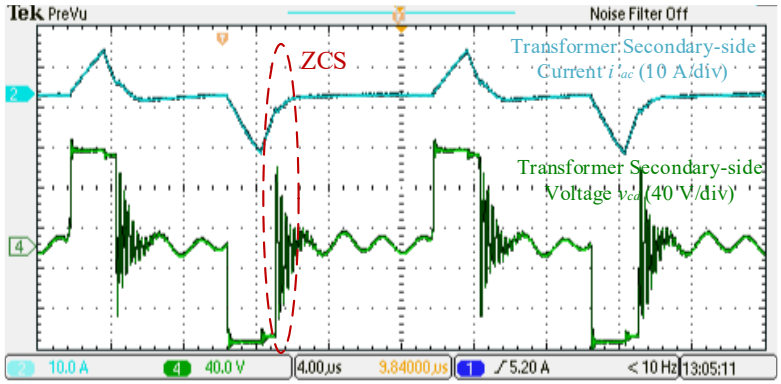

(a)

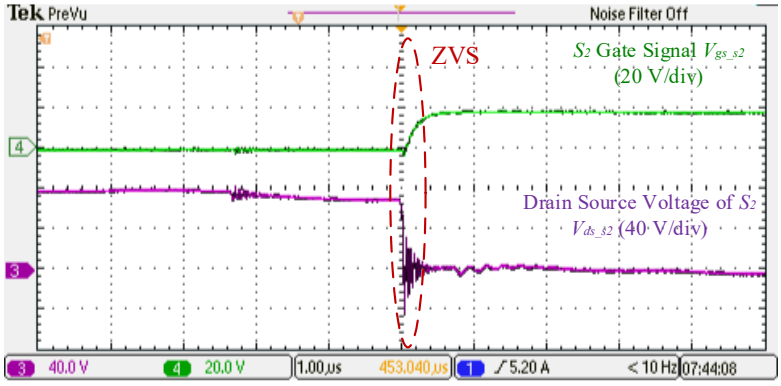

(b)

Fig. 4.10. Experimental results of (a) secondary-side diodes ZCS and (b) primary-side MOSFET S_2 ZVS with 200 W power output.

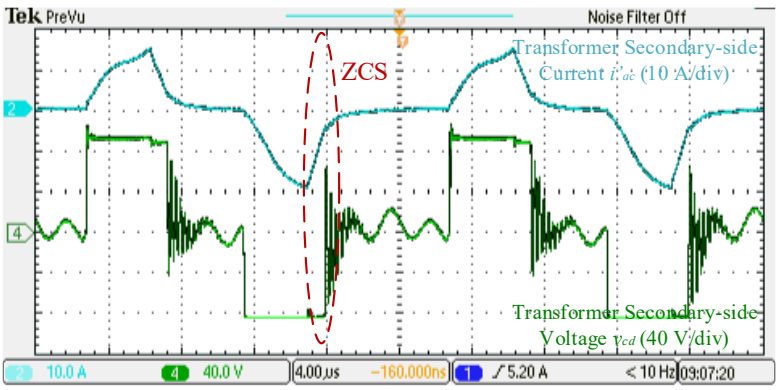

(a)

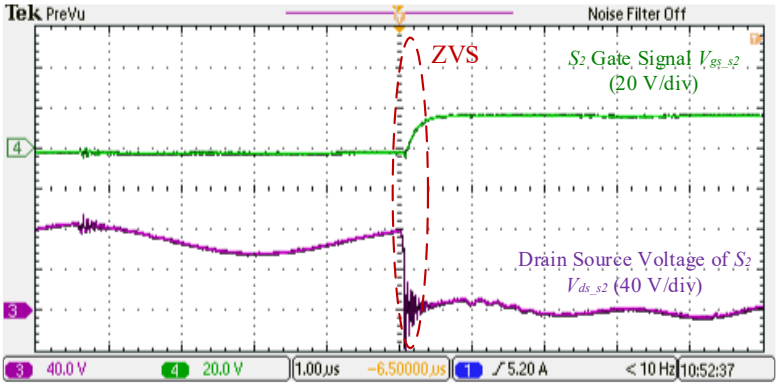

(b)

Fig. 4.11. Experimental results of (a) secondary-side diodes ZCS and (b) primary-side MOSFET S_2 ZVS with 500 W power output.

before starting of EIS since the converter needs to operate at the same operating point for a period to stabilize the internal dynamics of an FCS. I_{fc}^{dc*} is the sinusoidal ac perturbation with the magnitude of 10% of I_{fc}^{dc*}. Saturations are set to the output of v_o controller to make sure the decoupled control criterion is met. The three PI controllers are designed at the full-load condition based on the parameters of this converter. The switching frequency of this converter is 50 kHz.

A laboratory-scale hardware prototype is built based on parameters listed in Table 4.1. The experimental setup is shown in Fig. 4.9, where a dc power supply is connected to an impedance emulation circuit and the load bank is set to constant resistant load, assuming the operating point of fuel cell is fixed with energy storages or dumping resistors. The testing equipment used are Tektronix DPO2014 digital oscilloscope, Tektronix TCP0030 current probe and P5205A-NEW high-voltage differential probe.

The zoom-in diagrams of the load power at 200 W and 500 W during normal operation are given in Fig. 4.10 and 4.11. The switching waveform of S_2 proves ZVS is achieved with the

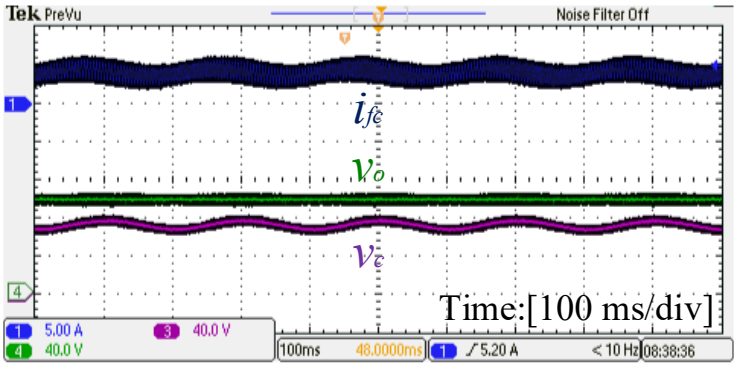

(a) 5 Hz

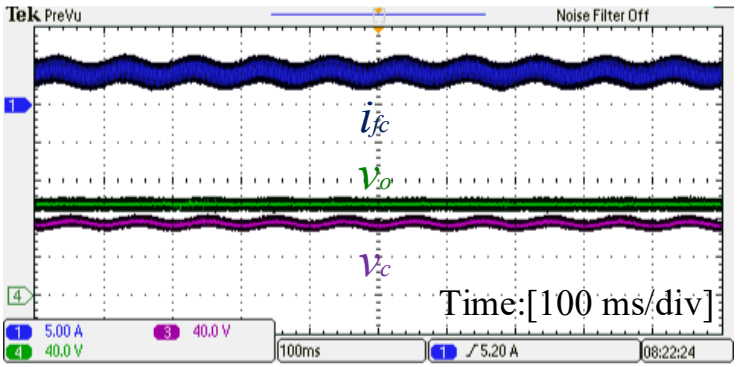

(b) 10 Hz

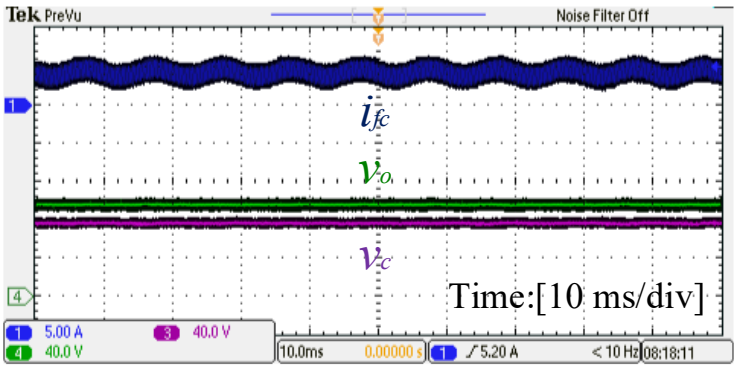

(c) 100 Hz

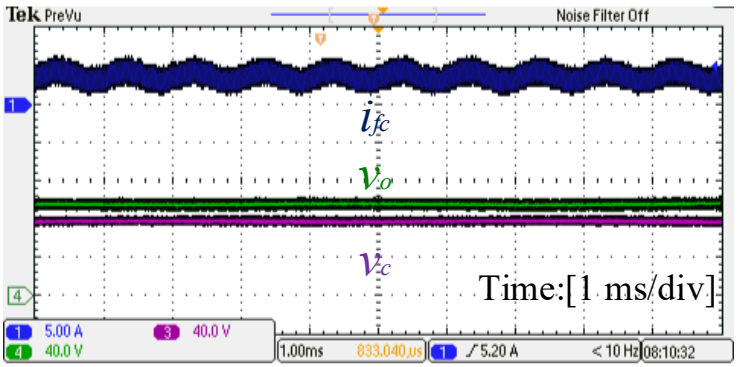

(d) 1000 Hz

Fig. 4.12. Experimental results of input current i_{fc}, primary side capacitor voltage v_c and output voltage v_o during EIS mode with load power at 200 W.

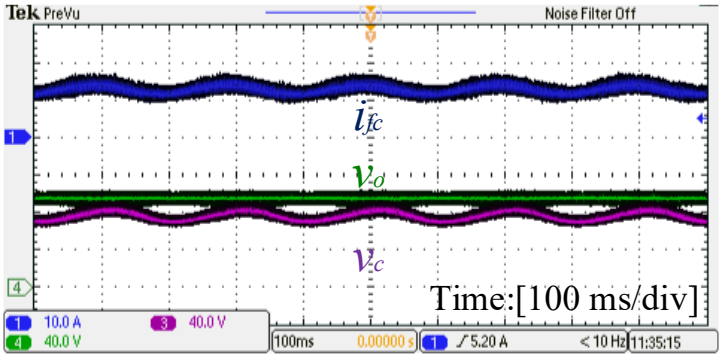

(a) 5 Hz

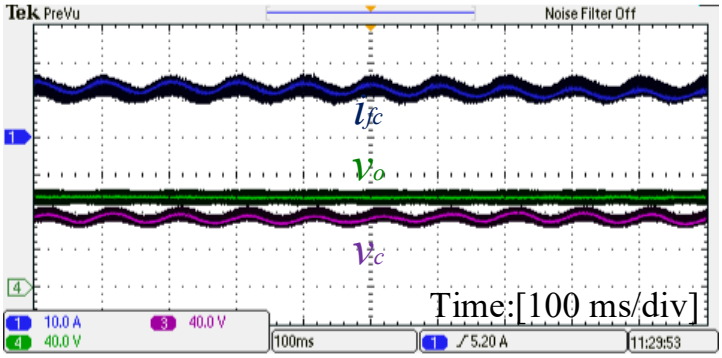

(b) 10 Hz

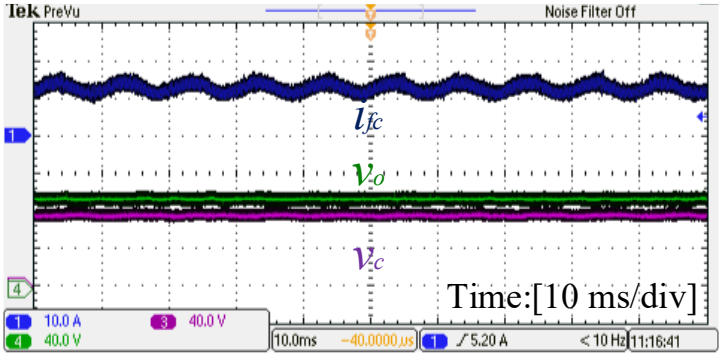

(c) 100 Hz

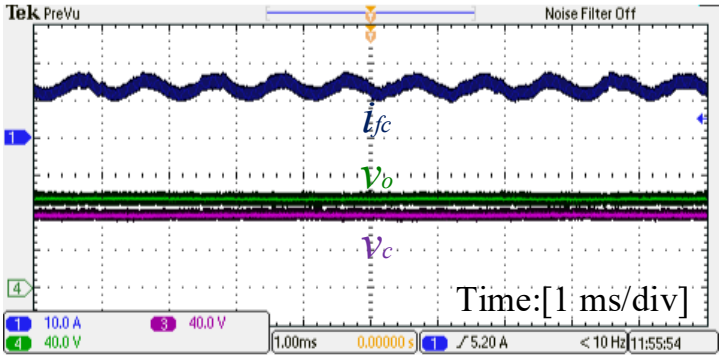

(d) 1000 Hz

Fig. 4.13. Experimental results of input current i_{fc}, primary side capacitor voltage v_c and output voltage v_o during EIS mode with load power at 500 W.

proposed design under various power outputs. ZCS waveforms of D_1 are also shown here, while ZCS is achieved for all diodes. From the transformer current waveform in Fig. 4.10 (a) and Fig. 4.11 (a), reactive power is eliminated in the decoupled mode. High efficiency is achieved, therefore, high frequencies perturbations for EIS can be excited.

The waveforms when EIS is triggered at 5 Hz, 10 Hz, 100 Hz and 1000 Hz under 200 W and 500 W operating points are shown in Fig. 4.12 and 4.13 respectively. As shown in the presented results, required various frequency sinusoidal current waveforms are generated at the fuel cell input to trigger the EIS operation. It is shown that the oscillations appeared on the PSES are minimal at the high frequency, i.e., 1000 Hz, while they are observed at low EIS frequencies and a lower EIS frequency induces a higher magnitude of oscillations. As expected, the oscillations brought by EIS operation are absorbed by PSES, leaving a clean constant output voltage. Therefore, the inverter stage connected will not be affected. By comparing Fig. 4.12 and 4.13 with the same EIS frequency, the higher output power leads to the higher oscillation magnitude on PSES. It can be concluded that the oscillation magnitudes are affected by the dc operating point and EIS frequency as illustrated in (4.17). Higher EIS frequencies can be achieved as long as the bandwidth is sufficient and lower frequencies are accomplished with a suitable capacitance according to (4.17).

4.3 Summary and Conclusions

This chapter contributes to bridging the design of the fuel cell PPC and the characteristics of FCS for achieving an extra functionality of the PPC. Hence the PPC will not only deal with efficient power conditioning but provide informative advanced EIS diagnostics as well. A fuel-cell-oriented converter design approach is proposed in this chapter, where the converter is designed according to the output characteristics of an FCS at normal conditions and the EIS function with a wide frequency range is incorporated in the converter topology. The challenges of achieving high and low ends of EIS frequencies from converter are identified. The proposed converter achieves high efficiency by employing decoupled mode, soft switching and/ or adopting new devices with superior performances. Therefore, the incorporated EIS function achieves high-frequency perturbations in the current control loop with extended control bandwidth. The oscillations brought by EIS operation are absorbed by PSES, leaving no disturbance to the load. With the proposed converter and control, the EIS function is maintained within the converter itself and need no system

level resizing or redesigning during integration and assembly. Therefore, wide-frequency-range perturbations of EIS are excited with the proposed converter and bringing no disturbance to the interconnected electrical systems in a powertrain.

Chapter 5 A New Auxiliary Converter Solution for Generating ac Perturbations for FCS EIS

Including the ac perturbations in the existing main PPC as presented Chapter 2 and 3 may require higher ratings of the components since the perturbations are imposed upon the normal dc operating point. Moreover, the control bandwidth is usually limited in high-power PPCs for generating high-frequency perturbations and EIS oscillations are introduced to the interconnecting system, while the firmware of the PPC also needs to be updated and re-tested. In view of these issues, a separate dc/dc converter was proposed in [48], [49], for decoupled operation of generating the EIS ac perturbations in the fuel cell system. This solution is able to eliminate the needs for re-design and re-validating the high-power main PPC, but the second dc/dc converter still carries a dc offset and the energy is wasted on a dumping resistor [49], which detract from its overall attractiveness.

To this end, this chapter proposes a new solution with a separate converter that only processes the required EIS perturbations with the ac energy cycling through a load side energy buffer, named auxiliary converter. This converter generates needed frequencies of EIS ac perturbations enabling *in situ* EIS diagnostics for FCS in automotive powertrains, stationary power supplies, or an offline testing bench. As an add-on component, the auxiliary converter is dedicated for EIS operations and is independent of the main power transfer path. It processes pure ac perturbations with only an energy buffer on the load side, featuring high compactness and great flexibility. Designated as an auxiliary converter, this solution allows the use of components of lower ratings and does not require a dumping resistor and its associated heat sink. It works similarly to a reactive power generator connected to the FCS output port, presenting the needed EIS ac current perturbations to it. Thanks to its detached status in the configuration and standalone operation capability, the auxiliary converter can function as a plug and play module without depending on any other components in the system and the oscillations induced by the EIS operation is therefore contained within the auxiliary converter without disturbance the main power path. This provides great

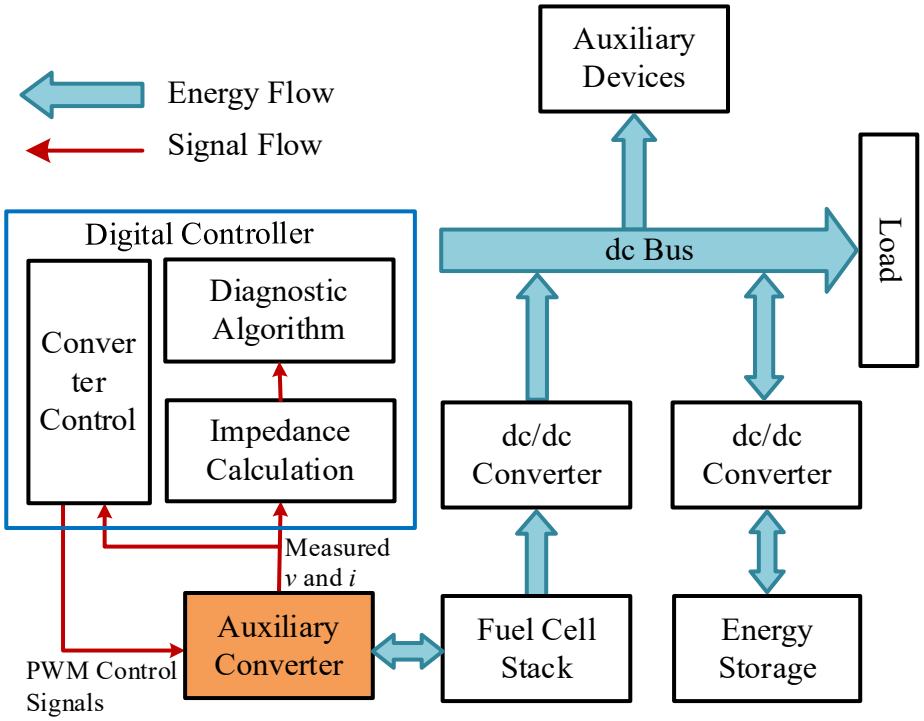

Fig. 5.1. Illustrative diagram of a hybrid fuel cell powertrain with *in situ* EIS enabled by an auxiliary converter.

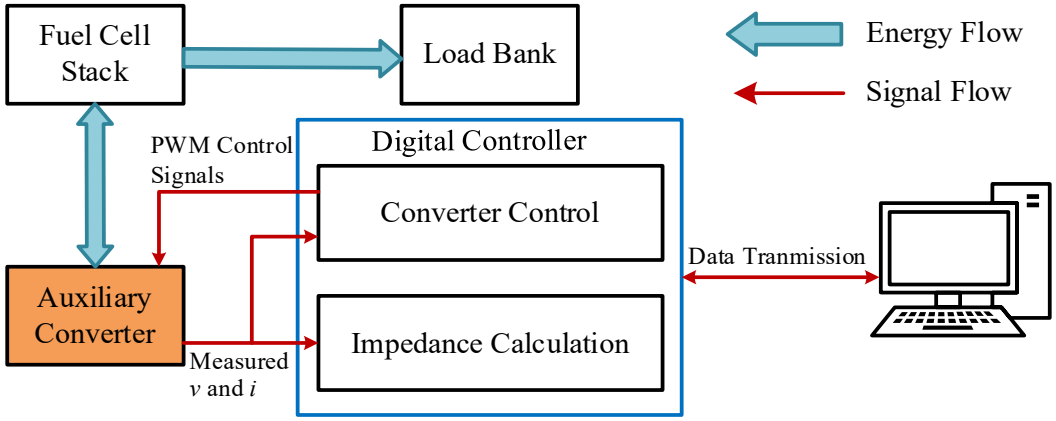

Fig. 5.2. Illustrative diagram of an offline testing setup with *in situ* EIS based diagnostic function embedded in the converter controller.

flexibilities to the placement of this device. For instance, it can be installed in the powertrain when EIS is required during the system integration process; alternatively, it can also be placed directly inside of a stack as an add-on self-diagnostic function module, providing advanced features from the fuel cell manufacturer's perspective. With the compact design of this auxiliary converter, it can be installed as close to the fuel cell as possible to eliminate the inductive effect of wires [35],

which would otherwise greatly influence the accuracy of impedance measurements from the FCS at high frequencies. Moreover, since the auxiliary converter only process a small portion of the power, the switching frequency of the converter can be pushed higher to induce high-frequency perturbations without introducing excessive power losses.

In the following, Section 5.1 presents the overall system description of the proposed auxiliary converter solution, including its working principle, control system design, and the sizing procedure of the load side capacitor. Simulation and experimental results are presented in Section 5.2. Finally, conclusions are given in Section 5.3.

5.1 Proposed Auxiliary Converter

5.1.1 System Descriptions

The application scenarios of the proposed auxiliary converter for a hybrid FCV powertrain and an offline testing bench are presented in Fig. 5.1 and Fig. 5.2, respectively. In the vehicle powertrain, the load features a dynamic power demand, and the energy storage is used to fix the operating point of the FCS, as is required during the EIS operation. In the offline testing case, the operating point of a fuel cell is fixed with a load bank or the fuel cell directly charges the on-board battery. The auxiliary converter is inserted in both cases to generate needed ac perturbations for EIS, which ranges from a few kilohertz at the high end to a few hertz or sub-hertz at the low end. With the integrated sensors in the auxiliary converter, responses of an FCS to the perturbations can be measured, with which impedances of the FCS can be calculated, and possible diagnostic functions can be implemented within the embedded controller in the case of an on-board application. For offline testing, the impedance spectrum can be transferred to a computer for recording and detailed analysis. It is noted in the figures that the bidirectional energy flow arrow between the FCS and auxiliary converter is because the energy is cycling between the FCS and the auxiliary converter, while the magnitude is much smaller than the dc component pulled through the main fuel cell dc/dc converter. Therefore, the total power from the FCS is always positive.

The generalized diagram of the proposed auxiliary converter is given in Fig. 5.3, where the main design target is to generate the needed ac perturbations at various frequencies interfacing with the FCS. The proposed auxiliary converter is divided into two phases. The front one is a switching network, comprising of power switches, and it withstands the high voltage of the high-power FCS and modulates the required ac perturbations. The later stage is an energy buffer to

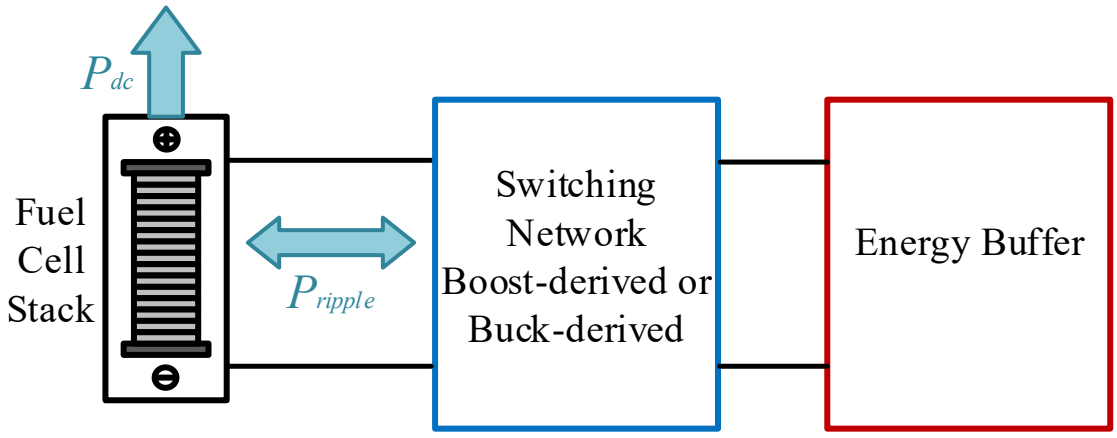

Fig. 5.3. Generalized illustrative diagram of the proposed auxiliary converter for FCS EIS.

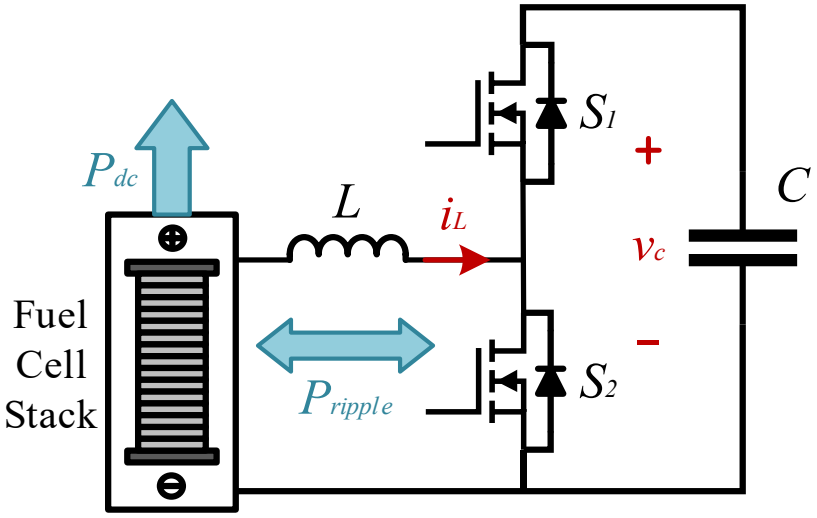

Fig. 5.4. Proposed auxiliary converter topology for FCS EIS.

cycle the energy and provide needed support for the front stage functionality. As indicated in Fig. 5.3, the switching network can be realized with either a bidirectional boost-derived or buck-derived converter, while the energy buffer can be a capacitor or a supercapacitor or a battery.

The schematic diagram of one of the realizations for the proposed auxiliary converter is shown in Fig. 5.4, which is a bidirectional buck-boost converter without a load. The input inductor is L, the half-bridge is formed by two power switches, i.e., S_1 and S_2, and a capacitor C at the load side. Since the auxiliary converter only deals with pure ac current perturbations of about 5~10% the magnitude of the fuel cell dc output current, L can be rated smaller, and MOSFETs can be used

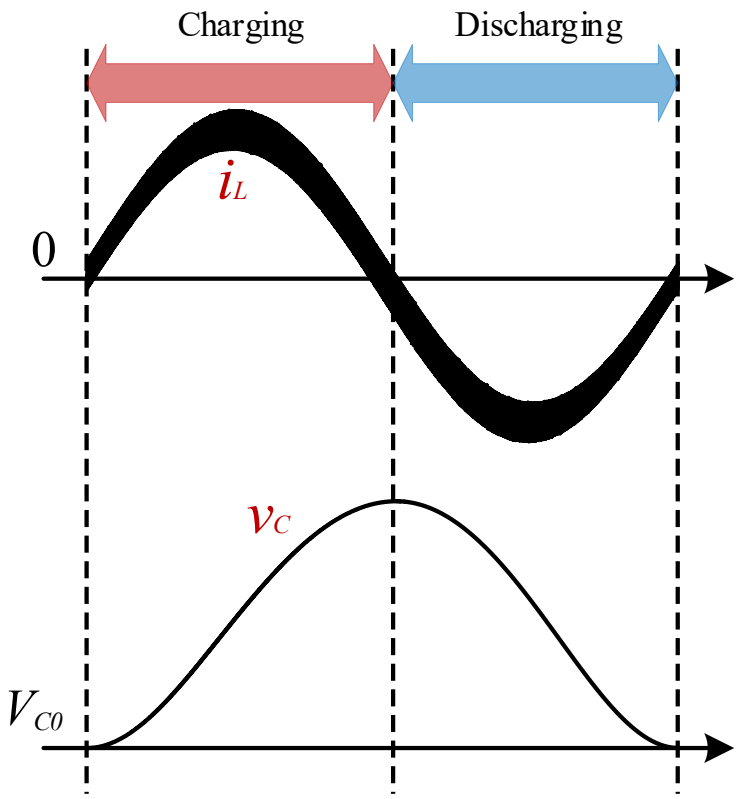

Fig. 5.5. Ideal waveforms of the auxiliary converter of inductor current and capacitor voltage.

for S_1 and S_2 and switched at high switching frequencies. The required ac perturbations are modulated through the converter control over the inductor current i_L, which is a pure sinusoidal ac current. The load side capacitor C serves as an instantaneous energy storage, absorbing oscillations induced from ac perturbations while holding the load voltage level for the proper boost operation. The ideal waveforms of the converter during the EIS operation are shown in Fig. 5.5. The capacitor gets charged during the positive half cycle of i_L and is discharged during the negative half cycle. In this application, large swing on v_c is accepted so that a small capacitance can be utilized.

Assuming i_L equals to $0.1I_{fc}\sin(\omega t)$ as the sinusoidal ac perturbations for EIS, where I_{fc} is the dc current output from the FCS and ω is the angular frequency of EIS perturbations and the magnitude ac perturbations takes 10% of the dc fuel cell current, the output voltage induced is

$$v_{fc} = \underbrace{\left(V_{oc} - Z_{fc}I_{fc}\right)}_{v_{fc}^{dc}} - \underbrace{Z_{fc}i_L}_{v_{fc}^{ac}} \tag{5.1}$$

in which V_{oc} and Z_{fc} are the open-circuit voltage and internal complex impedance as shown in the simplified fuel cell model in Fig. 5.6. As given in (5.1), the dc and ac parts of the output voltage

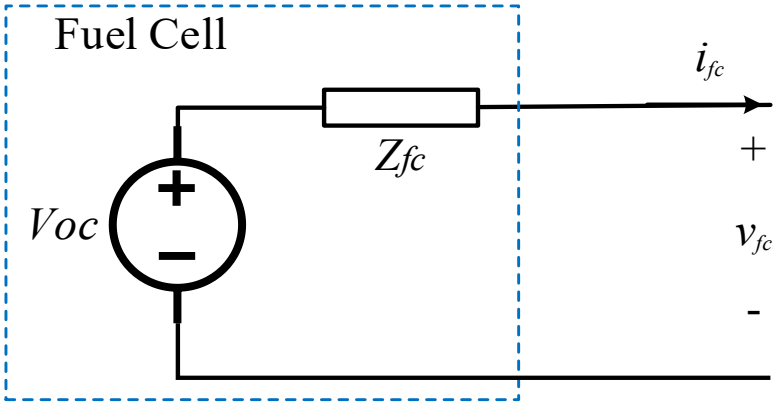

Fig. 5.6. Simplified fuel cell model.

are induced by the fuel cell dc current I_{fc} and ac perturbations from the auxiliary converter i_L, respectively.

Multiplying the output current with the voltage gives

$$P_{fc} = \underbrace{P_{dc} - 0.1Z_{fc}I_{fc}^2\,sin(\omega t)}_{P_{main}} + \underbrace{0.1P_{dc}\,sin(\omega t) - 0.01Z_{fc}I_{fc}^2\,sin^2(\omega t)}_{P_{aux}} \tag{5.2}$$

where P_{dc} is the product of v_{fc}^{dc} and I_{fc} as the dc power from the fuel cell. In a hybrid fuel cell powertrain, the FCS is normally controlled with a fixed output current in the EIS mode, therefore the power transferred through the main power path is the product of v_{fc} and I_{fc} corresponding to P_{dc} and $0.1Z_{fc}I_{fc}^2\sin(\omega t)$ in (5.2), contributing to P_{main}. From (5.2), the power output from the fuel cell is composed of both dc and ripple components during the EIS operation. P_{main} part is transferred to the main load, while the P_{aux} part is expected to be absorbed by the load side capacitor of the auxiliary converter. Since no load is connected to the capacitor, it can accept large ripples as long as the swing does not exceed the electrical rating limits and the boost operation is maintained.

The last term of (5.2) can be re-written as

$$0.01Z_{fc}I_{fc}^2\,sin^2(\omega t) = 0.005Z_{fc}I_{fc}^2 - 0.005Z_{fc}I_{fc}^2\,cos(2\omega t) \tag{5.3}$$

As indicated in (5.3), there is a non-sinusoidal term due to the existence of Z_{fc} in the fuel cell contributing to a small dc term. Moreover, considering the unavoidable converter losses, v_c will eventually experience a slow dc decaying instead of a pure ac oscillation.

In the auxiliary converter, only i_L is controlled, and the dynamic equation of it is

$$L\frac{di_L}{dt} = v_{fc} - dv_c \tag{5.4}$$

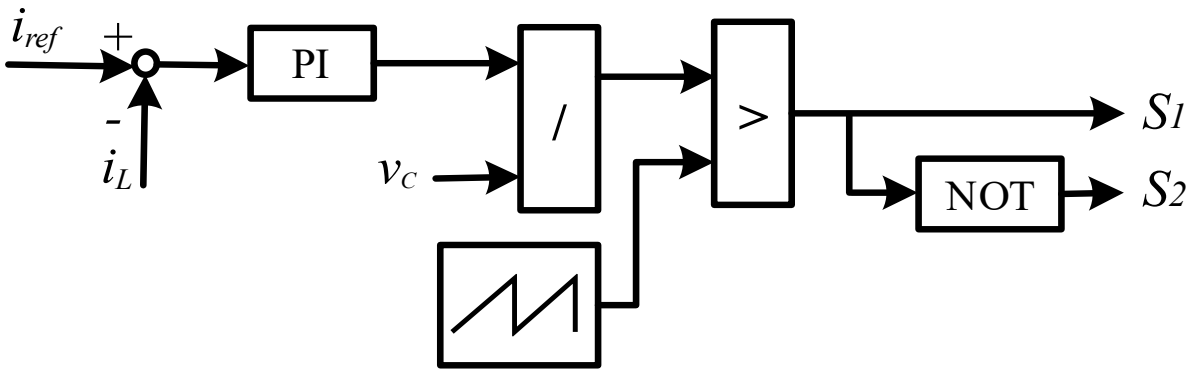

Fig. 5.7. Control block diagram of the auxiliary converter.

v_{fc} is mainly a stable dc voltage with relatively small ripples induced by the EIS operation as the internal impedance is normally only a few milliohms. On the other hand, v_c is allowed to contain large oscillations in order to minimize the load capacitance. From (5.4), it is seen that the control variable d adjusts dv_c from 0 to v_c continuously to obtain a sinusoidal shape needed for i_L. Therefore, d and v_c are coupled. Hence, they are considered as one control parameter first and a PI controller is designed accordingly with the transfer function of -1/Ls. Then, the output from PI is divided by the feedback v_c to obtain the duty cycle of the upper switch S_1. The controller implementation is shown in Fig. 5.7.

5.1.2 Capacitor Sizing

The capacitor needs to be properly sized to absorb P_{aux} in (5.2) while maintaining the maximal voltage in an acceptable range. The energy stored in a capacitor is expressed as

$$E = 0.5Cv_c^2 = \underbrace{0.5CV_{c0}^2}_{E_{dc}} + \underbrace{0.5C\Delta v_c^2 + CV_{c0}\Delta v_c}_{E_{ripple}} \tag{5.5}$$

where V_{c0} is the initial capacitor voltage when EIS is triggered and Δv_c is the ripple voltage. Equation (5.5) is divided into dc energy and the ripple portion formed by Δv_c.

Assuming P_{aux} is ideally exchanged with the auxiliary converter capacitor, the instantaneous energy balancing principle gives

$$\int P_{aux}dt = E_{ripple} = 0.5C\Delta v_c^2 + CV_{c0}\Delta v_c \tag{5.6}$$

By a few steps of manipulations, equation (5.6) can be expressed as

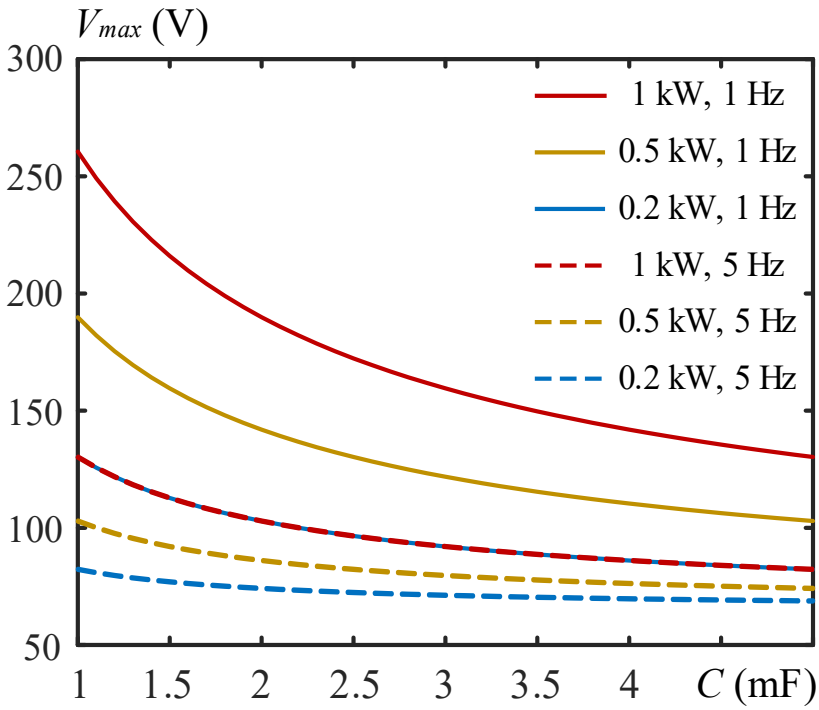

Fig. 5.8. Variations of maximal capacitor voltage magnitude according to different conditions from (5.9), V_{co}= 65 V.

$$\Delta v_c = -V_{c0} + \sqrt{V_{c0}^2 + \frac{2|P_{aux}|}{C\omega}(1 - cos(\omega t))} \tag{5.7}$$

The maximal magnitude of this oscillation is given as

$$V_{max} = |\Delta v_c| + V_{c0} = \sqrt{V_{c0}^2 + \frac{4|P_{aux}|}{C\omega}} \tag{5.8}$$

P_{aux} is expressed in (5.2), however, Z_{fc} is not known since it is the target to be detected with EIS operation. V_{max} is proportional to P_{aux}, thus, to find the worst-case condition, i.e., the highest V_{max}, is to get the highest P_{aux}. The later term of P_{aux} in (2) is relatively small and can be eliminated here. In addition, the second term carries a negative sign. To find the worst-case condition, it is therefore also eliminated. Equation (5.8) can then be expressed as

$$V_{max} = \sqrt{V_{c0}^2 + \frac{4P_{dc}}{C\omega}} \tag{5.9}$$

Here, the highest possible value is set by replacing P_{aux} with P_{dc}. The capacitor is sufficiently sized with (5.9), which reveals the relationship between the maximal capacitor voltage magnitude, the initial capacitor voltage, the fuel cell dc operating point, the load capacitance and the EIS frequency.

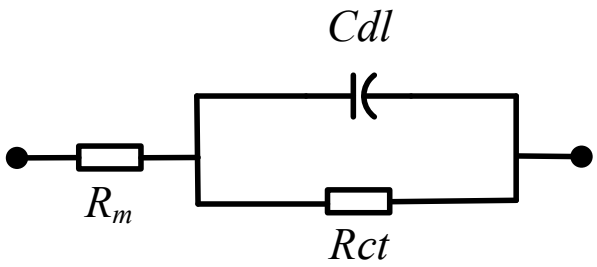

Fig. 5.9. Emulating impedance model used in simulation and experiments.

The variations of the maximal capacitor voltage magnitude under various conditions are presented in Fig. 5.8. It reveals that V_{max} is inversely and directly proportional to the EIS frequency and the fuel cell operating dc power, respectively.

5.2 Simulation and Experimental Verifications

5.2.1 Simulation Results

Simulation in Matlab/Simulink is conducted to evaluate the effect of internal impedance of a fuel cell on the auxiliary converter, where an emulated impedance adopted in [13] is used as shown in Fig. 5.9 with linear elements. The parameters of this impedance and the converter are given in Table 5.1, where they are also adopted in the experiments. Although nonlinear elements were used for emulating the impedance spectrum with semi-circle shapes, the linear elements are also capable of representing the impedance spectrums of FCS and more feasible in the experiments. A constant 20 A is drawn from the fuel cell and EIS frequency is set to 5 Hz, while R_m and C_{dl} are changed respectively to reveal their influences.

The simulation results of the auxiliary converter inductor current and capacitor voltage are given in Fig. 5.10, where needed ac perturbations with 2 A magnitudes are generated at the fuel cell port. It is shown that higher resistance of Z_{fc}, i.e., the real part of Z_{fc}, tends to diminish the oscillations showing on the load side capacitor of the auxiliary converter as expected from previous analyses. This is favorable as both faults and degradations tend to increase the resistance. Therefore, the capacitor is sized for a healthy stack at the beginning of its lifetime is sufficient for the entire usage of an FCS. The capacitor effect of the fuel cell internal impedance is not playing a significant effect on the capacitor voltage oscillation of the auxiliary converter as shown in Fig. 5.10.

Table 5.1. Fuel Cell and Converter Parameters of Auxiliary Converter

	Symbol	Value
Parameters used in Emulated Circuit	V_{fc0}	45 V
	R_m	0.1396 Ω
	R_{ct}	0.0742 Ω
	C_{dl}	30 mF
Parameters of Converter	L	390 uH
	C	1.5 mF
	f_s	50 kHz
	MOSFET	IPD60R280CFD7
	Driver	2ED2109S06F

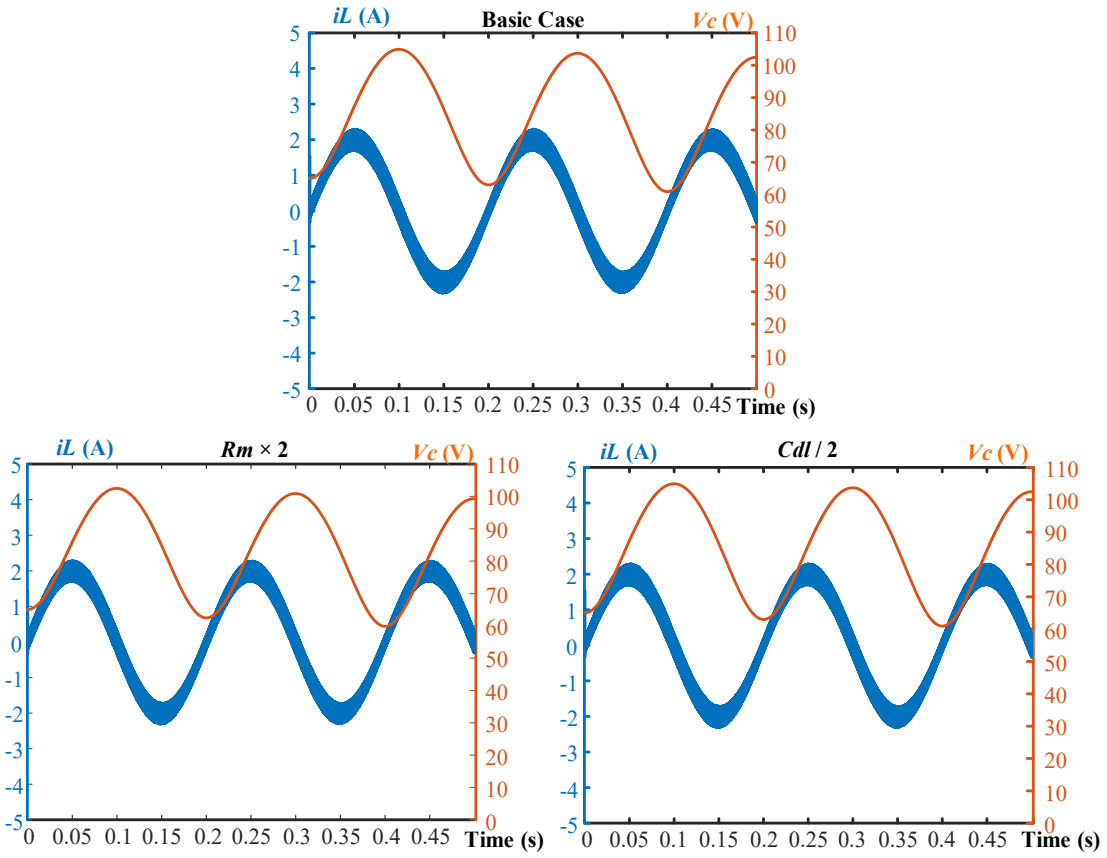

Fig. 5.10. Simulation results of the auxiliary converter of base case from Table 5.1 and changed R_m and C_{dl}.

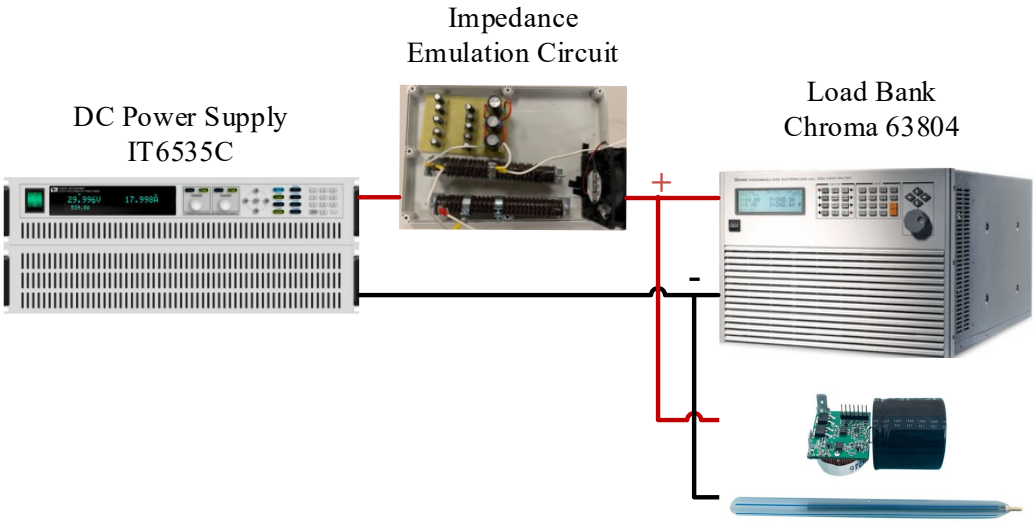

Fig. 5.11. Experimental setup: the size of IT6535C is 483mm×194mm×640.8mm and the designed auxiliary converter is comparable with a regular pen.

5.2.2 Experimental Results

To verify the proposed auxiliary converter solution, a laboratory prototype and experimental setup are built as shown in Fig. 5.11 with the same parameters given in Table 5.1. The size of this auxiliary converter is quite small, evident in the figure when compared with a pen, facilitating its flexible placement. Given the analyses in the former sections, the auxiliary converter can also be designed to a higher operating point and lower EIS frequencies.

The experimental setup is made up of a dc power supply (ITECH IT6535C) set to 45 V and an impedance circuit to emulate the internal impedance of the Nexa fuel cell module from Ballard Power Systems [76]. The experiments are carried out on an emulated FCS. The load bank (Chroma 63804) is set to constant current mode. The output power from the emulated FCS increases by drawing more current. The auxiliary converter is controlled by a TI TMS320F28335 platform, implemented with control algorithms and software protections. The starting of this converter is to charge the capacitor with a small constant current to the desired V_{c0} and then, modulating the ac perturbation by controlling i_L. The testing equipment used are Tektronix DPO2014 digital oscilloscope, Tektronix TCP0030 current probe and P5205A-NEW high-voltage differential probe.

The experimental results are given in Figs. 5.12-5.18. The ac current waveform and the resulting load side capacitor voltage are given in each figure. The load bank pulls 10 A and 20 A from the emulated fuel cell, inducing a fuel cell voltage of 43 V and 40.7 V, respectively. As shown in the

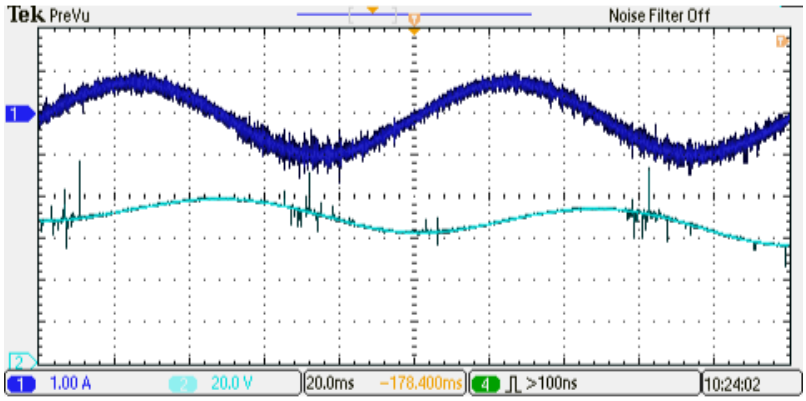

Fig. 5.12. Experimental results of auxiliary converter when emulated fuel cell operating at 10 A, EIS frequency at 10 Hz and initial capacitor voltage is 65 V. Channel 1 is i_L (1 A/Div) and Channel 2 is V_c (20 V/Div). Time: 20 ms/Div.

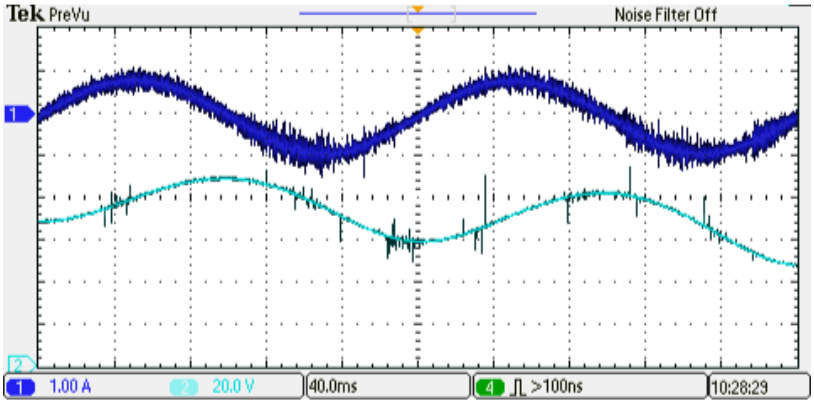

Fig. 5.13. Experimental results of auxiliary converter when emulated fuel cell operating at 10 A, EIS frequency at 5 Hz and initial capacitor voltage is 65 V. Channel 1 is i_L (1 A/Div) and Channel 2 is V_c (20 V/Div). Time: 40 ms/Div.

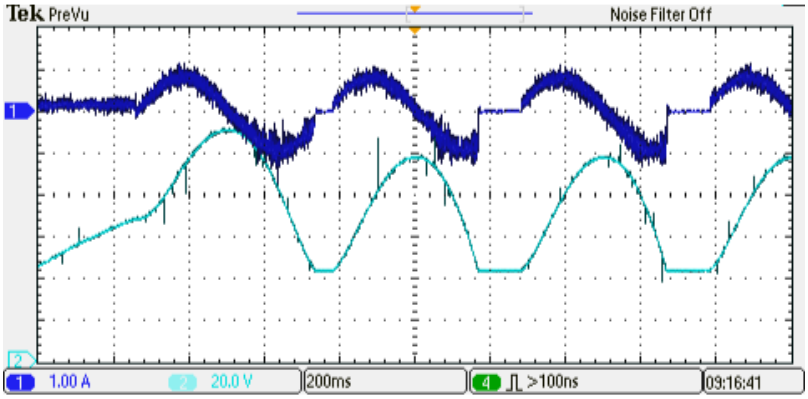

Fig. 5.14. Experimental results of auxiliary converter when emulated fuel cell operating at 10 A, EIS frequency at 2 Hz and initial capacitor voltage is 65 V. Channel 1 is i_L (1 A/Div) and Channel 2 is V_c (20 V/Div). Time: 200 ms/Div.

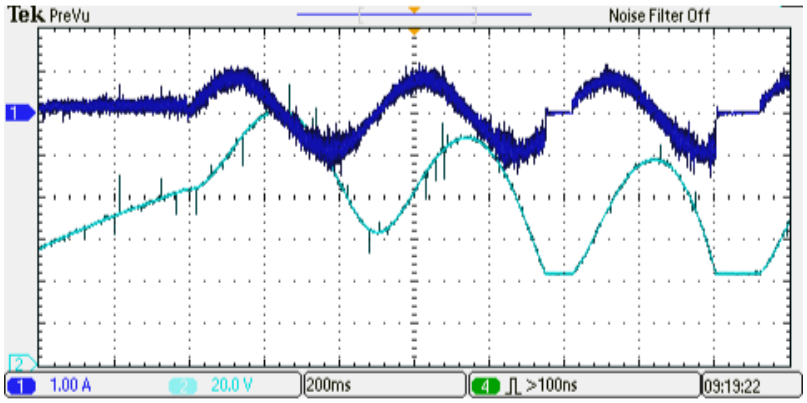

Fig. 5.15. Experimental results of auxiliary converter when emulated fuel cell operating at 10 A, EIS frequency at 2 Hz and initial capacitor voltage is 80 V. Channel 1 is i_L (1 A/Div) and Channel 2 is V_c (20 V/Div). Time: 200 ms/Div.

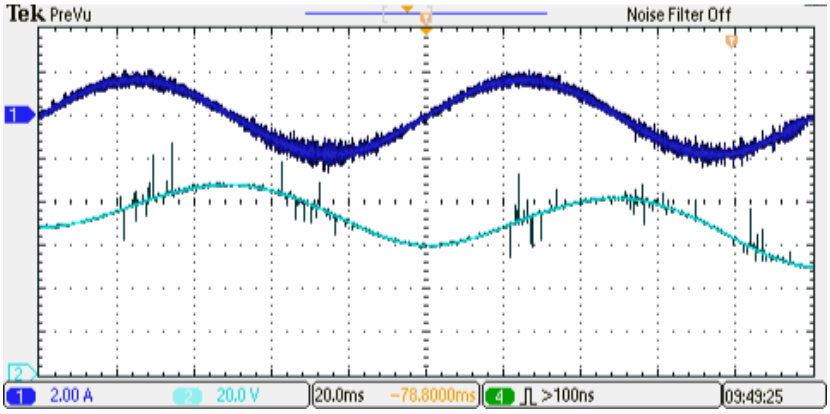

Fig. 5.16. Experimental results of auxiliary converter when emulated fuel cell operating at 20 A, EIS frequency at 10 Hz and initial capacitor voltage is 65 V. Channel 1 is i_L (2 A/Div) and Channel 2 is V_c (20 V/Div). Time: 20 ms/Div.

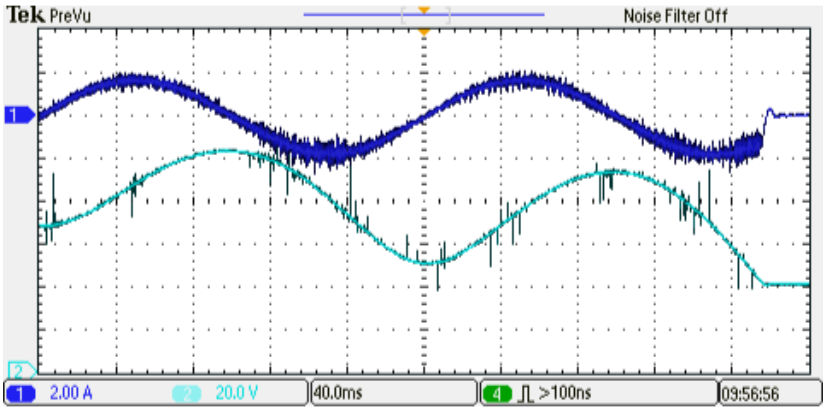

Fig. 5.17. Experimental results of auxiliary converter when emulated fuel cell operating at 20 A, EIS frequency at 5 Hz and initial capacitor voltage is 65 V. Channel 1 is i_L (2 A/Div) and Channel 2 is V_c (20 V/Div). Time: 40 ms/Div.

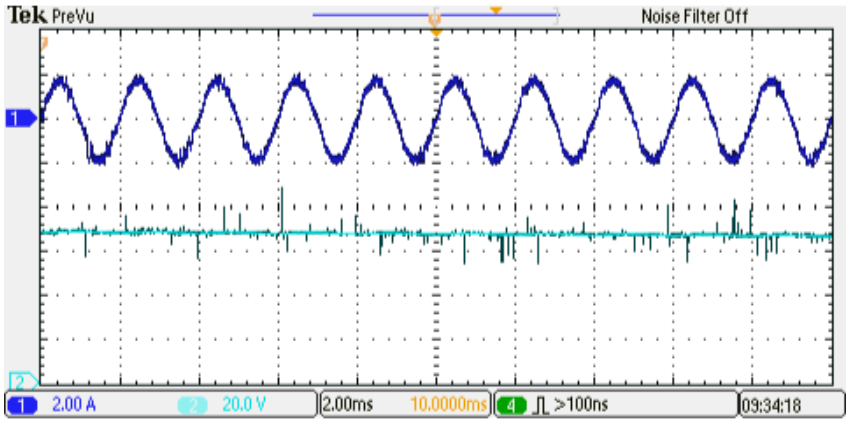

Fig. 5.18. Experimental results of auxiliary converter when emulated fuel cell operating at 20 A, EIS frequency at 500 Hz and initial capacitor voltage is 65 V. Channel 1 is i_L (2 A/Div) and Channel 2 is V_c (20 V/Div). Time: 2 ms/Div.

figures, the required sinusoidal current perturbations are generated at different frequencies and they are pure ac current in the auxiliary converter.

Low-frequency perturbations at 10 Hz, 5 Hz, and 2 Hz with 10 A fuel cell dc output current are given in Figs. 5.12-5.14. The capacitor voltages experience a noticeable swing that is inversely proportional to the EIS frequency. For Figs. 5.12 and 5.13, the expected maximal voltages from (5.9) are 77.7816 V and 88.7409 V, respectively, matching well with the experimental results. In Fig. 5.14, the capacitor voltage swings to a level lower than the fuel cell voltage, leading to a distorted i_L due to the high-magnitude oscillation and dc decaying on v_c. To cope with this, the initial voltage of the capacitor is pre-charged to 80 V and the triggered EIS result is shown in Fig. 5.15. The continuous operation of the setup will unavoidably have a v_c that is lower than the fuel cell voltage. However, in practice, one cycle is enough for low-frequency perturbations as it contains a high number of switching and sampling.

The results with the load bank drawing 20 A current are shown in Figs. 5.16-5.18 with perturbation magnitudes increased to 2 A. Compared with the results in Figs. 5.12 and 5.13, higher magnitudes of the capacitor voltage are observed, while the expected maximal voltages from (5.9) are 87.6340 V and 105.5199 V, respectively. It proves that oscillations on the capacitor are increased by a higher fuel cell operating point. The power from an FCS is affected by the application scenarios, such as in a lab, more power can be drawn from the FCS with large load banks, and power rating is limited when EIS is applied in the field for servicing. On the other hand, limited power can be pulled from an FCS during the motor is idling in a vehicle, depending on the

capacity of the on-board energy storage if it were used for setting the operating point of the FCS and the FCS can be operated at rated power when the motor is running.

The generated high-frequency perturbation of 500 Hz is given in Fig. 5.18 with the converter switching at 100 kHz. The capacitor voltage is relatively stable in this case.

5.3 Summary and Conclusions

In this chapter, an auxiliary converter solution is proposed to generate the needed ac perturbations for carrying out *in situ* EIS for FCS. Its topology and control design, operating principles, components sizing, and simulation and experimental results are presented. With the presented analysis and results, the auxiliary converter can be re-sized to an FCS at any rating. As compared with existing solutions in practice and literature, the plug-and-play feature of the proposed auxiliary converter makes it a very attractive solution for both fuel cell manufacturers and system integrators in bringing advanced diagnostic functions to FCS.

Chapter 6 Conclusions and Future Works

6.1 Summary and Conclusions

This thesis addresses issues related to enabling *in situ* EIS for high-power FCS with ac perturbations generated from switching power converters. Limitations and challenges are identified, and novel solutions are presented and verified with simulations and laboratory experimental setups. The key contributions of this work are summarized as follows:

1. Facing the challenge of enabling ac perturbations using existing high-power fuel cell PPCs with low switching frequencies, a control method is proposed to extend its EIS frequency range. Given the extra information from the proposed solution, a low-cost impedance processing method is also proposed to be included in the converter controller, completing a total software method for embedding the advanced diagnostic function into the PPC of an FCS. Therefore, the presented solution brings advanced diagnostic functions to the fuel cell PPCs with only the updating of firmware codes as retrofitting. Experimental results are presented to validate the proposed approaches.

2. Oscillations introduced by generating EIS ac perturbations from the fuel cell PPC and its influences on the interconnecting system were neglected in previous literature. A solid analyzing approach, small signal technique, is adopted, which takes the advantage of the relatively low magnitude of ac perturbation in EIS operations. The results indicate that system parameters and operating conditions are both playing a role in the magnitude of oscillations on the common dc link. With a hybrid system, the oscillations reach their peak at the resonant frequency of the energy storage converter. Moreover, along with the usage of an FCS or occurring of a faulty condition, the increased internal resistance tends to reduce the dc link oscillations.

3. Facing the disturbances on the common dc link induced by the converter based EIS, a type of CF isolated converter is proposed to remove the oscillations from dc link to PSES, where the PSES in the proposed converter topology is multiplexed to clamping the primary side voltage and absorb oscillations. Therefore, the dc link only needs to consider switching ripples by adopting this converter and capacitance can be sized smaller since no load is connected when the PSES is a

capacitor. Moreover, a designing method of this converter is proposed considering the characteristics of the FCS to operate at the desired mode and achieve soft switching. In the end, a fuel cell oriented designed method is presented, and the embedded EIS function of this converter reaches both high and low ends of the EIS frequencies. Experimental results are presented to verify the proposed converter.

4. An auxiliary converter concept is proposed to decouple the main power transferring path and EIS generations, where the oscillations induced by EIS are fully preserved in the auxiliary converter. Moreover, the proposed auxiliary converter only processes ac perturbations needed for EIS operation and cycling through instantaneous energy storage. Therefore, it features a compact plug-and-play module with great flexibilities, facilitating its placement and integration. Detailed designs are given and verifications with experimental results are presented as well.

6.2 Future Works

6.2.1 Implementing the Proposed Methods on a Practical Fuel Cell Stack

In chapter 2 of this thesis, the experiments were carried out in a laboratory setup with a dc power source and an impedance circuit emulating a fuel cell. This arrangement is more practical as the focus of this thesis is on the external electrical systems and facilitates the process of verifying the accuracy of impedance calculations. Moving the proposed approaches to an industry-adopted FCS is of great interest in the future research to bring the proposed approach closer to practical implementations. Moreover, various faults can be tested and used to set the alarm threshold of the proposed impedance processing method with a real FCS.

6.2.2 Topology Modifications and Controls of the Isolated Converter

Chapter 4 adopts only one possibility of realizing the proposed type of isolated converter. Other topologies as well as using a battery or a supercapacitor as the PSES can be further explored. In this way, a three-port converter is formed, where the future research focus would be the proper sizing and energy management of the energy storage to hold the operating point of the FCS and absorb oscillations simultaneously.

On the other hand, the resonant controller proposed in Chapter 2 for high-frequency perturbations can be applied to the current control loop of isolated converters as well to achieve high quality ac sinusoidal waveforms.

6.2.3 Buck Type Auxiliary Converter and Utilizing Battery/Supercapacitor for Energy Buffer

In Chapter 5, the realized auxiliary converter is formed by a boost type converter with a capacitor as the energy buffer. The auxiliary converter can also be designed as a buck type for the switching network, while an extra carefully designed input filter is necessary in this case to remove the switching noise to the fuel cell. If an LC or other high order filter were used as the input filter, the introduced resonance should be appropriately damped.

On the other hand, a small size battery or a supercapacitor can be used as the energy buffer in the proposed auxiliary converter. However, a battery or a supercapacitor bank is formed by serially connected cells and has a relatively low voltage on small scale, while using a full energy storage bank deteriorates the merits of low-cost and compactness of this auxiliary converter. Therefore, a high boost conversion stage is necessary to utilize the high energy of the small-scale battery/supercapacitor. A switched-capacitor converter can be a good candidate to boost up the voltage of the battery/supercapacitor to connect to the load side of the auxiliary converter, where the switched capacitor converter provides a fixed conversion ratio without complex closed loop control design. By this arrangement, it takes advantage of the high-energy-density of a battery/supercapacitor to reduce the volume of the proposed auxiliary converter potentially further.

Moreover, future works can be done to explore the derivations of the auxiliary converter to improve its power- and energy-density.

6.2.4 Different Forms of Perturbations

The ac perturbations adopted in this thesis is in sinusoidal forms, giving a higher frequency concentration. However, other forms of perturbations can also be applied with the proposed converter solutions, such as pseudo-random binary sequences or multi-sine signals. With the works done in this thesis, any form of perturbation can be generated by the proposed converter solutions as long as it is designed appropriately.

References

[1] J. Lai and M. W. Ellis, "Fuel Cell Power Systems and Applications," *Proceedings of the IEEE*, vol. 105, no. 11, pp. 2166-2190, Nov. 2017.

[2] W. Schmittinger and A. Vahidi, "A review of the main parameters influencing long-term performance and durability of PEM fuel cells", *J. Power Sources*, vol. 180, no. 1, pp. 1-14, 2008.

[3] T. Sutharssan, D. Montalvao, Y. K. Chen, W. Wang, C. Pisac and H. Elemara, "A review on prognostics and health monitoring of proton exchange membrane fuel cell", *Renew. Sust. Energ. Rev.*, vol. 75, pp. 440-450, 2017.

[4] X. Li, J. Li, L. Xu, F. Yang, J. Hua and M. Ouyang, "Performance analysis of proton-exchange membrane fuel cell stacks used in Beijing urban-route buses trial project", *Int. J. Hydrogen Energy*, vol. 35, no. 8, pp. 3841-3847, 2010.

[5] L. Eudy and M. Post, " BC Transit Fuel Cell Bus Project Evaluation Results: Second Report", *National Renewable Energy Laboratory Technical Report*, NREL/TP-5400-62317, 2014.

[6] R. Onanena, L. Oukhellou, D. Candusso, F. Harel, D. Hissel and P. Aknin, "Fuel cells static and dynamic characterizations as tools for the estimation of their ageing time," *Int. J. Hydrogen Energy*, vol. 36, no. 2, pp. 1730-1739, 2011.

[7] A. Debenjak, J. Petrovčič, P. Boškoski, B. Musizza and Đ. Juričić, "Fuel Cell Condition Monitoring System Based on Interconnected DC–DC Converter and Voltage Monitor," *IEEE Trans. Ind. Electron.*, vol. 62, no. 8, pp. 5293-5305, Aug. 2015.

[8] S. Thomas, S. Lee, A. Sahu and S. Park, " Online health monitoring of a fuel cell using total harmonic distortion analysis," *Int. J. Hydrogen Energy*, vol. 39, no. 9, pp. 4558-4565, 2014.

[9] N. Fouquet, C. Doulet, C. Nouillant, G. Dauphin-Tanguy and B. Ould-Bouamama, "Model based PEM fuel cell state-of-health monitoring via ac impedance measurements", *J. Power Sources*, vol. 159, no. 2, pp. 905-913, 2006.

[10] A. Gebregergis, P. Pillay and R. Rengaswamy, "PEMFC Fault Diagnosis, Modeling, and Mitigation," *IEEE Trans. Ind. Appl.*, vol. 46, no. 1, pp. 295-303, Jan.-feb. 2010.

[11] Z. Zheng, M. Péra, D. Hissel, M. Becherif, K. Agbli and Y. Li, "A double-fuzzy diagnostic methodology dedicated to online fault diagnosis of proton exchange membrane fuel cell stacks," *J. Power Sources*, vol. 271, pp. 570-581, Dec. 2014.

[12] D. Hissel, D. Candusso and F. Harel, "Fuzzy-Clustering Durability Diagnosis of Polymer Electrolyte Fuel Cells Dedicated to Transportation Applications", *IEEE Trans. Veh. Technol.*, vol. 56, no. 5, pp. 2414-2420, 2007.

[13] J. Kim, J. Lee and B. H. Cho, "Equivalent Circuit Modeling of PEM Fuel Cell Degradation Combined With a LFRC," *IEEE Trans. Ind. Electron.*, vol. 60, no. 11, pp. 5086-5094, Nov. 2013.

[14] C. de Beer, P. S. Barendse, P. Pillay, B. Bullecks and R. Rengaswamy, "Classification of High-Temperature PEM Fuel Cell Degradation Mechanisms Using Equivalent Circuits," *IEEE Trans. Ind. Electron.*, vol. 62, no. 8, pp. 5265-5274, Aug. 2015.

[15] C. Yan, J. Chen, H. Liu, L. Kumar and H. Lu, "Health Management for PEM Fuel Cells Based on an Active Fault Tolerant Control Strategy," *IEEE Trans. Sustain. Energy*, 08 Dec. 2020.

[16] X. Yuan, H. Wang, J. C. Sun, and J. Zhang, "AC impedance technique in PEM fuel cell diagnosis—A review," *Int. J. Hydrogen Energy*, vol.32, No.17, pp.4365- 4380, 2007.

[17] H. Homayouni, J. DeVaal, F. Golnaraghi and J. Wang, "Voltage Reduction Technique for Use with Electrochemical Impedance Spectroscopy in High-Voltage Fuel Cell and Battery Systems," *IEEE Trans. Transport. Electrific.*, vol. 4, no. 2, pp. 418-431, June 2018.

[18] S. M. R. Islam and S. Park, "Precise Online Electrochemical Impedance Spectroscopy Strategies for Li-Ion Batteries," *IEEE Trans. Ind. Appl.*, vol. 56, no. 2, pp. 1661-1669, March-April 2020.

[19] H. Lu, J. Chen, C. Yan, and H. Liu, “On-line fault diagnosis for proton exchange membrane fuel cells based on a fast electrochemical impedance spectroscopy measurement,” Journal of Power Sources, vol. 430, pp. 233–243, Aug. 2019.

[20] M. Ordonez, M. O. Sonnaillon, J. E. Quaicoe and M. T. Iqbal, "An Embedded Frequency Response Analyzer for Fuel Cell Monitoring and Characterization," *IEEE Trans. Ind. Electron.*, vol. 57, no. 6, pp. 1925-1934, June 2010.

[21] T. Nguyen, V. Doan and W. Choi, "Design of a Fuel Cell Power Conditioning System for Online Diagnosis and Load Leveling," *Journal of Power Electronics*, vol. 16, no. 2, pp. 695-703, 2016.

[22] X. Yan, M. Hou, L. Sun, D. Liang, Q. Shen, H. Xu, P. Ming and B. Yi, "AC impedance characteristics of a 2kW PEM fuel cell stack under different operating conditions and load changes," *Int. J. Hydrogen Energy*, vol. 32, no. 17, pp. 4358-4364, 2007.

[23] A. Dhirde, N. Dale, H. Salehfar, M. Mann and T. Han, "Equivalent Electric Circuit Modeling and Performance Analysis of a PEM Fuel Cell Stack Using Impedance Spectroscopy," *IEEE Trans. Energy Convers.*, vol. 25, no. 3, pp. 778-786, 2010.

[24] G. Mousa, "Fuel Cell Diagnostics using Electrochemical Impedance Spectroscopy", Ph.D, Simon Fraser University, 2014.

[25] N. Wagner and E. Gülzow, "Change of electrochemical impedance spectra (EIS) with time during CO-poisoning of the Pt-anode in a membrane fuel cell," *J. Power Sources*, vol. 127, no. 1-2, pp. 341-347, 2004.

[26] J. Wu, X. Yuan, J. Martin, H. Wang, J. Zhang, J. Shen, S. Wu and W. Merida, "A review of PEM fuel cell durability: Degradation mechanisms and mitigation strategies", *J. Power Sources*, vol. 184, no. 1, pp. 104-119, 2008.

[27] P. Pei and H. Chen, "Main factors affecting the lifetime of Proton Exchange Membrane fuel cells in vehicle applications: A review", *Applied Energy*, vol. 125, pp. 60-75, 2014.

[28] 2014 IEEE PHM Data Challenge, FCLAB Research Federation, France, 2014, [Online]. Available: http://eng.fclab.fr/ieee-phm-2014-data- challenge/

[29] D. Zhou, F. Gao, E. Breaz, A. Ravey and A. Miraoui, "Degradation prediction of PEM fuel cell using a moving window based hybrid prognostic approach", *Energy*, vol. 138, pp. 1175-1186, 2017.

[30] J. K. Kimotho, T. Meyer and W. Sextro, "PEM fuel cell prognostics using particle filter with model parameter adaptation," *2014 International Conference on Prognostics and Health Management*, Cheney, WA, 2014, pp. 1-6.

[31] L. Zhu and J. Chen, "Prognostics of PEM fuel cells based on Gaussian process state space models," *Energy*, vol. 149, pp. 63-73, 2018.

[32] H. Liu, J. Chen, M. Hou, Z. Shao and H. Su, "Data-based short-term prognostics for proton exchange membrane fuel cells," *Int. J. Hydrogen Energy*, vol. 42, no. 32, pp. 20791-20808, 2017.

[33] Z. Hu, L. Xu, J. Li, M. Ouyang, Z. Song and H. Huang, "A reconstructed fuel cell life-prediction model for a fuel cell hybrid city bus," *Energy Conversion and Management*, vol. 156, pp. 723-732, 2018.

[34] M. Bressel, M. Hilairet, D. Hissel and B. Ould Bouamama, "Remaining Useful Life Prediction and Uncertainty Quantification of Proton Exchange Membrane Fuel Cell Under Variable Load," *IEEE Trans. Ind. Electron.*, vol. 63, no. 4, pp. 2569-2577, 2016.

[35] T. Kim, H. Oh, H. Kim and B. D. Youn, "An Online-Applicable Model for Predicting Health Degradation of PEM Fuel Cells with Root Cause Analysis," *IEEE Trans. on Ind. Electron.*, vol. 63, no. 11, pp. 7094-7103, Nov. 2016.

[36] G. Mousa, F. Golnaraghi, J. DeVaal and A. Young, "Detecting proton exchange membrane fuel cell hydrogen leak using electrochemical impedance spectroscopy method", *J. Power Sources*, vol. 246, pp. 110-116, 2014.

[37] G. Mousa, J. DeVaal and F. Golnaraghi, "Diagnosis of hydrogen crossover and emission in proton exchange membrane fuel cells", *Int. J. Hydrogen Energy*, vol. 39, Is. 35, pp. 20116-20126, 2014.

[38] J. Sihvo, T. Roinila, T. Messo, and D.-i. Stroe, "Novel online fitting algorithm for impedance-based state estimation of Li-ion batteries," *IECON 19 Proceedings (Industrial Electronics Conference)*. IEEE, 2019.

[39] J. Shen, H. Homayouni and J. Wang, "An Online Impedance Processing Method for Fuel Cell EIS Measurements Enabling Degradation Information Extraction", *2019 IEEE 28th International Symposium on Industrial Electronics (ISIE)*, Vancouver, Canada, 12-14 June 2019.

[40] C. Jeppesena, S. S. Arayaa, S. L. Sahlina, S. Thomasa, S. J. Andreasen and S. K. Kæra, "Fault detection and isolation of high temperature proton exchange membrane fuel cell stack under the influence of degradation." *J. Power Sources*, vo. 359, pp. 37-47, 2017.

[41] C. de Beer, P. S. Barendse and P. Pillay, "Fuel Cell Condition Monitoring Using Optimized Broadband Impedance Spectroscopy," *IEEE Trans. Ind. Electron.*, vol. 62, no. 8, pp. 5306-5316, Aug. 2015.

[42] M. Hinaje, I. Sadli, J.-P. Martin, P. Thounthong, S. Raël and B. Davat, "Online humidification diagnosis of a PEMFC using a static DC–DC converter," *Int. J. Hydrogen Energy*, vol. 34, no. 6, pp. 2718-2723, 2009.

[43] G. Dotelli, R. Ferrero, P. G. Stampino, S. Latorrata and S. Toscani, "Diagnosis of PEM Fuel Cell Drying and Flooding Based on Power Converter Ripple," *IEEE Trans. Instrum. Meas.*, vol. 63, no. 10, pp. 2341- 2348, Oct. 2014.

[44] G. Dotelli, R. Ferrero, P. G. Stampino, S. Latorrata and S. Toscani, "PEM Fuel Cell Drying and Flooding Diagnosis with Signals Injected by a Power Converter," *IEEE Trans. Instrum. Meas.*, vol. 64, no. 8, pp. 2064-2071, Aug. 2015.

[45] N. Katayama and S. Kogoshi, "Real-Time Electrochemical Impedance Diagnosis for Fuel Cells Using a DC–DC Converter," *IEEE Trans. Energy Convers.,* vol. 30, no. 2, pp. 707-713, June 2015.

[46] D. Depernet, A. Narjiss, F. Gustin, D. Hissel and M. Péra, "Integration of electrochemical impedance spectroscopy functionality in proton exchange membrane fuel cell power converter," *Int. J. Hydrogen Energy*, vol. 41, no. 11, pp. 5378-5388, 2016.

[47] L. Zhang, Z. Zhou, Q. Chen, R. Long and S. Quan, "Model Predictive Control for Electrochemical Impedance Spectroscopy Measurement of Fuel Cells Based on Neural Network Optimization," *IEEE Trans. Transp. Electrific.*, vol. 5, no. 2, pp. 524-534, June 2019.

[48] P. Hong, J. Li, L. Xu, M. Ouyang and C. Fang, "Modeling and simulation of parallel DC/DC converters for online AC impedance estimation of PEM fuel cell stack," *Int. J. Hydrogen Energy*, vol. 41, no. 4, pp. 3004-3014, 2016.

[49] P. Hong, J. Li, L. Xu, M. Ouyang and C. Fang, "A new approach to online AC impedance measurement at high frequency of PEM fuel cell stack," *Int. J. Hydrogen Energy*, vol. 42, no. 30, pp. 19156-19169, 2017.

[50] D. A. Howey, P. D. Mitcheson, V. Yufit, G. J. Offer and N. P. Brandon, "Online Measurement of Battery Impedance Using Motor Controller Excitation*," IEEE Trans. Veh. Technol.*, vol. 63, no. 6, pp. 2557-2566, July 2014.

[51] W. Huang and J. A. Abu Qahouq, "An Online Battery Impedance Measurement Method Using DC–DC Power Converter Control," *IEEE Trans. Ind. Electron.*, vol. 61, no. 11, pp. 5987-5995, Nov. 2014.

[52] Y. Lee, S. Park and S. Han, "Online Embedded Impedance Measurement Using High-Power Battery Charger," *IEEE Trans. Ind. Appl.*, vol. 51, no. 1, pp. 498-508, Jan.-Feb. 2015.

[53] E. Din, C. Schaef, K. Moffat, and J. T. Stauth, “A scalable active battery management system with embedded real-time electrochemical impedance spectroscopy,” *IEEE Trans. Power Electron.*, vol. 32, no. 7, pp. 5688–5698, Jul. 2017.

[54] J. A. A. Qahouq and Z. Xia, "Single-Perturbation-Cycle Online Battery Impedance Spectrum Measurement Method With Closed-Loop Control of Power Converter," *IEEE Trans. Ind. Electron.*, vol. 64, no. 9, pp. 7019-7029, Sept. 2017.

[55] H. Wang, A. Gaillard and D. Hissel, "A review of DC/DC converter-based electrochemical impedance spectroscopy for fuel cell electric vehicles," *Int. J. Hydrogen Energy*, vol. 141, pp. 124-138, 2019.

[56] M. Karimi-Ghartemani, S. A. Khajehoddin, P. K. Jain, and A. Bakhshai, "A systematic approach to DC-bus control design in single-phase grid- connected renewable converters," *IEEE Trans. Power Electron.*, vol. 28, no. 7, pp. 3158–3166, Jul. 2013.

[57] J. Klima, M. Chomat and L. Schreier, "Analytical closed-form investigation of pwm inverter induction motor drive performance under dc bus voltage pulsation," *IET Electric Power Applications*, vol. 2, no. 6, pp. 341-352, November 2008.

[58] R. W. Erickson and D. Maksimovic, Fundamentals of Power Electronics. New York, NY, USA: Springer-Verlag, 2001.

[59] R. Teodorescu, F. Blaabjerg, M. Liserre and P. C. Loh, "Proportional-resonant controllers and filters for grid-connected voltage-source converters," *IEE Proceedings - Electric Power Applications*, vol. 153, no. 5, pp. 750-762, September 2006.

[60] A. G. Yepes, F. D. Freijedo, Ó. Lopez and J. Doval-Gandoy, "Analysis and Design of Resonant Current Controllers for Voltage-Source Converters by Means of Nyquist Diagrams and Sensitivity Function," *IEEE Trans. Ind. Electron.*, vol. 58, no. 11, pp. 5231-5250, Nov. 2011.

[61] C. Xie, X. Zhao, K. Li, J. Zou and J. M. Guerrero, "A New Tuning Method of Multiresonant Current Controllers for Grid-Connected Voltage Source Converters," *IEEE Trans. Emerg. Sel. Topics Power Electron.*, vol. 7, no. 1, pp. 458-466, March 2019.

[62] Yuan XZ, Song C, Wang H, Zhang J. Electrochemical impedance spectroscopy in PEM fuel cells: fundamentals and applications. Springer Science & Business Media, 2009 Nov 25.

[63] H. Wang, A. Gaillard and D. Hissel, " Online electrochemical impedance spectroscopy detection integrated with step-up converter for fuel cell electric vehicle," *Int. J. Hydrogen Energy*, vol. 44, no. 2, pp. 1110-1121, 2019.

[64] A. Emadi, A. Khaligh, C. H. Rivetta, and G. A. Williamson, "Constant power loads and negative impedance instability in automotive systems: Definition, modeling, stability, and control

of power electronic converters and motor drives," *IEEE Trans. Veh. Technol.*, vol. 55, no. 4, pp. 1112– 1125, Jul. 2006.

[65] A. M. Rahimi and A. Emadi, "An analytical investigation of DC/DC power electronic converters with constant power loads in vehicular power systems," *IEEE Trans. Veh. Technol*., vol. 58, no. 6, pp. 2689–2702, Jul. 2009.

[66] A. M. Rahimi and A. Emadi, "Active damping in DC/DC power electronic converters: A novel method to overcome the problems of constant power loads," *IEEE Trans. Ind. Electron.*, vol. 56, no. 5, pp. 1428–1439, May 2009.

[67] M. Anun, M. Ordonez, I. G. Zurbriggen and G. G. Oggier, "Circular Switching Surface Technique: High-Performance Constant Power Load Stabilization for Electric Vehicle Systems," *IEEE Trans. on Power Electron.*, vol. 30, no. 8, pp. 4560-4572, Aug. 2015.

[68] W. Li, J. Xiao, Y. Zhao and X. He, "PWM Plus Phase Angle Shift (PPAS) Control Scheme for Combined Multiport DC/DC Converters," *IEEE Trans. Power Electron.*, vol. 27, no. 3, pp. 1479-1489, March 2012.

[69] J. Zhang, H. Wu, X. Qin and Y. Xing, "PWM Plus Secondary-Side Phase-Shift Controlled Soft-Switching Full-Bridge Three-Port Converter for Renewable Power Systems," *IEEE Trans. on Ind. Electron.*, vol. 62, no. 11, pp. 7061-7072, Nov. 2015.

[70] D. Sha, X. Wang and D. Chen, "High-Efficiency Current-Fed Dual Active Bridge DC–DC Converter With ZVS Achievement Throughout Full Range of Load Using Optimized Switching Patterns," *IEEE Trans. on Power Electron.*, vol. 33, no. 2, pp. 1347-1357, Feb. 2018.

[71] X. Sun, Y. Shen, Y. Zhu and X. Guo, "Interleaved Boost-Integrated LLC Resonant Converter with Fixed-Frequency PWM Control for Renewable Energy Generation Applications," *IEEE Trans. on Power Electron.*, vol. 30, no. 8, pp. 4312-4326, Aug. 2015.

[72] Z. Wang and H. Li, "A Soft Switching Three-phase Current-fed Bidirectional DC-DC Converter with High Efficiency Over a Wide Input Voltage Range," *IEEE Trans. on Power Electron.*, vol. 27, no. 2, pp. 669-684, Feb. 2012.

[73] D. Sha, Q. Lin, F. You, X. Wang and G. Xu, "A ZVS Bidirectional Three-Level DC–DC Converter with Direct Current Slew Rate Control of Leakage Inductance Current," *IEEE Trans. Ind Appl.*, vol. 52, no. 3, pp. 2368-2377, May-June 2016.

[74] M. C. Mira, Z. Zhang, A. Knott and M. A. E. Andersen, "Analysis, Design, Modeling, and Control of an Interleaved-Boost Full-Bridge Three-Port Converter for Hybrid Renewable Energy Systems," *IEEE Trans. Power Electron.*, vol. 32, no. 2, pp. 1138-1155, Feb. 2017.
[75] Ogawa, T., Umayahara, K., and Ikogi, Y., "Development of Fuel Cell (FC) System for New Generation FC Bus," *SAE Int. J. Adv. & Curr. Prac. in Mobility*, pp. 782-786, 2019.
[76] Nexa Power Module User's Manual, Ballard Power Systems, Burnaby, BC, Canada, 2003.